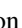




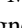



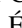




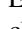
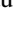
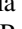
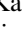

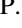

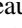

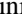

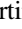
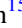






Spitzer Follow-up of Extremely Cold Brown Dwarfs Discovered by the Backyard Worlds: Planet 9 Citizen Science Project

Aaron M. Meisner¹ , Jacqueline K. Faherty² , J. Davy Kirkpatrick³ , Adam C. Schneider⁴ , Dan Caselden⁵ , Jonathan Gagné^{6,7} , Marc J. Kuchner⁸ , Adam J. Burgasser⁹ , Sarah L. Casewell¹⁰ , John H. Debes¹¹ , Étienne Artigau⁶ , Daniella C. Bardalez Gagliuffi² , Sarah E. Logsdon¹ , Rocío Kiman^{2,12} , Katelyn Allers¹³ , Chih-chun Hsu⁹ , John P. Wisniewski¹⁴ , Michaela B. Allen⁸, Paul Beaulieu¹⁵, Guillaume Colin¹⁵ , Hugo A. Durantini Luca¹⁶ , Sam Goodman¹⁵ , Léopold Gramaize¹⁵ , Leslie K. Hamlet¹⁵ , Ken Hinckley¹⁵ , Frank Kiwy¹⁵ , David W. Martin¹⁵, William Pendrill¹⁵, Austin Rothermich¹⁷ , Arttu Sainio¹⁵ , Jörg Schümann¹⁵ , Nikolaj Stevnbak Andersen¹⁵, Christopher Tanner¹⁵ , Vinod Thakur¹⁵, Melina Thévenot¹⁵ , Jim Walla¹⁵, Zbigniew Wędracki¹⁵, Christian Aganze⁹, Roman Gerasimov⁹, and Christopher Theissen^{9,18}

The Backyard Worlds: Planet 9 Collaboration

¹ NSF's National Optical-Infrared Astronomy Research Laboratory, 950 N. Cherry Ave., Tucson, AZ 85719, USA; ameisner@noao.edu

² Department of Astrophysics, American Museum of Natural History, Central Park West at 79th St., New York, NY 10024, USA

³ IPAC, Mail Code 100-22, California Institute of Technology, 1200 E. California Blvd., Pasadena, CA 91125, USA

⁴ School of Earth and Space Exploration, Arizona State University, Tempe, AZ 85282, USA

⁵ Gigamon Applied Threat Research, 619 Western Ave., Suite 200, Seattle, WA 98104, USA

⁶ Institute for Research on Exoplanets, Université de Montréal, 2900 Blvd. Édouard-Montpetit Montréal, QC H3T 1J4, Canada

⁷ Planétarium Rio Tinto Alcan, Espace pour la Vie, 4801 av. Pierre-de Coubertin, Montréal, QC, Canada

⁸ NASA Goddard Space Flight Center, Exoplanets and Stellar Astrophysics Laboratory, Code 667, Greenbelt, MD 20771, USA

⁹ Center for Astrophysics and Space Science, University of California San Diego, La Jolla, CA 92093, USA

¹⁰ Department of Physics and Astronomy, University of Leicester, University Road, Leicester LE1 7RH, UK

¹¹ ESA for AURA, Space Telescope Science Institute, 3700 San Martin Dr., Baltimore, MD 21218, USA

¹² Department of Physics, Graduate Center, City University of New York, 365 5th Ave., New York, NY 10016, USA

¹³ Physics and Astronomy Department, Bucknell University, 701 Moore Ave., Lewisburg, PA 17837, USA

¹⁴ Homer L. Dodge Department of Physics and Astronomy, University of Oklahoma, 440 W. Brooks St., Norman, OK 73019, USA

¹⁵ Backyard Worlds: Planet 9

¹⁶ IATE-OAC, Universidad Nacional de Córdoba-CONICET, Laprida 854, X5000 BGR, Córdoba, Argentina

¹⁷ Physics Department, University Of Central Florida, 4000 Central Florida Blvd., Orlando, FL 32816, USA

Received 2020 May 22; revised 2020 June 29; accepted 2020 June 30; published 2020 August 20

Abstract

We present Spitzer follow-up imaging of 95 candidate extremely cold brown dwarfs discovered by the Backyard Worlds: Planet 9 citizen science project, which uses visually perceived motion in multiepoch Wide-field Infrared Survey Explorer (WISE) images to identify previously unrecognized substellar neighbors to the Sun. We measure Spitzer [3.6]–[4.5] color to phototype our brown dwarf candidates, with an emphasis on pinpointing the coldest and closest Y dwarfs within our sample. The combination of WISE and Spitzer astrometry provides quantitative confirmation of the transverse motion of 75 of our discoveries. Nine of our motion-confirmed objects have best-fit linear motions larger than $1'' \text{ yr}^{-1}$; our fastest-moving discovery is WISEA J155349.96+693355.2 ($\mu \approx 2'' 15 \text{ yr}^{-1}$), a possible T-type subdwarf. We also report a newly discovered wide-separation (~ 400 au) T8 comoving companion to the white dwarf LSPM J0055+5948 (the fourth such system to be found), plus a candidate late T companion to the white dwarf LSR J0002+6357 at 5/5 projected separation (~ 8700 au if associated). Among our motion-confirmed targets, five have Spitzer colors most consistent with spectral type Y. Four of these five have exceptionally red Spitzer colors suggesting types of Y1 or later, adding considerably to the small sample of known objects in this especially valuable low-temperature regime. Our Y dwarf candidates begin bridging the gap between the bulk of the Y dwarf population and the coldest known brown dwarf.

Unified Astronomy Thesaurus concepts: Y dwarfs (1827); Brown dwarfs (185); T dwarfs (1679); Visual binary stars (1777); Proper motions (1295); Solar neighborhood (1509); Infrared astronomy (786)

Supporting material: machine-readable tables

1. Introduction

A complete census of the solar neighborhood provides the best way to identify and study the Galactic substellar population. The intrinsic faintness of the lowest-temperature brown dwarfs means that we can only hope to directly image those that are nearby to the Sun. For any given substellar type, the examples most amenable to detailed follow-up observations will be those that are

closest. In particular, as the James Webb Space Telescope (JWST; Gardner et al. 2006) nears launch, it is critical to identify the highest-priority brown dwarf targets for spectroscopic characterization, especially pushing into the low-mass/temperature regime of isolated exoplanet analogs.

By virtue of its unprecedented full-sky sensitivity at 3–5 μm , the Wide-field Infrared Survey Explorer (WISE; Wright et al. 2010) has dramatically enhanced our ability to pinpoint the coldest brown dwarfs and reshaped our view of the solar neighborhood (e.g.,

¹⁸ NASA Sagan Fellow.

Cushing et al. 2011; Kirkpatrick et al. 2011; Luhman 2013, 2014b). The WISE W1 ($3.4\ \mu\text{m}$) and W2 ($4.6\ \mu\text{m}$) bandpasses were specifically engineered to enable the selection of ultracold brown dwarfs via their red W1–W2 colors (Mainzer et al. 2011b). Including recent data from the NEOWISE mission (Mainzer et al. 2011a, 2014), WISE has now surveyed the entire sky 14 times spanning almost a decade, making identification of nearby brown dwarfs based on their large apparent motions an increasingly important tool for their discovery (e.g., Kirkpatrick et al. 2014, 2016; Luhman 2014a; Scholz 2014; Schneider et al. 2016; Kuchner et al. 2017; Marocco et al. 2019; Meisner et al. 2020).

However, the vast WISE/NEOWISE data set has yet to be exhaustively searched for cold and close brown dwarfs (e.g., Kirkpatrick et al. 2019). WISE has detected more than 2 billion unique astronomical sources (Schlafly et al. 2019), and its full imaging archive contains over 30 trillion pixels. Despite modern computing resources, human vetting still plays an integral role in the discovery of moving objects among a sea of interlopers and artifacts (e.g., Kirkpatrick et al. 2014, 2016; Schneider et al. 2016).

To overcome the bottleneck of visual inspection encountered by WISE-based moving object searches, we initiated the Backyard Worlds: Planet 9 citizen science project (<http://backyardworlds.org>; Kuchner et al. 2017, hereafter Backyard Worlds). Backyard Worlds crowdsources the visual vetting workload among thousands of volunteers who participate via the internet, viewing animated blinks of WISE images spanning the full WISE+NEOWISE time baseline. In this work we present a sample of 96 candidate extremely cold brown dwarfs discovered by Backyard Worlds volunteers. For this sample, which generally lacks high-significance detections at W1, we have obtained critical Spitzer/IRAC (Werner et al. 2004; Fazio et al. 2004) photometry at $3.6\ \mu\text{m}$ (ch1) and $4.5\ \mu\text{m}$ (ch2). Secure ch1 detections enable estimates of key parameters, including spectral type, effective temperature, and distance.

In Section 2 we briefly summarize the WISE and NEOWISE missions. In Section 3 we provide background information about the Backyard Worlds project. In Section 4 we explain our selection of the Spitzer follow-up targets that compose our sample (Section 5). In Section 6 we discuss our Spitzer observing strategy. In Section 7 we present our Spitzer photometry. In Section 8 we present follow-up spectroscopic confirmations. In Section 9 we perform WISE and Spitzer astrometry in order to assess significance of motion. In Section 10 we present follow-up and archival near-infrared (NIR) photometry for our sample. In Section 11 we synthesize our photometry, spectroscopy, and astrometry results, commenting on various individual objects of particular interest. We conclude in Section 12.

2. WISE/NEOWISE Overview

WISE is a 0.4 m aperture space telescope in low Earth orbit, launched in late 2009. WISE mapped the entire sky once in all four of its broad mid-infrared channels ($W1 = 3.4\ \mu\text{m}$, $W2 = 4.6\ \mu\text{m}$, $W3 = 12\ \mu\text{m}$, and $W4 = 22\ \mu\text{m}$) during the first half of 2010 (Cutri et al. 2012). In the latter part of 2010 the two longest wavelength bands became unusable owing to exhaustion of onboard cryogen. However, WISE continued to operate in W1 and W2 through early 2011 thanks to the NEOWISE mission extension (Mainzer et al. 2011a). WISE was put into hibernation from 2011 February until 2013 December, at which

point it recommenced surveying in W1 and W2 as part of the NEOWISE-Reactivation mission (NEOWISE-R; Mainzer et al. 2014; Cutri et al. 2015). NEOWISE-R has continued its W1/W2 observations ever since.

A typical sky location is observed for a ~ 1 -day time period once every 6 months. WISE has now completed a total of 14 such full-sky mappings in W1 and W2. By co-adding exposures within each 6-monthly visit to each sky location, it is possible to construct a time series of deep and clean WISE co-adds optimized for detecting faint moving objects (Meisner et al. 2018b, 2018c, 2019) while leveraging a time baseline $>10\times$ longer than that of AllWISE (Cutri et al. 2013). The joint analysis of WISE and NEOWISE data therefore opens up a huge discovery space for finding faint moving objects, such as cold brown dwarfs, in the mid-infrared.

3. Backyard Worlds Overview

In order to fully mine the combined WISE+NEOWISE data set for moving object discoveries, we launched the Backyard Worlds: Planet 9 citizen science project on 2017 February 15 (Kuchner et al. 2017). Backyard Worlds crowdsources the process of visually confirming motion in WISE images by distributing animated “flipbooks” via the Zooniverse web portal (Simpson et al. 2014). Each flipbook shows a time-series blink covering a random¹⁹ $\sim 10' \times 10'$ patch of sky. In detail, each frame of each blink is a color-composite difference image meant to null out static background sources. Each difference image is built by creating one co-added sky pass worth of WISE data (a “time-resolved unWISE co-add”; Meisner et al. 2018b) and then subtracting off a static sky template built by co-adding other epochs of WISE data. Very fast moving objects (motions of many arcseconds per year or larger) will appear unsubtracted, while slower-moving sources (down to a few hundred mas yr^{-1}) will manifest as partially subtracted “dipoles.” The blue (red) channel represents W1 (W2), so that redder (i.e., colder) moving objects will appear distinctively orange.²⁰

Although Backyard Worlds places substantial emphasis on discovering very cold and close Y dwarfs, participants are encouraged to report any moving object not presented in the prior literature (i.e., not in the SIMBAD database; Wenger et al. 2000). Examples include comoving substellar companions to higher-mass primaries (e.g., Faherty et al. 2020), white dwarfs with infrared excesses (e.g., Debes et al. 2019), and hypothesized planets in the outer solar system (e.g., Matese et al. 1999; Matese & Whitmire 2011; Luhman 2014a; Batygin & Brown 2016; Meisner et al. 2017, 2018a).

As of 2020 April, Backyard Worlds counts more than 58,000 registered users, with the number of unique participants (including those not registered) estimated to be several times larger. Among these participants are ~ 200 advanced users who collaborate closely with one another and the science team. Advanced users have created a number of custom motion search tools that expand the Backyard Worlds effort significantly beyond its presence on the Zooniverse web portal (e.g., WiseView; Caselden et al. 2018) and often make use of catalog

¹⁹ The locations are truly random; there is no preselection of the flipbook footprints to, e.g., be centered on a suspected brown dwarf candidate.

²⁰ The Backyard Worlds documentation at <https://www.zooniverse.org/projects/marckuchner/backyard-worlds-planet-9/about/research> contains example images illustrating this color scheme and the appearance of dipoles and fast movers in our flipbooks.

querying interfaces such as SIMBAD, IRSA, VizieR (Ochsenbein et al. 2000), and the Astro Data Lab (Fitzpatrick et al. 2014). See Figure 1 of Kuchner et al. (2017) for an example Backyard Worlds flipbook image and Figure 1 of Meisner et al. (2020) for an example WiseView image sequence.

4. Spitzer Target Selection

Our Spitzer follow-up consists of two separate observing campaigns, programs 14076 and 14299, which we will refer to as p14076 and p14299 (PI: Faherty in both cases). Target selection for both campaigns was essentially the same, though performed at different times: p14076 (p14299) targets were selected in 2018 March (2019 April).

Backyard Worlds maintains a running list of all user-submitted, previously unpublished candidate moving objects with motions that have been visually confirmed by our science team and archival photometry suggesting L, T, or Y spectral types. This list currently contains ~ 1600 newly discovered brown dwarf candidates and represents the parent sample from which we selected our Spitzer photometry targets. At the time of p14076 (p14299) target selection, this parent sample of Backyard Worlds discoveries included ~ 800 (~ 1200) brown dwarf candidates.

The primary goal of our Spitzer photometry campaigns was to pinpoint the strongest Y dwarf candidates among our moving object discoveries. As such, the majority of our targets were selected because they bear the hallmarks of potential Y dwarfs: detected only in W2 (undetected in W1 and other optical/infrared surveys) and exhibiting clear motion consistent with that of a brown dwarf in the solar neighborhood. Additionally, we selected some Spitzer targets that have a faint W1 counterpart visible if any of the following three conditions were met: the crude phototype based on W1–W2 color suggested possible membership within the 20 pc sample, the candidate appeared to be a potential common proper motion (CPM) companion to another moving object, and the motion was exceptionally large ($\mu \gtrsim 1'' \text{ yr}^{-1}$). With these selection rules in mind, we reexamined our full list of Backyard Worlds discoveries prior to each Spitzer campaign’s proposal submission and requested observations for those objects that matched our criteria for meriting Spitzer follow-up. One major driver behind our p14299 effort was the desire to phototype relatively recent Backyard Worlds discoveries before the impending retirement of Spitzer.

We do not expect our brown dwarf target list to be contaminated by W2-only solar system objects. Because their apparent motions are so large, inner solar system objects are entirely nulled out by our co-addition of WISE data into daily intervals. At Kuiper Belt distances, faint solar system objects should also be largely removed by our stacking, and their degree-scale parallaxes easily distinguish them from brown dwarfs in the solar neighborhood. At distances of order 1000 au (e.g., Batygin & Brown 2016) a planetary body would remain present in our flipbooks, but the corresponding parallax of several arcminutes would again allow us to separate such a candidate from our brown dwarf targets. For parallaxes of $\sim 1'$ to $\sim 1^\circ$, the WISE data would appear to show one solar system body as a pair of linear tracklets at sky locations offset by roughly twice the parallax. Each of these two apparitions would be perceived during our target vetting visual inspections (performed on isolated arcminute-sized cutouts) as “vanishing” during every other sky pass, which is inconsistent with the

signature of a brown dwarf in the solar neighborhood. Therefore, our Spitzer brown dwarf target sample will exclude objects at a few thousand au or closer even though we have not attempted to perform solar system orbit linking on arcminute or degree angular scales. During our brown dwarf target selection process, sources alternating in sky position by a few arcminutes or more from one sky pass to the next would generally have been discarded and presumed to be “latent” detector artifacts, which were found to be a common contaminant in the WISE Planet 9 search of Meisner et al. (2017). At distances of $\sim 10,000$ – $30,000$ au (e.g., Matese & Whitmire 2011), the trajectory of a solar companion would be dominated by many arcseconds of oscillatory parallactic motion, but none of our Spitzer targets display such behavior.

We ultimately selected 65 targets for p14076 and 33 targets for p14299. p14299 inadvertently retargeted two objects from p14076 (WISEA 0651–8355 and WISEA 1627–2443), meaning that our full Spitzer follow-up sample contains 96 unique sources. The sample presented in this work additionally includes one object (CWISE 0002+6352) for which we have analyzed serendipitous archival Spitzer imaging from the GLIMPSE360 program (Churchwell et al. 2009).

During p14299 target selection, we sought to avoid duplicating any objects already slated for Spitzer observations by the CatWISE team (Spitzer program 14034, p14034 for short; Eisenhardt et al. 2020; Meisner et al. 2020). The Backyard Worlds and CatWISE moving object discovery lists overlap extensively, since both projects seek to uncover faint brown dwarfs using motions spanning the combined WISE +NEOWISE time baseline.

5. Spitzer Target Sample Properties

In our estimation, the combined p14076+p14299 sample is best viewed as effectively AllWISE selected, resulting from a combination of numerous AllWISE queries issued by Backyard Worlds advanced users. A total of 91% (87/96) of our discoveries are present in the AllWISE catalog, despite the fact that the full WISE+NEOWISE data set now contains $>2\times$ more securely detected sources than AllWISE (Schlafly et al. 2019). The discoveries of four of our nine targets not in AllWISE (WISEU 0019–0943, WISEU 0055+5847, WISEU 0505+3043, WISEU 2150–7520) are readily explained by dedicated CPM searches where WISE visual inspection was seeded by the Gaia DR2 (Gaia Collaboration et al. 2016, 2018) catalog of higher-mass objects in the solar neighborhood.

Because our Spitzer target selection was finalized before the public release of CatWISE (Eisenhardt et al. 2020) and we believe our sample to be largely AllWISE selected, we adopt AllWISE designations for our discoveries when available. In the absence of an AllWISE counterpart, we then use the CatWISE designation if one is available, and we finally employ unWISE Catalog designations when neither AllWISE nor CatWISE contains a counterpart.

Our sample’s spatial distribution in Galactic coordinates is shown in Figure 1. As expected, our brown dwarf candidates are scattered across the entire sky, with a significant underdensity in the crowded Galactic plane—only 6% (6/97) of objects inhabit the $|b_{\text{gal}}| < 10^\circ$ sky region that accounts for 17% of the sky. There also appears to be somewhat of an overdensity toward the south Galactic cap.

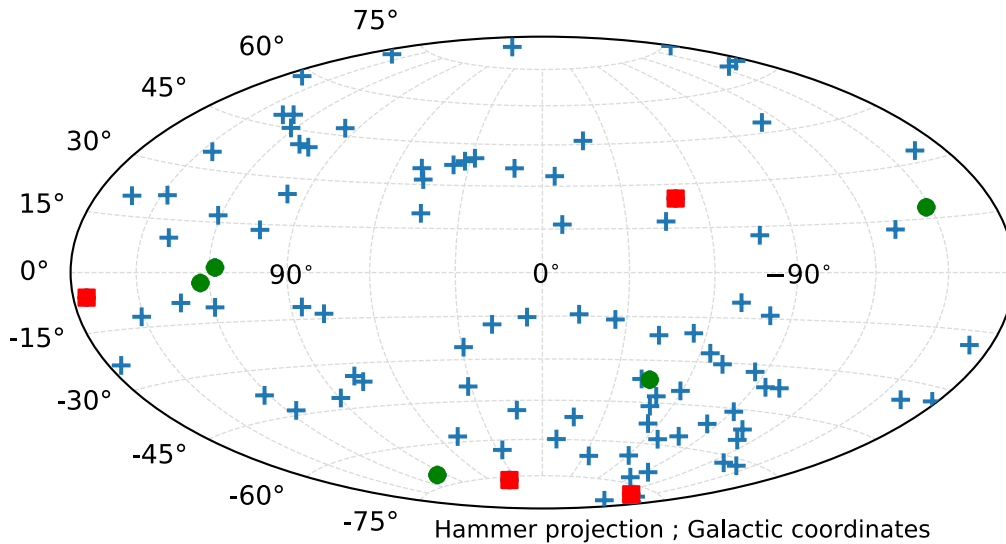


Figure 1. Full-sky distribution of all 96 Backyard Worlds targets followed up with Spitzer programs 14076 and 14299, plus one discovery (CWISE 0002+6352) with archival Spitzer data, in Galactic Hammer projection. CPM candidates are denoted by green circles. Red squares are spurious candidates (Table 1) for which no Spitzer counterpart was found. The locations of all other brown dwarf candidates are shown as blue plus signs.

5.1. Targets Previously Presented by Backyard Worlds

The discoveries of six of our targets have been previously published by our team: WISEU 2150–7520 in Faherty et al. (2020) plus WISEA 0014+7951, WISEA 0830+2837, WISEA 0830–6323, WISEA 1516+7217, and WISEA 1525+6053 in Bardalez Gagliuffi et al. (2020). These prior publications should be considered the definitive references for WISEU 2150–7520 and WISEA 0830+2837, as they contain more detailed treatments of these objects. For WISEA 0014+7951, WISEA 0830–6323, WISEA 1516+7217, and WISEA 1525+6053, the present work provides significant new information by motion-confirming these targets and supplying more accurate WISE+Spitzer proper-motion measurements for them.

5.2. Overlap with Previously Published CatWISE Spitzer Follow-up

Although we intended to avoid duplicating any Spitzer follow-up of brown dwarf discoveries already published by the CatWISE team (Marocco et al. 2019, 2020; Meisner et al. 2020), we inadvertently targeted CWISEP 1359–4352 in p14299. We nevertheless propagate this object through our entire analysis pipeline in this work, since its p14299 Spitzer photometry is deeper than the p14034 photometry initially presented in Meisner et al. (2020).

5.3. Spurious Candidates

Four brown dwarf candidates were found to have no Spitzer counterpart (see Table 1 and Section 7). These spurious candidates are thought to be very faint noise excursions or artifacts in the WISE data. In addition to the targets in Table 1, WISEA J162716.41–244355.4 clearly has an extended morphology based on our Spitzer imaging and is therefore presumed to be a piece of nebulosity in the ρ Ophiuchi molecular cloud complex rather than a moving object.

5.4. WISE Photometry

Table 2 provides WISE photometry for our entire sample of 96 targets. In gathering WISE photometry, we gave preference

Table 1
Targets without Any Spitzer Counterpart

AOR	Designation	W2 (mag)
70080512	WISEA J014614.70–290048.4	16.49 ± 0.20
70082560	WISEU J050511.06+304355.6	16.38 ± 0.12
70084096	WISEA J132441.18–372024.8	16.25 ± 0.19
70083072	WISEA J235136.37–250247.6	16.14 ± 0.19

Note. Each object’s designation prefix corresponds to the WISE catalog from which the quoted W2 magnitude has been drawn.

(This table is available in machine-readable form.)

to CatWISE photometry when available, since CatWISE fluxes are fit to linearly moving profiles that account for source motion and CatWISE incorporates $4\times$ more input W1/W2 imaging than AllWISE. In the absence of CatWISE photometry, we next checked AllWISE for photometry. In the event that neither CatWISE nor AllWISE photometry was available, we use photometry from the unWISE Catalog (Schlafly et al. 2019). Note that the unWISE Catalog performs source detection and photometry independently in W1 and W2, and so a few objects in Table 2 have W2 photometry from the unWISE Catalog but no corresponding W1 photometry. Also note that in general the identifier prefixes we have chosen (typically WISEA for AllWISE) do not correspond to the origin of the WISE photometry listed in Table 2 (typically CatWISE). For WISEU 2150–7520 we report the custom WISE photometry from Faherty et al. (2020). Table 2 lists the origin of WISE photometry reported for each target. All magnitudes quoted throughout this paper are in the Vega system unless otherwise noted.

Figure 2 shows a histogram of the W2 magnitudes of the 96 new discoveries in our sample. The median W2 magnitude of this sample is $W2 = 15.70$ mag. This is much fainter than all prior full-sky WISE motion searches except for Meisner et al. (2020), which had a median W2 magnitude of $W2 = 15.93$ mag. Both Backyard Worlds and CatWISE have been able to push much fainter than previous full-sky WISE motion

Table 2
Mid-infrared Photometry from WISE and Spitzer

Name	Motion Confirmed	W1 (mag)	W2 (mag)	W1–W2 (mag)	AOR	ch1 (mag)	ch2 (mag)	ch1–ch2 (mag)	WISE Phot. Reference ^c
CWISE J000229.93+635217.0	yes	18.21 ± 0.21	15.73 ± 0.05 ^b	2.48 ± 0.22	38724864	17.349 ± 0.246	15.690 ± 0.055	1.659 ± 0.252	6
WISEA J001449.96+795116.1	yes	18.72 ± 0.28	16.00 ± 0.06	2.72 ± 0.28	65969152	17.752 ± 0.059	15.863 ± 0.019	1.890 ± 0.062	1
WISEU J001908.31–094323.3	yes	18.33 ± 0.17	15.81 ± 0.07 ^b	2.52 ± 0.19	70084352	17.119 ± 0.034	15.666 ± 0.019	1.453 ± 0.038	2
WISEA J002810.59+521853.1	yes	18.05 ± 0.13	15.60 ± 0.05	2.45 ± 0.14	68143872	17.360 ± 0.043	15.669 ± 0.019	1.691 ± 0.046	1
WISEA J002909.90+190516.6	yes	17.58 ± 0.10	15.36 ± 0.05	2.21 ± 0.11	65969664	16.727 ± 0.025	15.301 ± 0.018	1.426 ± 0.032	1
WISEA J003631.29–642735.6	no	18.31 ± 0.16	15.86 ± 0.05	2.45 ± 0.17	70079744	17.203 ± 0.037	15.816 ± 0.019	1.388 ± 0.041	1
WISEU J004851.21+250814.9	yes	...	15.04 ± 0.03 ^b	...	68141824	16.793 ± 0.026	14.743 ± 0.016	2.050 ± 0.031	2
WISEU J005559.88+594745.0	yes	...	15.20 ± 0.03 ^b	...	68141568	16.450 ± 0.021	14.965 ± 0.016	1.485 ± 0.026	2
WISEA J010116.12–520629.8	yes	18.85 ± 0.26	15.88 ± 0.05	2.98 ± 0.27	65970432	17.687 ± 0.056	15.692 ± 0.019	1.994 ± 0.060	1
WISEA J012057.06–764216.4	yes	18.87 ± 0.21	15.87 ± 0.05	2.99 ± 0.22	65970944	17.663 ± 0.056	15.790 ± 0.019	1.874 ± 0.059	1
WISEA J012834.87–280302.5	yes	17.47 ± 0.09	15.55 ± 0.05	1.92 ± 0.10	70085632	16.722 ± 0.025	15.511 ± 0.018	1.211 ± 0.032	1
WISEA J013217.78–581825.9	yes	19.10 ± 0.43	15.72 ± 0.05	3.38 ± 0.43	65971200	17.882 ± 0.064	15.740 ± 0.019	2.141 ± 0.067	1
WISEU J013522.46–221957.3	yes	...	15.85 ± 0.07 ^b	...	70082048	17.154 ± 0.035	15.793 ± 0.019	1.362 ± 0.039	2
WISEA J013810.78–412220.2	yes	18.40 ± 0.17	16.32 ± 0.09	2.08 ± 0.19	68143616	17.434 ± 0.044	16.198 ± 0.021	1.236 ± 0.049	1
WISEA J014603.23–261908.7	yes	>18.88	15.92 ± 0.07	>2.96	68142080	17.490 ± 0.047	15.810 ± 0.019	1.680 ± 0.052	1
WISEA J015507.35–421635.7	yes	18.91 ± 0.26	16.23 ± 0.08	2.68 ± 0.27	70079488	18.375 ± 0.100	16.165 ± 0.020	2.210 ± 0.102	1
WISEA J015601.22+525304.4	no	17.26 ± 0.07	15.43 ± 0.04	1.83 ± 0.08	70082816	16.697 ± 0.024	15.354 ± 0.018	1.343 ± 0.030	1
WISEA J021420.18–573245.1	yes	18.94 ± 0.24	16.25 ± 0.07	2.69 ± 0.25	65971712	18.075 ± 0.079	16.157 ± 0.020	1.918 ± 0.081	1
WISEA J025756.40–265528.8	yes	18.70 ± 0.33	16.20 ± 0.09	2.50 ± 0.34	68144384	18.302 ± 0.097	15.953 ± 0.019	2.348 ± 0.099	1
WISEA J025805.29–321917.4	yes	16.56 ± 0.04	14.91 ± 0.03 ^b	1.65 ± 0.05	70084608	16.025 ± 0.016	14.988 ± 0.016	1.037 ± 0.023	1
WISEA J030534.09–582635.5	yes	18.29 ± 0.12	15.55 ± 0.03	2.74 ± 0.13	65971968	17.340 ± 0.042	15.515 ± 0.018	1.824 ± 0.046	1
WISEA J032600.28+421056.8	yes	>19.03	15.28 ± 0.04	>3.75	65972224	17.230 ± 0.038	15.292 ± 0.018	1.938 ± 0.042	1
WISEA J032811.00–422321.6	yes	18.56 ± 0.25	16.29 ± 0.07	2.27 ± 0.26	65972480	17.930 ± 0.066	16.026 ± 0.020	1.904 ± 0.069	1
WISEA J034253.20+673143.5	no	17.69 ± 0.10	15.56 ± 0.05	2.12 ± 0.11	70085888	16.488 ± 0.021	15.411 ± 0.018	1.077 ± 0.028	1
WISEA J034227.44–462252.0	yes	18.89 ± 0.32	16.12 ± 0.06	2.77 ± 0.32	70086144	17.714 ± 0.057	16.132 ± 0.021	1.582 ± 0.060	1
WISEA J035410.03–572104.0	no	18.57 ± 0.23	16.10 ± 0.08	2.47 ± 0.24	70085376	17.773 ± 0.061	16.059 ± 0.020	1.714 ± 0.064	1
WISEA J035733.85+070557.4	yes	17.78 ± 0.14	15.37 ± 0.05	2.42 ± 0.14	65972736	16.736 ± 0.026	15.401 ± 0.018	1.335 ± 0.032	1
WISEA J040702.42+190945.8	yes	17.55 ± 0.11	15.55 ± 0.06	2.01 ± 0.13	65972992	16.837 ± 0.027	15.444 ± 0.018	1.392 ± 0.033	1
WISEA J042236.95–044203.5	yes	18.82 ± 0.41	16.02 ± 0.08 ^b	2.80 ± 0.41	68140544	17.694 ± 0.054	15.937 ± 0.020	1.758 ± 0.058	1
WISEA J050238.28+100750.0	yes	18.91 ± 0.51	15.35 ± 0.05	3.56 ± 0.51	65973760	17.520 ± 0.047	15.363 ± 0.018	2.156 ± 0.050	1
WISEU J050305.68–564834.0	yes	...	16.71 ± 0.09 ^b	...	68142592	18.997 ± 0.185	16.022 ± 0.020	2.975 ± 0.185	2
WISEA J050615.56–514521.3	yes	18.49 ± 0.14	16.71 ± 0.10	1.78 ± 0.17	70013696	18.340 ± 0.098	16.233 ± 0.021	2.107 ± 0.100	1
WISEA J053535.43–644518.5	yes	15.26 ± 0.04	15.08 ± 0.03 ^b	0.17 ± 0.04	70083584	15.089 ± 0.012	15.087 ± 0.016	0.002 ± 0.020	1
WISEA J053512.01–773829.7	yes	>19.58	15.90 ± 0.05	>3.68	68142848	18.120 ± 0.082	15.881 ± 0.019	2.240 ± 0.084	1
WISEA J061713.07+670400.8	no	18.22 ± 0.15	15.89 ± 0.06	2.32 ± 0.16	70080000	17.876 ± 0.065	15.972 ± 0.019	1.905 ± 0.068	1
WISEA J064503.72+524054.1	yes	16.85 ± 0.05	15.09 ± 0.03 ^b	1.75 ± 0.06	68144128	17.157 ± 0.035	15.138 ± 0.017	2.019 ± 0.039	4
WISEA J065113.90–835502.6	yes	18.29 ± 0.11	15.61 ± 0.04	2.68 ± 0.12	70013952	17.424 ± 0.043	15.534 ± 0.018	1.889 ± 0.047	1
WISEA J075438.20+090044.9	yes	18.48 ± 0.24	15.78 ± 0.08	2.71 ± 0.25	65974528	17.584 ± 0.049	15.741 ± 0.019	1.844 ± 0.052	1
WISEA J080622.22–082046.5	yes	>18.79	15.49 ± 0.12	>3.31	65974784	17.295 ± 0.041	15.411 ± 0.018	1.884 ± 0.045	3
WISEA J083011.95+283716.0	yes	>18.83	15.84 ± 0.14	>2.99	65975296	19.100 ± 0.199	15.845 ± 0.019	3.254 ± 0.200	3
WISEA J083019.97–632305.4	yes	18.12 ± 0.10	15.87 ± 0.04	2.25 ± 0.10	65975040	17.497 ± 0.049	15.675 ± 0.018	1.821 ± 0.052	1
WISEA J084329.01+694709.8	yes	18.23 ± 0.16	16.21 ± 0.08	2.03 ± 0.18	70081792	17.213 ± 0.036	16.013 ± 0.020	1.201 ± 0.042	1
WISEA J101804.20–684254.0	yes	17.41 ± 0.06	15.54 ± 0.03 ^b	1.88 ± 0.07	65975552	17.324 ± 0.043	15.406 ± 0.017	1.918 ± 0.046	1
WISEA J104051.77+450329.3	no	17.89 ± 0.12	15.22 ± 0.04	2.67 ± 0.13	68143104	16.949 ± 0.030	15.285 ± 0.018	1.664 ± 0.034	1

Table 2
(Continued)

Name	Motion Confirmed	W1 (mag)	W2 (mag)	W1–W2 (mag)	AOR	ch1 (mag)	ch2 (mag)	ch1–ch2 (mag)	WISE Phot. Reference ^c
WISEA J104216.89–003935.9	yes	18.07 ± 0.17	15.62 ± 0.05	2.45 ± 0.18	65975808	17.368 ± 0.043	15.745 ± 0.019	1.624 ± 0.047	1
WISEA J105349.41–460241.2	yes	17.18 ± 0.07	15.27 ± 0.04 ^b	1.91 ± 0.08	65976064	17.159 ± 0.035	15.258 ± 0.017	1.901 ± 0.039	1
WISEA J105917.38+285729.3	yes	18.06 ± 0.16	15.60 ± 0.05	2.46 ± 0.16	70083840	17.295 ± 0.039	15.593 ± 0.019	1.702 ± 0.043	1
WISEA J110201.76+350335.4	yes	18.32 ± 0.27	15.18 ± 0.04	3.14 ± 0.27	65976320	17.278 ± 0.038	15.132 ± 0.017	2.147 ± 0.043	1
WISEA J112440.19+663052.0	yes	18.11 ± 0.13	15.40 ± 0.04	2.71 ± 0.13	70016512	17.162 ± 0.035	15.319 ± 0.017	1.844 ± 0.039	1
WISEA J114350.90+401333.9	yes	18.45 ± 0.28	15.59 ± 0.05	2.86 ± 0.29	65977344	17.397 ± 0.042	15.486 ± 0.018	1.911 ± 0.046	1
WISEA J114601.22+342458.8	yes	18.08 ± 0.14	15.62 ± 0.06	2.46 ± 0.15	65977600	16.899 ± 0.029	15.447 ± 0.018	1.452 ± 0.034	1
WISEA J115917.89+671704.2	yes	19.20 ± 0.43	16.14 ± 0.07	3.06 ± 0.44	65977856	18.129 ± 0.081	15.951 ± 0.019	2.178 ± 0.083	1
WISEA J125721.01+715349.3	yes	19.01 ± 0.24	16.11 ± 0.06	2.90 ± 0.24	65978112	18.889 ± 0.162	16.158 ± 0.021	2.731 ± 0.163	1
WISEA J131102.03+312107.9	no	19.11 ± 0.47	15.76 ± 0.06	3.35 ± 0.48	70085120	17.587 ± 0.049	15.741 ± 0.019	1.846 ± 0.052	1
WISEA J135042.33–830202.8	no	19.30 ± 0.49	16.78 ± 0.19	2.52 ± 0.52	70084864	17.728 ± 0.056	16.785 ± 0.026	0.943 ± 0.062	3
CWISEP J135937.65–435226.9 ^a	yes	>18.37	16.13 ± 0.08	>2.24	70079232	18.169 ± 0.083	15.920 ± 0.019	2.249 ± 0.085	1
WISEA J143422.31–083934.2	yes	>18.52	16.02 ± 0.08	>2.50	65978368	17.930 ± 0.068	15.855 ± 0.019	2.075 ± 0.071	1
WISEA J151620.39+721745.4	yes	18.91 ± 0.17	16.13 ± 0.05	2.79 ± 0.18	65978624	18.170 ± 0.084	15.946 ± 0.019	2.224 ± 0.086	1
WISEA J152529.09+605356.5	yes	>19.67	15.99 ± 0.05	>3.68	65978880	18.024 ± 0.073	15.883 ± 0.019	2.141 ± 0.076	1
WISEAR J154025.77–113940.8	yes	18.20 ± 0.21	16.06 ± 0.10	2.14 ± 0.23	68143360	17.417 ± 0.044	15.927 ± 0.019	1.489 ± 0.048	1
WISEA J155349.96+693355.2	yes	16.48 ± 0.03	15.49 ± 0.03 ^b	0.99 ± 0.04	65979136	16.324 ± 0.019	15.458 ± 0.018	0.865 ± 0.026	1
WISEA J160516.79+002139.0	yes	18.37 ± 0.20	15.46 ± 0.05	2.90 ± 0.20	65979392	17.403 ± 0.043	15.483 ± 0.018	1.920 ± 0.047	1
WISEA J161940.51+134752.0	no	16.98 ± 0.06	14.74 ± 0.03	2.24 ± 0.06	70019328	16.479 ± 0.021	14.795 ± 0.016	1.684 ± 0.026	1
WISEA J162716.41–244355.4	no	16.37 ± 0.06	13.76 ± 0.02 ^b	2.61 ± 0.06	70019584	16.052 ± 0.019	13.951 ± 0.016	2.102 ± 0.025	1
WISEA J162852.64+160421.0	yes	18.49 ± 0.21	15.90 ± 0.06	2.58 ± 0.22	65980160	17.790 ± 0.060	15.839 ± 0.019	1.951 ± 0.063	1
WISEA J163932.75+184049.4	yes	18.09 ± 0.19	15.50 ± 0.04	2.59 ± 0.19	65980416	17.656 ± 0.052	15.371 ± 0.017	2.285 ± 0.054	1
WISEA J165902.66+274747.9	no	>19.23	16.06 ± 0.07 ^b	>3.17	70081536	17.843 ± 0.061	15.961 ± 0.019	1.882 ± 0.064	1
WISEA J171331.68+245000.9	yes	19.12 ± 0.36	15.98 ± 0.06	3.14 ± 0.37	65980672	17.524 ± 0.047	15.842 ± 0.019	1.681 ± 0.052	1
WISEA J172907.10–753017.0	yes	17.36 ± 0.07	15.48 ± 0.04	1.87 ± 0.08	70080256	16.848 ± 0.027	15.420 ± 0.018	1.428 ± 0.032	1
WISEA J175328.55–590447.6	yes	>19.00	15.58 ± 0.05	>3.42	68144640	17.336 ± 0.039	15.186 ± 0.017	2.150 ± 0.043	1
WISEA J175701.50+183215.2	no	18.49 ± 0.21	15.72 ± 0.05 ^b	2.77 ± 0.22	68141312	17.863 ± 0.062	15.726 ± 0.019	2.138 ± 0.065	1
WISEA J181849.59–470146.9	yes	18.51 ± 0.51	15.14 ± 0.08 ^b	3.37 ± 0.52	65980928	17.100 ± 0.034	15.066 ± 0.016	2.034 ± 0.038	3
WISEA J185109.93+671343.7	no	17.29 ± 0.04	16.71 ± 0.07	0.58 ± 0.08	65981184	17.142 ± 0.036	16.414 ± 0.023	0.728 ± 0.043	1
WISEA J190005.76–310810.9	yes	18.42 ± 0.36	14.92 ± 0.04	3.50 ± 0.36	65981440	16.852 ± 0.028	14.787 ± 0.016	2.064 ± 0.032	1
WISEA J193054.55–205949.4	yes	>18.80	15.24 ± 0.05 ^b	>3.56	65981696	18.417 ± 0.104	15.250 ± 0.017	3.168 ± 0.105	1
WISEA J201833.67–141720.3	yes	>18.57	15.06 ± 0.04	>3.51	65981952	17.166 ± 0.036	14.997 ± 0.016	2.168 ± 0.040	1
WISEA J205921.85+662725.2	yes	18.71 ± 0.18	15.70 ± 0.04	3.02 ± 0.18	65982208	17.414 ± 0.042	15.526 ± 0.018	1.888 ± 0.046	1
WISEA J211456.86–180519.0	yes	18.12 ± 0.19	14.97 ± 0.04	3.15 ± 0.19	65982464	16.791 ± 0.026	14.938 ± 0.016	1.853 ± 0.031	1
WISEA J212020.71+303656.2	no	17.13 ± 0.06	15.53 ± 0.05	1.60 ± 0.08	70081280	16.258 ± 0.020	15.255 ± 0.017	1.003 ± 0.025	1
WISEA J212510.91–730758.8	yes	18.27 ± 0.16	15.62 ± 0.05	2.65 ± 0.17	65982720	17.372 ± 0.043	15.561 ± 0.018	1.812 ± 0.047	1
WISEA J213810.99+373312.9	no	17.32 ± 0.07	15.75 ± 0.05	1.57 ± 0.08	70081024	17.281 ± 0.041	15.888 ± 0.019	1.394 ± 0.045	1
WISEA J214025.23–332707.4	yes	18.90 ± 0.51	16.10 ± 0.10	2.80 ± 0.52	70080768	18.130 ± 0.082	16.122 ± 0.021	2.008 ± 0.086	1
WISEU J215018.46–752053.0	yes	18.18 ± 0.15	15.81 ± 0.05 ^b	2.37 ± 0.16	68140800	17.020 ± 0.036	15.632 ± 0.018	1.388 ± 0.041	5
WISEAR J220746.67–503631.7	yes	>19.09	16.16 ± 0.09	>2.94	68141056	17.664 ± 0.052	16.001 ± 0.019	1.663 ± 0.056	1
WISEA J221859.33+114644.4	yes	17.90 ± 0.14	15.04 ± 0.03	2.85 ± 0.14	65983232	16.490 ± 0.021	14.889 ± 0.016	1.602 ± 0.027	1
WISEA J221841.38+143003.4	yes	17.23 ± 0.07	15.15 ± 0.04	2.07 ± 0.08	70082304	16.896 ± 0.030	15.281 ± 0.017	1.615 ± 0.034	1
WISEA J224319.56–145857.3	yes	17.91 ± 0.24	15.39 ± 0.05	2.52 ± 0.24	65984000	17.765 ± 0.058	15.336 ± 0.018	2.429 ± 0.060	1
WISEU J224547.11–433341.5	yes	...	15.60 ± 0.05 ^b	...	68142336	...	15.029 ± 0.017	...	2

Table 2
(Continued)

Name	Motion Confirmed	W1 (mag)	W2 (mag)	W1–W2 (mag)	AOR	ch1 (mag)	ch2 (mag)	ch1–ch2 (mag)	WISE Phot. Reference ^c
WISEA J225404.16–265257.5	yes	18.20 ± 0.19	15.38 ± 0.05	2.81 ± 0.20	65984512	17.467 ± 0.046	15.200 ± 0.017	2.267 ± 0.049	1
WISEA J230930.58+145633.1	yes	17.96 ± 0.14	15.64 ± 0.06	2.32 ± 0.15	65984768	16.867 ± 0.027	15.455 ± 0.018	1.411 ± 0.033	1
WISEA J233816.47–732929.7	yes	18.37 ± 0.23	15.48 ± 0.04 ^b	2.88 ± 0.23	65985024	17.628 ± 0.052	15.525 ± 0.018	2.102 ± 0.055	1
WISEA J235120.62–700025.8	no	19.12 ± 0.38	15.66 ± 0.04	3.47 ± 0.38	70083328	18.415 ± 0.109	15.708 ± 0.019	2.707 ± 0.111	1
WISEA J235456.63–481440.1	yes	18.55 ± 0.20	15.89 ± 0.06	2.66 ± 0.21	65985536	18.086 ± 0.078	15.850 ± 0.019	2.236 ± 0.080	1

Notes.

^a The discovery of CWISEP J135937.65–435226.9 was presented in Meisner et al. (2020), but its more recent p14299 Spitzer photometry provided here is deeper than that of Meisner et al. (2020).

^b WISE photometry is or may be contaminated by blending.

^c Reference for WISE photometry: 1 = CatWISE Preliminary catalog; 2 = unWISE Catalog; 3 = AllWISE catalog; 4 = CatWISE Preliminary catalog reject table; 5 = Faherty et al. (2020); 6 = CatWISE 2020 catalog.

(This table is available in machine-readable form.)

7

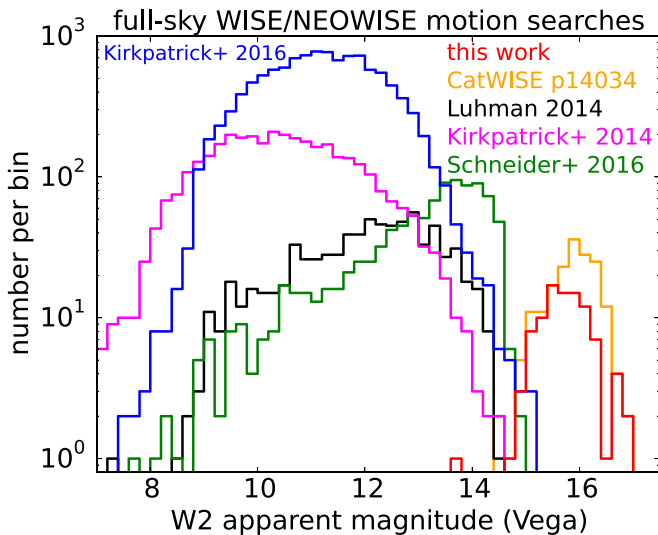


Figure 2. W2 magnitude distributions of full-sky WISE/NEOWISE motion survey samples (logarithmic vertical axis scale). The red histogram represents our 95 Backyard Worlds discoveries followed up with Spitzer p14076 and p14299, plus one with archival Spitzer data (CWISE 0002+6352). The Backyard Worlds targets are much fainter than those of all prior samples except for CatWISE (Spitzer program 14034; Meisner et al. 2020).

searches because they make use of time-resolved unWISE co-add images (Meisner et al. 2018b, 2018c, 2019) spanning the full WISE+NEOWISE baseline.

6. Spitzer Observing Strategy

The primary goal of our Spitzer follow-up is to obtain photometric spectral type estimates, which we typically cannot determine from WISE because our targets generally lack secure W1 detections. Spitzer ch1–ch2 color tends to increase monotonically toward later spectral types, and so we can use the Kirkpatrick et al. (2019) relation for spectral type as a function of ch1–ch2 color to phototype our brown dwarf candidates.

We adopted a simplistic observing strategy whereby every target is observed using the exact same Spitzer dithering sequence—no scaling of the total exposure time (or number of dithers) per target was performed based on anticipated Spitzer brightness/color. We opted for a per-target Astronomical Observation Request (AOR) consisting of a “Spiral16” dither pattern with “medium” scale and a 30 s frame time per channel per dither.

The total exposure time per target in ch1 was engineered to ensure that our Spitzer photometry can distinguish between late T and Y dwarfs, even for our faintest targets. The Spitzer color “boundary” between late T and Y dwarfs occurs at ch1–ch2 ≈ 2.4 mag (Kirkpatrick et al. 2019). In our observation planning, we assume that ch2 \approx W2, as is typical for mid-T and later brown dwarfs (Kirkpatrick et al. 2019). The faintest W2 magnitude among our targets is W2 = 16.78, so we budget to achieve a ch1 signal-to-noise ratio (S/N) of 5 near the T/Y boundary according to ch1(S/N = 5) = 16.78 + 2.4 = 19.18. Our past Spitzer observing campaigns (e.g., program 70062) have indicated that obtaining five dithers with 30 s frame times achieves S/N = 5 at ch1 = 18.75. Assuming that depth scales with the square root of the number of dithers, 16 dithers would then go 0.63 mag deeper at 5 σ , yielding an expected 5 σ ch1 threshold of 19.38 mag, exceeding that desired with a margin

of 0.2 mag. This margin can help accommodate depth variations due to factors such as zodiacal background or diffuse emission near the Galactic plane. Our targets have median ch2 ≈ 15.6 and median ch1–ch2 ≈ 1.9 (Table 2), so we typically obtain a ch1 uncertainty of ~ 0.04 – 0.05 mag (see Section 7), corresponding to ch1 S/N of ~ 20 – 25 .

7. Spitzer Photometry

Spitzer photometry is performed according to Section 5.1 of Kirkpatrick et al. (2019). In brief, we construct a custom mosaic for each target in each of ch1 and ch2 using the MOsaicker and Point Source EXtractor (MOPEX; Makovoz & Khan 2005) software package. For a few targets, we specially remove one or a small number of dithers where the ch1 counterpart’s immediate vicinity happened to be corrupted by a cosmic ray or glint. We then perform source detection and photometry with MOPEX/APEX (Makovoz & Marleau 2005). We tabulate both point-response function (PRF) and aperture photometry for extracted sources and apply the appropriate aperture correction to our aperture fluxes to obtain their equivalent total fluxes. Table 2 lists our final Spitzer photometry results, where we have averaged each target’s PRF and aperture photometry quantities to arrive at the quoted values. In the case of CWISE 0002+6352, we simply quote the PRF photometry, since the aperture photometry is contaminated by a nearby source.

We adopted a default source detection threshold of S/N = 5, but two exceptionally red targets required decreasing this threshold to S/N = 2: WISEU 0503–5648 and WISEA 1930–2059.

WISEU 2245–4333 is severely blended with a brighter neighboring source at our Spitzer epoch, such that we are only able to extract photometry in ch2 but not in ch1. Unfortunately, this means that we cannot obtain a Spitzer-based phototype for this source, or estimates of any other derived quantities that require a ch1–ch2 color measurement (e.g., photometric distance and effective temperature).

8. Spectroscopic Follow-Up

8.1. Magellan FIRE Spectroscopy

We used the 6.5 m Baade Magellan telescope and the Folded-port InfraRed Echelle (FIRE; Simcoe et al. 2013) spectrograph to obtain NIR spectra of eight objects on our Spitzer programs (see Table 3). Observations were made for four sources on 2018 December 1 under clear conditions and an additional four sources under poor conditions: one object on 2019 December 10 and three objects on 2019 December 12. For all observations, we used the prism mode and the 0.6 slit (resolution $\lambda/\Delta\lambda \sim 100$) covering the full 0.8–2.5 μm band. We observed all objects using a standard ABBA nod pattern with an exposure time of 120 s per nod. We observed an A0 standard star after each target for telluric corrections and obtained an Ne Ar lamp spectrum for wavelength calibration. At the start of the night we used quartz lamps as dome flats in order to calibrate pixel-to-pixel response. Data were reduced using the FIREHOSE package, which is based on the MASE and Spextool reduction packages (Vacca et al. 2003; Cushing et al. 2004; Bochanski et al. 2009).

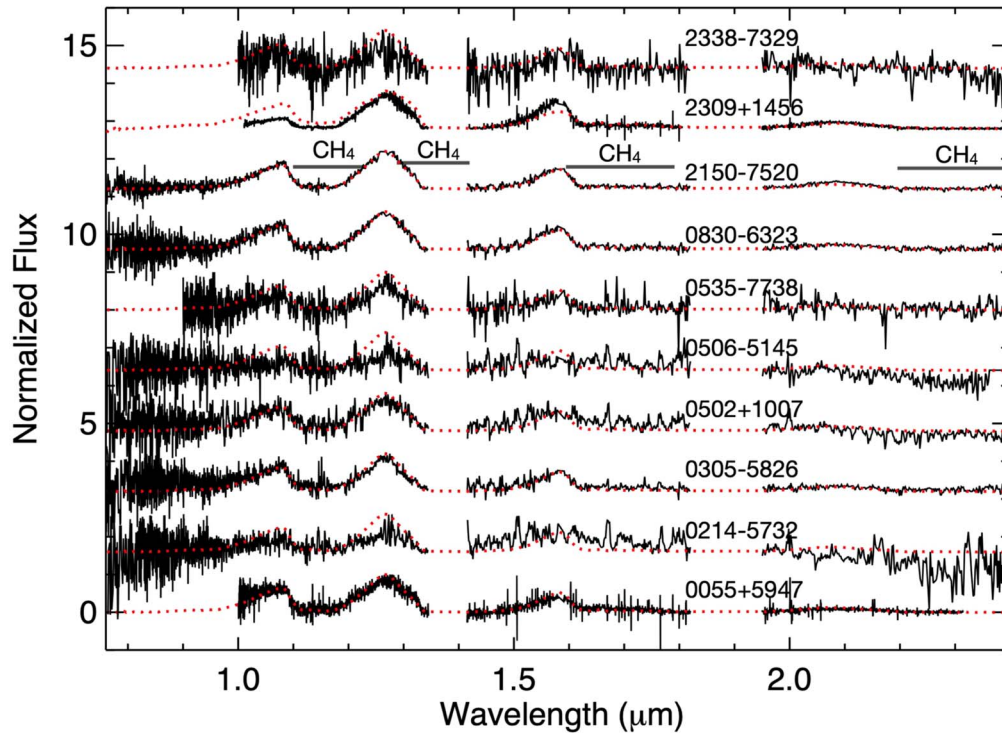


Figure 3. All spectra obtained for this sample (both FIRE and NIRES) plotted in order of decreasing R.A. The quality of the data varies by conditions at the telescope (see Table 3) and faintness of each source. Overplotted on each is the T8 standard 2MASS J0415195–093506 (red curve) from Burgasser et al. (2004). All sources are ± 1 subtype from a T8; therefore, it is a comparison for all. Regions impacted by telluric absorption are removed (at ~ 1.4 and $\sim 1.9 \mu\text{m}$).

Table 3
Details on Spectroscopic Follow-Up

Name (1)	Telescope (2)	Instrument (3)	Date (4)	Exp(s) (5)	Frames (6)	Telluric (7)	Conditions (8)	SpT (9)
WISEU J005559.88+594745.0	KECK II	NIRES	2019 Oct 28	300	3	HD 5071	Clear	T8
WISEA J021420.18–573245.1	Baade	FIRE	2019 Dec 12	120	6	HD 23722	Poor	>T6
WISEA J030534.09–582635.5	Baade	FIRE	2018 Dec 1	120	8	HD 53607	Clear	T8
WISEA J050238.28+100750.0	Baade	FIRE	2019 Dec 10	120	6	HD 287640	Poor	>T6
WISEA J050615.56–514521.3	Baade	FIRE	2019 Dec 12	120	5	HD 60331	Poor	\geq T8
WISEA J053512.01–773829.7	Baade	FIRE	2018 Dec 1	120	8	HD 90104	Clear	\geq T8
WISEA J083019.97–632305.4	Baade	FIRE	2018 Dec 1	120	6	HD 45647	Clear	T8-T9
WISEU J215018.46–752053.0 ^a	Baade	FIRE	2018 Dec 1	120	6	HD 200523	Clear	T8
WISEA J230930.58+145633.1	KECK II	NIRES	2018 Sept 1	300	12	HD 7215	Clear	T8
WISEA J233816.47–732929.7	Baade	FIRE	2019 Dec 12	120	4	HD 23722	Poor	>T6

Note.

^a See Faherty et al. (2020) for details on this system.

(This table is available in machine-readable form.)

8.2. Keck NIRES Spectroscopy

We used the Keck II telescope and the Near-Infrared Echellette Spectrometer (NIRES; Wilson et al. 2004) on 2019 October 28 and 2018 September 1 to obtain 0.94–2.45 μm NIR spectra of two objects (see Table 3). All components on NIRES are fixed with a $0''.55$ slit producing resolution ~ 2700 data. All sources were identified using the K -band finder camera and observed in an ABBA nod pattern. Exposure times and AB frames acquired are listed in Table 3. The data were reduced using a modified version of Spextool (Cushing et al. 2004; see also Section 4.4 of Kirkpatrick et al. 2011), following the standard procedure. Wavelength calibration was determined using telluric lines. The spectra of each A–B pair were

extracted individually and then combined with the other extracted pairs. The telluric correction procedure was carried out as detailed in Vacca et al. (2003).

8.3. Spectra Results

We show all spectra obtained for this Spitzer sample in Figure 3. Objects are arranged in order of decreasing R.A. from top to bottom. Several objects were observed under poor weather conditions (see Table 3), and therefore the quality of their data is diminished, especially at H and K bands (e.g., WISEA J021420.18–573245.1). Regardless, all objects show clear CH_4 absorption in J band, and we can confirm all of them to be late T dwarfs. We compared each object against the T

dwarf spectral standards in the SpeX prism library and list our best-fit type in Table 3.

For uniform comparison in Figure 3, we overplot the T8 standard 2MASS J0415195–093506 (red curve) from Burgasser et al. (2004) on each object. All sources are classified as T8, within one subtype of T8, or broadly defined as a late T dwarf, and therefore our standard choice serves as a robust comparative object. Several sources are high S/N (>10 across the wavelength coverage) and well fit to the T8 standard (within one spectral type). These include WISE J215018.46–752053.0, which was the subject of Faherty et al. (2020) as it was discovered to be comoving with a Gaia DR2 L1 dwarf; WISEA J083019.97–632305.4, which has Hubble Space Telescope (HST) photometry reported in Bardalez Gagliuffi et al. (2020) consistent with a late T dwarf; and WISEU J005559.88+594745.0, which is a new comoving companion reported in this paper (see Section 11.6.3). WISEA J083019.97–632305.4 and WISEU J005559.88+594745.0 both have J -, H -, and K -band spectra with clear and strong CH_4 absorption consistent with the standard, implying that they are field sources with no unusual parameters.

In the case of WISEA J021420.18–573245.1, WISEA J050238.28+100750.0, and WISEA J233816.47–732929.7 the spectra are too noisy to ascertain an exact type. Each of these sources is notably later than T6. In the case of WISEA J050615.56–514521.3, WISEA J053512.01–773829.7, and WISEA J083019.97–632305.4 these sources are all at least T8 but possibly later. Finally, WISEA J230930.58+145633.1 is best fit by the T8 standard. This source and WISE J00559.88+594745.0 were collected using the NIRES instrument on Keck II. Unlike the FIRE prism spectra shown for all other sources, the Keck NIRES spectra are stitched together from cross-dispersed orders. This can (although not always) lead to poorly fit continuum shapes where order overlaps were deprecated by low-S/N sources. WISEA J230930.58+145633.1 appears to have slightly depleted J -band flux and enhanced H - and K -band flux; however, this may be due to stitching in the merged spectrum of the source. A band-by-band comparison to the standard is more compatible, and therefore we do not conclude that this object is necessarily peculiar.

9. Astrometry

9.1. Astrometric Analysis Overview

Because our brown dwarf candidates were selected based on visually perceived source movement, we need a means to quantify our confidence in the motion of each object. This can be accomplished by checking whether or not each target’s joint WISE+Spitzer astrometry falls along a consistent linear trajectory. The combination of Spitzer and WISE data points is critical, since our Spitzer follow-up imaging is completely independent of any anomalous occurrence in the WISE data that may have misled our target selection efforts (e.g., noise, artifacts, blending, imperfect blink registration).

Our targets are (by selection) better detected at 4–5 μm than at 3–4 μm , so we only perform the detailed astrometric analyses of Sections 9.2–9.4 in W2 and ch2. The basic steps of our astrometric analyses are obtaining Gaia-calibrated W2 and ch2 positions spanning the ~ 2010 –2019 time period (Sections 9.2, 9.3) and then fitting these with a linear motion model (Section 9.4). The linear trajectory fitting results can then be used to assess significance of motion as described in Section 9.4. As a by-product, we also obtain more accurate

motion measurements than would be possible using WISE data alone.

9.2. WISE Astrometry

Full details of our W2 astrometry procedure are provided in Section 8.3 of Meisner et al. (2020). Our WISE astrometry is based on catalogs constructed by running the `crowdsourcing` pipeline (Schlafly et al. 2018, 2019) on unWISE co-adds. These unWISE co-adds time-slice the available W2 data in a number of ways, for example, 6-monthly intervals, yearly intervals, the entire pre-hibernation time period, and the entire post-hibernation time period. Detailed definitions of our unWISE time slices for W2 astrometry are provided in Table 5 of Meisner et al. (2020). For each target, we create W2 co-adds and catalogs corresponding to all of these different time slices and then choose a subset of the available W2 detections that best covers the entire WISE/NEOWISE time period while never double-counting any W2 observations. The most common choice is simply a pair of W2 astrometric detections: one for the entire pre-hibernation time period co-added together and another for the entire post-hibernation time period co-added together. In the present work we incorporate the sixth year of WISE data (2017 December–2018 December), whereas Meisner et al. (2020) only used 5 yr of WISE data.

The unWISE co-adds simply propagate the native exposure-level (“Level 1b”) world coordinate system (WCS), which can have systematics at the 100–200 mas level.²¹ We therefore recalibrate our W2 astrometry to Gaia DR2 accounting for the Gaia calibrator proper motions. Note that none of our brown dwarf candidates are detected by Gaia; rather, our astrometry is tied to that of brighter/warmer nearby stars present in Gaia. We typically achieve a W2 versus Gaia bright-end scatter of 40–45 mas per coordinate, just $\sim 1/60$ of the WISE pixel side length. The complete set of W2 (R.A., decl.) coordinates used in our WISE+Spitzer linear motion fits is provided in Table 4.

9.3. Spitzer Astrometry

Our Spitzer astrometry methodology is as described in Section 8.4 of Meisner et al. (2020); here we provide only a concise summary. Our ch2 astrometry is measured from mosaics rather than single-dither Spitzer frames and proceeds from the same set of extracted catalogs used for our ch2 photometry (Section 7). We do not simply adopt the native WCS of the mosaics, which is inherited from that of the single-dither Spitzer frames tied to the Two Micron All Sky Survey (2MASS), since these have astrometry accurate only at the order hundred mas level (Martin et al. 2018). We can achieve much better astrometric accuracy of ~ 20 –25 mas per coordinate by recalibrating the mosaic WCS to Gaia (Martin et al. 2018; Meisner et al. 2020). In detail, we match the ch2 mosaic extractions to Gaia DR2 using the native WCS and then refit six astrometric parameters per mosaic: the WCS CRPIX coordinates (i.e., translations along the two sky directions) and all four CD matrix elements (i.e., scale factors governing the mosaic pixel size and orientation).²² Our fitting minimizes residuals between the WCS-predicted pixel locations of the Gaia DR2 sources (propagated to the relevant Spitzer epoch according to their proper motions) and the measured pixel

²¹ http://wise2.ipac.caltech.edu/docs/release/allwise/expsup/sec5_2b.html

²² See Greisen & Calabretta (2002) for precise definitions of these WCS parameters.

Table 4
Recalibrated WISE W2 Positions

Name	R.A. (deg, ICRS)	Decl. (deg, ICRS)	$\sigma_{\text{R.A.}}$ (mas)	$\sigma_{\text{Decl.}}$ (mas)	Time slice ^a	Mean MJD
CWISE J000229.93+635217.0	0.624757	63.871147	402	389	post0_2yr	56983.52
	0.625715	63.871405	389	374	post1_2yr	57716.24
WISEA J001449.96+795116.1	3.708443	79.854488	432	402	pre	55359.17
	3.711609	79.854339	508	476	post0_1yr	56813.37
	3.712429	79.854352	639	590	post1_1yr	57172.58
	3.712981	79.854583	531	489	post2_1yr	57526.24
	3.713487	79.854231	519	483	post3_1yr	57900.05
	3.715139	79.854420	471	433	post4_1yr	58245.57
WISEU J001908.31−094323.3	4.785193	−9.722557	658	678	pre	55454.78
	4.784726	−9.723279	319	319	post	57566.42
WISEA J002810.59+521853.1	7.044147	52.314851	296	295	pre	55396.93
	7.044060	52.314345	287	285	post	57478.15
WISEA J002909.90+190516.6	7.291288	19.088003	351	357	pre	55467.06
	7.291163	19.087455	222	223	post	57484.91
WISEA J003631.29−642735.6	9.130568	−64.459988	370	359	pre	55438.27
	9.130869	−64.460012	301	285	post	57585.75

Note.

^a See Table 5 of Meisner et al. (2020) for definitions of the WISE/NEOWISE time slices used for W2 astrometry.

(This table is available in its entirety in machine-readable form.)

coordinate centroids. The median per-coordinate astrometric scatter relative to Gaia after our mosaic WCS recalibration is 20 mas.

The complete set of ch2 (R.A., decl.) coordinates used in our WISE+Spitzer linear motion fits is provided in Table 5. The “method number” column of Table 5 is an integer code indicating which set of Gaia DR2 calibrator selection cuts was applied during astrometric recalibration, with these codes defined in Table 6 of Meisner et al. (2020). The N_{calib} column lists the number of Gaia–Spitzer calibrators employed for each target’s mosaic. We sought to always obtain at least five astrometric calibrators per mosaic and only failed to achieve this in one case: WISEA 1627–2443. The lack of calibrators in this field is due to heavy dust extinction within the Gaia bandpass, and in any event WISEA 1627–2443 itself turns out to be an extended piece of nebulosity.

9.4. Linear Motion Fits

We combine our W2 and ch2 astrometry by performing linear fits of the motion along both the R.A. and decl. directions. We do not attempt to include a parallactic motion component in these fits. The fits are performed using weighted linear least squares, where the per-coordinate uncertainties are those listed in Tables 4 and 5. The least-squares fitting propagates these positional uncertainties into formal uncertainties on the R.A. and decl. direction linear motions. No outlier rejection is performed, since we generally have only a handful of astrometric data points per target, and all W2 and ch2 detections used for motion fitting were individually vetted in advance. The best-fit linear motions and their uncertainties are provided in Table 6 for all targets detected in our Spitzer ch2 imaging.

A primary aim of our WISE+Spitzer astrometric analysis is to determine quantitatively whether each target is indeed moving. To do this, we adopt the same significance of motion metric and threshold as in Meisner et al. (2020): $\chi^2_{\text{motion}} > 23.01$, where

$\chi^2_{\text{motion}} = \mu_{\alpha}^2 / \sigma_{\mu_{\alpha}}^2 + \mu_{\delta}^2 / \sigma_{\mu_{\delta}}^2$. This threshold corresponds to a $< 10^{-3}$ probability for random scatter in the linear motion measurement to have induced such a large χ^2_{motion} value for an object that is actually stationary.

Figure 4 shows a histogram of the best-fit total linear motions obtained. Our χ^2_{motion} threshold tends to be exceeded for $\mu_{\text{tot}} \gtrsim 170 \text{ mas yr}^{-1}$ at the typical W2 magnitude of our sample. A total of 79 of our 97 sample members are motion confirmed according to our χ^2_{motion} criterion. One, CWISEP 1359–4352, was previously motion confirmed in Meisner et al. (2020). In another two cases, WISEA 1627–2443 and WISEA 1350–8302, we vetoed the motion confirmation after visual inspection of the Spitzer imaging. WISEA 1627–2443 is seen to be spatially extended at Spitzer resolution, and thus our measured positions likely exhibit excess scatter relative to our positional uncertainties that assume pointlike profiles. This source is presumed to be a piece of nebulosity rather than a moving object. Upon more detailed examination of the W2 and ch2 images of WISEA 1350–8302, we determined that the WISE brown dwarf candidate is actually a very faint $\sim 8''$ separation pair of Spitzer sources, the redder of which we have listed in Table 5. Therefore, the fitted motion is a spurious artifact of comparing the WISE centroid, which effectively averages the positions of two faint Spitzer sources, against the ch2 position of one of those Spitzer objects.

Since we use the same motion confirmation approach and significance threshold as did the CatWISE team for their p14034 Spitzer follow-up (Meisner et al. 2020), it is interesting to compare our fraction of successful motion confirmations to theirs. A total of 64% (114/177) of CatWISE p14034 brown dwarf candidates were motion confirmed, versus 79% (77/97) for our Backyard Worlds Spitzer sample. The higher rate of confirmations for Backyard Worlds likely arises because the CatWISE p14034 sample is fainter by $\sim 0.2\text{--}0.3 \text{ mag}$ in the median, leading to correspondingly noisier WISE astrometry.

Table 5
Spitzer ch2 Coordinates Used in Linear Motion Fits

Name	AOR	R.A. (deg, ICRS)	Decl. (deg, ICRS)	$\sigma_{R.A.}$ (mas)	$\sigma_{Decl.}$ (mas)	MJD	Method Number ^a	N_{calib}
CWISE J000229.93+635217.0	38724864	0.62231037	63.87123123	72	73	55241.26	1	46
WISEA J001449.96+795116.1	65969152	3.71501259	79.85442342	40	37	58468.01	1	23
WISEU J001908.31-094323.3	70084352	4.78470790	-9.72344646	27	37	58797.40	2	11
WISEA J002810.59+521853.1	68143872	7.04428023	52.31384701	32	33	58432.59	1	63
WISEA J002909.90+190516.6	65969664	7.29110034	19.08729895	27	19	58412.28	2	12
WISEA J003631.29-642735.6	70079744	9.13131560	-64.46003825	20	26	58735.08	1	15
WISEU J004851.21+250814.9	68141824	12.21464712	25.13658190	20	20	58422.32	1	11
WISEU J005559.88+594745.0	68141568	14.00051522	59.79578164	23	27	58440.22	1	139
WISEA J010116.12-520629.8	65970432	15.31970026	-52.10773862	37	21	58412.56	1	11
WISEA J012057.06-764216.4	65970944	20.23898676	-76.70398902	44	22	58344.53	1	11
WISEA J012834.87-280302.5	70085632	22.14595356	-28.05033249	22	17	58808.74	3	8
WISEA J013217.78-581825.9	65971200	23.07591639	-58.30725759	20	26	58412.65	1	11
WISEU J013522.46-221957.3	70082048	23.84403267	-22.33314285	23	20	58811.80	3	7
WISEA J013810.78-412220.2	68143616	24.54675533	-41.37159316	32	33	58398.00	3	9
WISEA J014603.23-261908.7	68142080	26.51472397	-26.32003655	26	31	58412.46	3	8
WISEA J015507.35-421635.7	70079488	28.78239170	-42.27671463	23	34	58818.89	3	6
WISEA J015601.22+525304.4	70082816	29.00500275	52.88458715	34	23	58822.17	1	62
WISEA J021420.18-573245.1	65971712	33.58650243	-57.54594570	22	21	58412.73	1	10
WISEA J025756.40-265528.8	68144384	44.48661717	-26.92456171	25	23	58434.94	2	13
WISEA J025805.29-321917.4	70084608	44.52240028	-32.32185488	12	24	58808.58	3	7
WISEA J030534.09-582635.5	65971968	46.39040780	-58.44364855	28	44	58410.04	1	17
WISEA J032600.28+421056.8	65972224	51.50213308	42.18332783	19	21	58469.52	1	34
WISEA J032811.00-422321.6	65972480	52.04717894	-42.38821872	41	32	58420.96	3	6
WISEA J034253.20+673143.5	70085888	55.72223070	67.52862577	22	31	58846.36	1	51
WISEA J034227.44-462252.0	70086144	55.61530679	-46.38068632	27	26	58794.12	2	12
WISEA J035410.03-572104.0	70085376	58.54177590	-57.35152682	21	26	58769.56	2	10
WISEA J035733.85+070557.4	65972736	59.39171212	7.09839040	17	29	58470.54	2	11
WISEA J040702.42+190945.8	65972992	61.76075410	19.16227921	28	19	58471.90	1	20
WISEA J042236.95-044203.5	68140544	65.65671168	-4.70266919	27	28	58467.54	2	10
WISEA J050238.28+100750.0	65973760	75.65912713	10.12998430	16	16	58503.75	1	23
WISEU J050305.68-564834.0	68142592	75.77729216	-56.80850165	27	23	58412.83	1	14
WISEA J050615.56-514521.3	70013696	76.56411289	-51.75649839	24	24	58682.84	1	11
WISEA J053535.43-644518.5	70083584	83.89700202	-64.75446204	37	21	58677.78	1	49
WISEA J053512.01-773829.7	68142848	83.80034174	-77.64100972	25	27	58412.85	1	17
WISEA J061713.07+670400.8	70080000	94.30370110	67.06689045	44	21	58677.47	1	19
WISEA J064503.72+524054.1	68144128	101.26410076	52.67960950	20	26	58507.80	1	19
WISEA J065113.90-835502.6	70013952	102.80363968	-83.91683768	22	25	58679.62	1	25
WISEA J075438.20+090044.9	65974528	118.65971018	9.01182050	25	29	58543.14	1	16
WISEA J080622.22-082046.5	65974784	121.59320085	-8.34964574	23	17	58535.77	1	29
WISEA J083011.95+283716.0	65975296	127.54945237	28.61629645	25	33	58535.71	2	14
WISEA J083019.97-632305.4	65975040	127.58288593	-63.38381226	39	19	58344.67	1	56
WISEA J084329.01+694709.8	70081792	130.86936209	69.78535795	23	29	58677.45	2	12
WISEA J101804.20-684254.0	65975552	154.51383115	-68.71398807	29	31	58326.78	1	122
WISEA J104051.77+450329.3	68143104	160.21595657	45.05803453	59	42	58549.01	3	8
WISEA J104216.89-003935.9	65975808	160.56943665	-0.66075227	78	19	58594.34	6	5
WISEA J105349.41-460241.2	65976064	163.45380404	-46.04390952	39	29	58410.09	1	60
WISEA J105917.38+285729.3	70083840	164.82071899	28.95865465	54	32	58748.00	9	6
WISEA J110201.76+350335.4	65976320	165.50723334	35.05947583	17	10	58598.99	3	6
WISEA J112440.19+663052.0	70016512	171.16746754	66.51400232	19	11	58677.37	1	10
WISEA J114350.90+401333.9	65977344	175.96029298	40.22521825	16	14	58565.07	3	6
WISEA J114601.22+342458.8	65977600	176.50372177	34.41670535	43	32	58598.97	3	7
WISEA J115917.89+671704.2	65977856	179.81987122	67.28374931	51	26	58535.45	1	10
WISEA J125721.01+715349.3	65978112	194.33121922	71.89699166	29	29	58342.73	2	12
WISEA J131102.03+312107.9	70085120	197.75827665	31.35224597	18	21	58787.83	3	6
WISEA J135042.33-830202.8	70084864	207.69524015	-83.03520175	41	41	58677.76	1	44
CWISEP J135937.65-435226.9	70079232	209.90620896	-43.87450576	23	27	58794.15	1	55
WISEA J143422.31-083934.2	65978368	218.59410001	-8.66004739	23	25	58419.48	1	11
WISEA J151620.39+721745.4	65978624	229.08171391	72.29750529	24	33	58525.48	1	16
WISEA J152529.09+605356.5	65978880	231.36949783	60.90077689	23	16	58412.23	1	10
WISEAR J154025.77-113940.8	68143360	235.10551308	-11.66231946	23	22	58431.55	1	31
WISEA J155349.96+693355.2	65979136	238.44587574	69.56790675	22	30	58358.98	1	13
WISEA J160516.79+002139.0	65979392	241.31920501	0.36045853	27	24	58435.17	1	15
WISEA J161940.51+134752.0	70019328	244.91893625	13.79777587	18	20	58683.34	1	12

Table 5
(Continued)

Name	AOR	R.A. (deg, ICRS)	Decl. (deg, ICRS)	$\sigma_{\text{R.A.}}$ (mas)	$\sigma_{\text{Decl.}}$ (mas)	MJD	Method Number ^a	N_{catib}
WISEA J162716.41–244355.4	70019584	246.81842257	–24.73230094	31	14	58681.61	9	4
WISEA J162852.64+160421.0	65980160	247.21956184	16.07014592	17	27	58323.79	1	14
WISEA J163932.75+184049.4	65980416	249.88517019	18.68033997	21	20	58324.27	1	21
WISEA J165902.66+274747.9	70081536	254.76088341	27.79695337	33	32	58677.16	1	11
WISEA J171331.68+245000.9	65980672	258.38136764	24.83425966	20	29	58324.56	1	23
WISEA J172907.10–753017.0	70080256	262.28008923	–75.50523721	39	20	58677.55	1	54
WISEA J175328.55–590447.6	68144640	268.36809140	–59.08058293	23	21	58469.25	1	86
WISEA J175701.50+183215.2	68141312	269.25658811	18.53743224	24	19	58457.88	1	38
WISEA J181849.59–470146.9	65980928	274.70680026	–47.03089410	23	21	58471.57	1	117
WISEA J185109.93+671343.7	65981184	282.79034267	67.22875209	62	30	58325.08	1	30
WISEA J190005.76–310810.9	65981440	285.02396090	–31.13711842	22	16	58484.17	1	137
WISEA J193054.55–205949.4	65981696	292.72484856	–20.99948094	21	30	58356.43	1	67
WISEA J201833.67–141720.3	65981952	304.64040610	–14.28865037	20	19	58508.47	1	43
WISEA J205921.85+662725.2	65982208	314.83817793	66.45691651	33	41	58404.81	1	43
WISEA J211456.86–180519.0	65982464	318.73577161	–18.08979809	13	13	58528.10	1	13
WISEA J212020.71+303656.2	70081280	320.08640707	30.61562843	16	21	58766.26	1	67
WISEA J212510.91–730758.8	65982720	321.29817399	–73.13397549	31	31	58344.65	1	16
WISEA J213810.99+373312.9	70081024	324.54582525	37.55373364	24	28	58766.25	1	69
WISEA J214025.23–332707.4	70080768	325.10661695	–33.45339899	23	25	58735.46	1	16
WISEA J215018.46–752053.0	68140800	327.58089437	–75.34866889	40	17	58459.16	1	15
WISEAR J220746.67–503631.7	68141056	331.94492853	–50.61225168	26	26	58509.50	2	14
WISEA J221859.33+114644.4	65983232	334.74775599	11.77832823	11	19	58407.08	1	14
WISEA J221841.38+143003.4	70082304	334.67136398	14.50036772	13	29	58766.28	1	17
WISEA J224319.56–145857.3	65984000	340.83216229	–14.98390871	30	20	58411.46	2	12
WISEU J224547.11–433341.5	68142336	341.44819598	–43.56205682	27	26	58523.84	1	11
WISEA J225404.16–265257.5	65984512	343.51885430	–26.88270278	23	44	58410.00	3	10
WISEA J230930.58+145633.1	65984768	347.37899411	14.94148799	41	34	58412.32	2	11
WISEA J233816.47–732929.7	65985024	354.57437439	–73.49193575	19	21	58412.39	1	11
WISEA J235120.62–700025.8	70083328	357.83542855	–70.00743644	25	43	58711.33	1	10
WISEA J235456.63–481440.1	65985536	358.73728759	–48.24501823	40	40	58412.36	1	11

Notes. N_{catib} is the number of Gaia DR2 sources used for Spitzer ch2 astrometric recalibration. See Section 8.4.1 of Meisner et al. (2020) for additional details.

^a The astrometric calibrator selection “method number” here refers to the method number listed in Table 6 of Meisner et al. (2020).

(This table is available in machine-readable form.)

10. Near-infrared Photometry

10.1. Mont-Mégantic/CPAPIR Follow-up

We observed 42 of our brown dwarf candidates in the MKO *J* band with the Caméra PANoramique Proche Infra-Rouge (CPAPIR; Artigau et al. 2004) wide-field ($30' \times 30'$) NIR camera located at the Observatoire du Mont-Mégantic (OMM) 1.6 m observatory (Racine 1978) between 2018 May and 2020 January. Ten of these OMM targets were well detected ($>4\sigma$), 11 were marginally detected ($<4\sigma$), and 21 were not detected.

Targets were always observed near the center of the lower right quadrant of the CPAPIR camera because the amplifier of the upper right quadrant is malfunctioning. The data were reduced with a custom Python pipeline that was standardized for CPAPIR/OMM data. Images are flat-fielded with a standard white field inside the telescope dome observed at the start or end of the night. A sky image is built from a median of the observations, taken across small, random dithering patterns and where all sources at the 2MASS positions are masked. The sky image is subtracted from each individual frame, and a linear astrometric solution is obtained with a local implementation of the <http://astrometry.net> tool (Lang et al. 2010) anchored on index files built from Gaia DR2 data (Gaia Collaboration et al. 2018; Lindegren et al. 2018). Individual images are then median combined into a final frame, and a new

astrometric solution is built from <http://astrometry.net> and Gaia DR2 including second-degree distortions as Simple Imaging Polynomial polynomials.

Aperture photometry was calculated for each target with a custom IDL pipeline using an aperture twice as large as the FWHM reported by the OMM data reduction pipeline ($1''7\text{--}4''9$ with a median of $2''1$), centered at the position predicted from the WISE+Spitzer motion solutions. Using twice the FWHM ensures that small deviations in predicted versus observed positions do not affect the photometric measurement, without needing to estimate a new centroid for very faint targets. The background sky was estimated from the median of an annulus with inner and outer radii 3 and 6 times as large as the photometric aperture, respectively.

Photometric zero-points were estimated by measuring the flux of all 2MASS catalog entries within the field of view (while avoiding the outermost 250 pixel edges) and calculating the median zero-point that translates from CPAPIR *J*-band fluxes to 2MASS *J*-band magnitudes. Limiting 5σ depths were calculated for nondetections by sampling 1000 uniform-random positions in the field of view while avoiding 2MASS entries. The average of the absolute flux values at 84th and 16th percentiles of the random distribution multiplied by 5 was then transformed to a 5σ detection limit in magnitudes with the

Table 6
Linear Motion Fit Results Combining WISE and Spitzer Astrometry

Name	α_0 (deg, ICRS)	δ_0 (deg, ICRS)	σ_{α_0} (mas)	σ_{δ_0} (mas)	MJD ₀	μ_α (mas yr ⁻¹)	μ_δ (mas yr ⁻¹)	μ_{tot} (mas yr ⁻¹)	χ^2_{motion}	χ^2	dof	χ^2_ν
CWISE J000229.93+635217.0	0.6225026	63.8712344	70	71	55379.85	802 ± 49	44 ± 47	803 ± 49	268.7	2.53	2	1.26
WISEA J001449.96+795116.1	3.7149072	79.8544230	40	37	58416.60	487 ± 44	-9 ± 41	487 ± 44	123.1	5.15	10	0.52
WISEU J001908.31-094323.3	4.7847093	-9.7234432	28	37	58778.24	-126 ± 58	-286 ± 59	312 ± 59	28.5	4.04	2	2.02
WISEA J002810.59+521853.1	7.0442758	52.3138656	33	33	58383.44	49 ± 34	-458 ± 34	461 ± 34	181.9	6.43	2	3.22
WISEA J002909.90+190516.6	7.2911017	19.0873034	27	19	58391.51	-80 ± 39	-296 ± 40	306 ± 40	59.4	0.90	2	0.45
WISEA J003631.29-642735.6	9.1313102	-64.4600379	20	26	58715.36	143 ± 38	-22 ± 37	144 ± 38	14.6	0.78	2	0.39
WISEU J004851.21+250814.9	12.2145993	25.1366132	20	20	58367.15	1009 ± 21	-728 ± 21	1244 ± 21	3446.9	8.49	10	0.85
WISEU J005559.88+594745.0	14.0004779	59.7957828	23	27	58375.91	408 ± 25	-24 ± 25	409 ± 25	275.5	12.59	10	1.26
WISEA J010116.12-520629.8	15.3196862	-52.1077423	37	21	58392.14	673 ± 45	236 ± 44	713 ± 45	253.9	7.94	10	0.79
WISEA J012057.06-764216.4	20.2389720	-76.7039955	43	22	58313.86	139 ± 43	271 ± 40	305 ± 41	56.7	0.17	2	0.08
WISEA J012834.87-280302.5	22.1459505	-28.0503342	22	18	58793.11	211 ± 37	138 ± 37	252 ± 37	46.2	0.52	2	0.26
WISEA J013217.78-581825.9	23.0759047	-58.3072568	21	26	58393.05	438 ± 43	-43 ± 41	440 ± 43	106.4	6.11	10	0.61
WISEU J013522.46-221957.3	23.8440303	-22.3331396	24	20	58798.63	199 ± 42	-317 ± 43	374 ± 43	77.2	0.93	2	0.47
WISEA J013810.78-412220.2	24.5467497	-41.3715961	33	33	58386.43	554 ± 82	348 ± 83	655 ± 82	63.3	2.24	2	1.12
WISEA J014603.23-261908.7	26.5147183	-26.3200316	26	32	58397.66	465 ± 58	-418 ± 59	625 ± 58	114.9	0.49	2	0.25
WISEA J015507.35-421635.7	28.7823850	-42.2767135	23	35	58805.52	486 ± 55	-88 ± 55	494 ± 55	81.4	0.21	2	0.11
WISEA J015601.22+525304.4	29.0049998	52.8845881	34	23	58769.24	2 ± 27	-12 ± 27	12 ± 27	0.2	5.08	2	2.54
WISEA J021420.18-573245.1	33.5864956	-57.5459455	23	21	58403.07	529 ± 55	-36 ± 53	530 ± 55	93.7	0.75	2	0.37
WISEA J025756.40-265528.8	44.4866123	-26.9245623	26	24	58424.03	541 ± 57	93 ± 58	549 ± 57	93.5	0.54	2	0.27
WISEA J025805.29-321917.4	44.5223944	-32.3218519	12	24	58775.48	183 ± 19	-115 ± 19	216 ± 19	127.4	5.51	2	2.76
WISEA J030534.09-582635.5	46.3904512	-58.4436436	28	42	58329.36	-363 ± 30	-185 ± 29	407 ± 30	185.0	10.79	12	0.90
WISEA J032600.28+421056.8	51.5021296	42.1833222	20	21	58451.49	228 ± 38	410 ± 39	469 ± 39	147.3	3.34	2	1.67
WISEA J032811.00-422321.6	52.0471675	-42.3882280	41	32	58392.89	407 ± 50	435 ± 50	595 ± 50	140.3	0.07	2	0.03
WISEA J034253.20+673143.5	55.7222242	67.5286251	23	31	58803.22	80 ± 29	-18 ± 30	82 ± 29	8.1	3.05	2	1.52
WISEA J034227.44-462252.0	55.6153003	-46.3806890	28	27	58769.74	250 ± 40	154 ± 41	294 ± 40	52.9	0.50	2	0.25
WISEA J035410.03-572104.0	58.5417751	-57.3515241	22	26	58750.33	10 ± 43	-170 ± 42	171 ± 42	16.7	1.97	2	0.98
WISEA J035733.85+070557.4	59.3917084	7.0983951	18	30	58452.48	275 ± 39	-361 ± 41	454 ± 41	125.5	4.45	10	0.44
WISEA J040702.42+190945.8	61.7607504	19.1622810	28	20	58458.11	289 ± 49	-178 ± 51	340 ± 49	47.8	0.95	2	0.48
WISEA J042236.95-044203.5	65.6566997	-4.7026620	27	29	58454.14	1150 ± 53	-695 ± 55	1344 ± 54	625.6	2.58	4	0.64
WISEA J050238.28+100750.0	75.6591290	10.1299861	16	17	58492.12	-177 ± 36	-223 ± 38	284 ± 38	57.1	1.92	2	0.96
WISEU J050305.68-564834.0	75.7772405	-56.8085133	27	24	58367.04	801 ± 28	322 ± 28	864 ± 28	953.4	16.91	10	1.69
WISEA J050615.56-514521.3	76.5641167	-51.7564942	24	24	58659.17	-127 ± 36	-239 ± 37	271 ± 37	53.4	0.12	2	0.06
WISEA J053535.43-644518.5	83.8970611	-64.7545225	34	20	58370.15	-116 ± 11	260 ± 10	284 ± 10	773.0	0.85	2	0.42
WISEA J053512.01-773829.7	83.8003381	-77.6410178	26	27	58374.70	13 ± 30	251 ± 32	251 ± 32	59.9	3.15	2	1.58
WISEA J061713.07+670400.8	94.3037035	67.0668897	44	22	58655.33	-113 ± 40	24 ± 43	116 ± 40	8.2	4.56	2	2.28
WISEA J064503.72+524054.1	101.2641238	52.6796522	20	26	58450.69	-314 ± 21	-945 ± 23	996 ± 23	1887.8	9.48	10	0.95
WISEA J065113.90-835502.6	102.8036976	-83.9168458	23	25	58631.78	-175 ± 26	230 ± 27	290 ± 27	118.4	0.47	2	0.24
WISEA J075438.20+090044.9	118.6597088	9.0118237	25	29	58528.49	166 ± 52	-280 ± 55	326 ± 54	36.4	2.18	2	1.09
WISEA J080622.22-082046.5	121.5931954	-8.3496258	24	18	58516.33	296 ± 34	-1366 ± 36	1398 ± 36	1512.3	9.87	10	0.99
WISEA J083011.95+283716.0	127.5494547	28.6163163	25	33	58523.11	-189 ± 58	-2053 ± 62	2062 ± 62	1120.6	4.38	10	0.44
WISEA J083019.97-632305.4	127.5828973	-63.3838313	39	19	58297.09	-83 ± 28	501 ± 28	508 ± 28	334.0	10.09	10	1.01
WISEA J084329.01+694709.8	130.8693699	69.7853611	23	29	58662.96	-234 ± 50	-278 ± 53	363 ± 52	49.0	0.25	2	0.12

Table 6
(Continued)

Name	α_0 (deg, ICRS)	δ_0 (deg, ICRS)	σ_{α_0} (mas)	σ_{δ_0} (mas)	MJD ₀	μ_{α} (mas yr ⁻¹)	μ_{δ} (mas yr ⁻¹)	μ_{tot} (mas yr ⁻¹)	χ^2_{motion}	χ^2	dof	χ^2_{ν}
WISEA J101804.20−684254.0	154.5139496	−68.7140252	28	30	58239.38	−608 ± 26	536 ± 26	810 ± 26	1002.9	10.97	10	1.10
WISEA J104051.77+450329.3	160.2159462	45.0580445	56	42	58406.68	62 ± 31	−73 ± 31	96 ± 31	9.5	1.57	2	0.79
WISEA J104216.89−003935.9	160.5694386	−0.6607485	77	19	58579.15	−361 ± 51	−342 ± 53	497 ± 52	92.2	1.08	2	0.54
WISEA J105349.41−460241.2	163.4538550	−46.0439285	38	29	58340.00	−664 ± 31	370 ± 32	761 ± 31	606.4	2.54	6	0.42
WISEA J105917.38+285729.3	164.8207434	28.9586486	53	33	58703.56	−592 ± 46	191 ± 47	622 ± 46	185.1	1.09	2	0.55
WISEA J110201.76+350335.4	165.5072344	35.0594772	17	11	58587.00	−66 ± 29	−159 ± 30	172 ± 30	33.8	5.89	10	0.59
WISEA J112440.19+663052.0	171.1674677	66.5140041	19	12	58662.24	10 ± 27	−152 ± 28	152 ± 28	29.0	0.34	2	0.17
WISEA J114350.90+401333.9	175.9602973	40.2252208	16	15	58556.32	−492 ± 41	−384 ± 43	624 ± 41	228.5	10.12	10	1.01
WISEA J114601.22+342458.8	176.5037433	34.4166991	43	32	58547.09	−470 ± 39	128 ± 41	487 ± 39	156.3	9.26	10	0.93
WISEA J115917.89+671704.2	179.8199024	67.2837552	50	27	58513.81	−774 ± 59	−338 ± 60	845 ± 60	201.3	5.01	10	0.50
WISEA J125721.01+715349.3	194.3312702	71.8969922	29	29	58322.64	−952 ± 54	−25 ± 53	952 ± 54	310.3	5.17	2	2.58
WISEA J131102.03+312107.9	197.7582770	31.3522460	18	22	58773.53	−42 ± 38	10 ± 40	44 ± 38	1.3	1.31	2	0.66
WISEA J135042.33−830202.8	207.6951222	−83.0351927	42	41	58658.13	909 ± 63	−533 ± 62	1054 ± 62	284.4	10.52	2	5.26
CWISEP J135937.65−435226.9	209.9062116	−43.8745052	23	27	58784.91	−303 ± 65	−141 ± 68	334 ± 65	26.0	3.91	2	1.96
WISEA J143422.31−083934.2	218.5940972	−8.6600460	23	25	58412.23	503 ± 69	−236 ± 73	555 ± 70	63.2	0.24	2	0.12
WISEA J151620.39+721745.4	229.0817502	72.2974880	24	33	58490.15	−429 ± 37	654 ± 35	782 ± 36	474.8	3.65	10	0.36
WISEA J152529.09+605356.5	231.3695088	60.9007668	23	17	58395.04	−365 ± 38	770 ± 37	852 ± 37	516.8	4.70	10	0.47
WISEAR J154025.77−113940.8	235.1055164	−11.6623176	23	23	58426.07	−777 ± 74	−409 ± 77	878 ± 75	138.1	0.59	2	0.30
WISEA J155349.96+693355.2	238.4459734	69.5678794	22	30	58332.37	−1684 ± 56	1348 ± 53	2157 ± 55	1549.3	5.05	8	0.63
WISEA J160516.79+002139.0	241.3192107	0.3604616	27	24	58409.22	−295 ± 38	−157 ± 40	334 ± 38	76.4	0.04	2	0.02
WISEA J161940.51+134752.0	244.9189341	13.7977748	18	20	58614.57	45 ± 16	8 ± 17	45 ± 16	7.7	2.17	2	1.08
WISEA J162716.41−244355.4	246.8184113	−24.7322913	29	14	58575.18	39 ± 15	−105 ± 14	112 ± 14	65.1	25.16	10	2.52
WISEA J162852.64+160421.0	247.2195602	16.0701545	18	28	58313.18	154 ± 49	−1047 ± 53	1059 ± 53	401.8	11.69	10	1.17
WISEA J163932.75+184049.4	249.8851790	18.6803400	21	21	58303.49	−523 ± 35	28 ± 37	524 ± 35	222.1	4.25	10	0.42
WISEA J165902.66+274747.9	254.7608835	27.7969502	33	32	58653.69	−32 ± 53	149 ± 56	152 ± 56	7.4	2.09	2	1.04
WISEA J171331.68+245000.9	258.3813705	24.8342589	21	29	58314.64	−304 ± 61	214 ± 65	372 ± 63	35.2	4.14	2	2.07
WISEA J172907.10−753017.0	262.2800827	−75.5052306	39	21	58628.40	46 ± 27	−181 ± 28	187 ± 28	44.0	0.26	2	0.13
WISEA J175328.55−590447.6	268.3680988	−59.0805770	24	21	58445.32	−197 ± 35	−328 ± 36	382 ± 36	112.8	4.02	10	0.40
WISEA J175701.50+183215.2	269.2565871	18.5374332	25	19	58443.86	114 ± 44	−81 ± 47	140 ± 45	9.6	0.58	2	0.29
WISEA J181849.59−470146.9	274.7067977	−47.0308803	23	22	58433.15	29 ± 28	−517 ± 29	518 ± 29	311.5	10.01	2	5.01
WISEA J185109.93+671343.7	282.7903397	67.2287532	61	30	58301.83	52 ± 74	−97 ± 70	110 ± 71	2.4	1.55	2	0.77
WISEA J190005.76−310810.9	285.0239614	−31.1371133	22	16	58460.85	−26 ± 28	−301 ± 30	303 ± 30	101.0	0.82	2	0.41
WISEA J193054.55−205949.4	292.7248684	−20.9994605	21	30	58331.41	−994 ± 36	−1098 ± 38	1481 ± 38	1561.2	4.71	10	0.47
WISEA J201833.67−141720.3	304.6404052	−14.2886541	21	20	58482.80	48 ± 32	191 ± 33	197 ± 33	35.4	0.07	2	0.04
WISEA J205921.85+662725.2	314.8382734	66.4569167	32	40	58303.22	−511 ± 28	−31 ± 27	512 ± 28	326.5	3.95	2	1.98
WISEA J211456.86−180519.0	318.7357753	−18.0897946	13	14	58518.15	−460 ± 35	−473 ± 36	660 ± 35	349.8	2.77	10	0.28
WISEA J212020.71+303656.2	320.0864070	30.6156283	16	21	58747.66	6 ± 33	10 ± 33	12 ± 33	0.1	0.01	2	0.00
WISEA J212510.91−730758.8	321.2981397	−73.1339610	31	31	58306.39	325 ± 41	−464 ± 41	567 ± 41	189.7	1.60	2	0.80
WISEA J213810.99+373312.9	324.5458272	37.5537319	24	28	58731.84	−21 ± 32	75 ± 32	78 ± 32	6.0	7.26	2	3.63
WISEA J214025.23−332707.4	325.1066145	−33.4533963	23	25	58728.28	415 ± 67	−515 ± 69	661 ± 69	93.2	2.10	2	1.05
WISEU J215018.46−752053.0	327.5808368	−75.3486640	40	18	58438.92	918 ± 40	−307 ± 40	968 ± 40	571.9	5.80	10	0.58
WISEAR J220746.67−503631.7	331.9449276	−50.6122455	27	26	58503.19	108 ± 99	−1380 ± 98	1384 ± 98	198.1	4.40	10	0.44

Table 6
(Continued)

Name	α_0 (deg, ICRS)	δ_0 (deg, ICRS)	σ_{α_0} (mas)	σ_{δ_0} (mas)	MJD ₀	μ_α (mas yr ⁻¹)	μ_δ (mas yr ⁻¹)	μ_{tot} (mas yr ⁻¹)	χ^2_{motion}	χ^2	dof	χ^2_ν
WISEA J221859.33+114644.4	334.7477539	11.7783302	11	20	58394.99	224 ± 31	-267 ± 33	349 ± 32	118.0	1.33	2	0.67
WISEA J221841.38+143003.4	334.6713695	14.5003718	14	29	58748.87	-387 ± 33	-307 ± 34	494 ± 33	218.4	3.67	10	0.37
WISEA J224319.56-145857.3	340.8321592	-14.9839027	30	21	58396.41	286 ± 49	-541 ± 50	611 ± 50	150.2	0.51	2	0.25
WISEU J224547.11-433341.5	341.4481561	-43.5620463	27	26	58490.27	1108 ± 35	-388 ± 35	1174 ± 35	1131.1	2.73	2	1.37
WISEA J225404.16-265257.5	343.5188443	-26.8827008	24	43	58389.63	566 ± 54	-63 ± 54	569 ± 54	113.0	0.96	2	0.48
WISEA J230930.58+145633.1	347.3789785	14.9414978	41	34	58383.22	664 ± 59	-466 ± 60	811 ± 59	187.3	3.79	12	0.32
WISEA J233816.47-732929.7	354.5743186	-73.4919335	19	22	58385.05	755 ± 32	-114 ± 30	764 ± 31	588.8	3.71	10	0.37
WISEA J235120.62-700025.8	357.8354396	-70.0074316	25	43	58665.89	-101 ± 37	-139 ± 36	172 ± 36	22.3	0.42	2	0.21
WISEA J235456.63-481440.1	358.7372720	-48.2450119	40	40	58373.02	403 ± 50	-231 ± 50	465 ± 50	85.7	3.21	2	1.60

Note. $\chi^2_\nu = \chi^2/(\text{dof})$.

(This table is available in machine-readable form.)

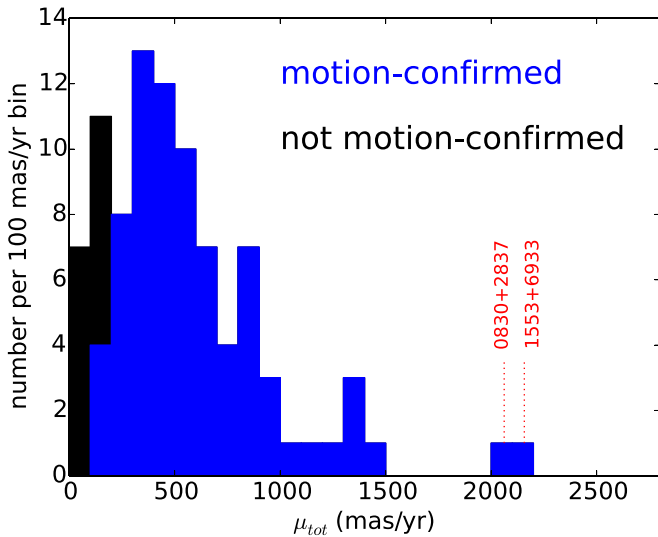


Figure 4. Distribution of best-fit total linear motions for our brown dwarf candidates. The number of sample members per bin that were not motion confirmed is shown in black, stacked on top of the number of motion-confirmed targets per bin (blue). Objects with $\mu_{\text{tot}} \gtrsim 170 \text{ mas yr}^{-1}$, corresponding to approximately half of a WISE pixel of displacement over the available time baseline, tend to be motion confirmed. One new discovery (WISEA 1553+6933) has best-fit $\mu_{\text{tot}} > 2000 \text{ mas yr}^{-1}$, and eight have $\mu_{\text{tot}} > 1000 \text{ mas yr}^{-1}$; these number counts do not include WISEA 0830+2837 ($\mu_{\text{tot}} \approx 2060 \text{ mas yr}^{-1}$), since this object’s discovery was previously presented in Bardalez Gagliuffi et al. (2020).

appropriate zero-point. The 5σ depths ranged from 15.7 to 19.2 mag, with a median value of 18.1 mag.

10.2. Archival Near-infrared Photometry

We have also compiled archival NIR photometry for members of our sample using the WFCAM Science Archive (UKIRT/WFCAM data; Hambly et al. 2008) and VISTA Science Archive (VISTA/VIRCAM data; Cross et al. 2012). We issued a cone search in the vicinity of each target and visually vetted possible NIR counterparts to avoid spurious positional cross-matches. We searched for archival NIR photometry in the Y , J , H , and K bands (K_S rather than K in the case of VIRCAM). The NIR counterparts are predominantly drawn from the UKIRT Hemisphere Survey in the north (UHS; Dye et al. 2018) and the VISTA Hemisphere Survey in the south (VHS; McMahon et al. 2013), though VIKING (Edge et al. 2013) and the UKIRT Infrared Deep Sky Survey (Lawrence et al. 2007) also contribute. By selection, all members of our sample lack 2MASS (Skrutskie et al. 2006) counterparts.

10.3. Merged Near-infrared Photometry

Table 7 provides a merged compilation of OMM and archival NIR photometry for motion-confirmed targets, in the $YJHK/K_S$ bands. In cases where both OMM and archival follow-up J -band photometry are available, Table 7 quotes the higher significance measurement. Table 8 reports additional OMM follow-up results for targets that are not motion confirmed and/or have higher-significance J -band measurements in archival data sets. Our follow-up OMM photometry agrees well with archival photometry in cases where both are available.

Figure 5 shows a color-color plot of J -ch2 versus ch1-ch2 for motion-confirmed targets with both colors available. The

data points are by and large in good agreement with the expected trend for brown dwarfs (Dupuy & Liu 2012), providing further assurance that our motion confirmation process has weeded out static contaminants that might display rather discrepant colors. WISEAR 2207-5036, a suspected subdwarf owing to its high kinematics (Section 11.5.1), stands out as likely the strongest color outlier. Even if all other sample members are typical field brown dwarfs, we would statistically expect some fraction to scatter $>1\sigma$ off of the Dupuy & Liu (2012) locus; this likely explains most or all of the Figure 5 J -band detections falling modestly outside of the purple shaded region. Analogous color-color diagrams for Y -ch2, H -ch2, and K -ch2 again show agreement with the expected trends for brown dwarfs, though we have omitted those plots owing to their paucity of NIR detections.

In addition to the ground-based NIR photometry gathered here, five of our targets have HST follow-up NIR photometry (Bardalez Gagliuffi et al. 2020). Owing to the nonstandard bandpasses of these HST data, we have chosen not to merge the HST measurements with our ground-based photometry in this work.

11. Results and Discussion

11.1. Derived Parameters

Table 9 lists various properties that we are able to derive based on our ch1 and ch2 magnitudes, for the sample of motion-confirmed objects with both of these Spitzer photometric data points available.²³ These derived parameters are as follows:

1. Phototype: We estimate phototypes using the Kirkpatrick et al. (2019) relation for spectral type as a function of ch1-ch2 color. We use the same phototyping procedure as Meisner et al. (2020), which contains a more detailed explanation of our methodology and associated caveats. In brief, Meisner et al. (2020) estimate an rms phototyping uncertainty of approximately ± 1 subtype. Larger errors between phototype and real spectral type for individual objects are of course possible, and photometric type estimates should never be considered substitutes for true spectral types. For the four objects successfully assigned a true spectral type and subtype in Table 3, our phototypes achieve the expected level of agreement: an rms difference of 1.03 subtypes.
2. Absolute ch2 magnitude: We estimate the absolute ch2 magnitude using the Kirkpatrick et al. (2019) relation for M_{ch2} as a function of ch1-ch2. Again, our procedure is the same as that of Meisner et al. (2020), which contains further details, particularly in relation to the quoted uncertainties.
3. Distance: Photometric distance estimates for members of our sample follow from the combination of each object’s measured apparent ch2 magnitude and M_{ch2} estimate. Details of how we quote these distances and their associated uncertainties can be found in Meisner et al. (2020).
4. Effective temperature: We provide T_{eff} estimates based on the Kirkpatrick et al. (2019) relation for effective

²³ WISEA 0535-6445 is excluded from Table 9 despite having a Spitzer color measurement, since its ch1-ch2 ≈ 0 color does not place a strong constraint on its spectral type or absolute magnitude. See Section 11.7.2 for further discussion of this object.

Table 7
Ground-based NIR Photometry from the VISTA/UKIRT Archives and OMM Follow-up for Motion-confirmed Members of Our Sample

Name	Y (mag)	J_{MKO} (mag)	H_{MKO} (mag)	K_{MKO} (mag)	K_S (mag)	Origin
WISEA J001449.96+795116.1	...	19.72 ± 0.62	CPAPIR
WISEU J001908.31-094323.3	19.72 ± 0.10	18.80 ± 0.08	>18.13	VIRCAM
WISEA J002810.59+521853.1	...	19.20 ± 0.16	WFCAM
WISEA J002909.90+190516.6	...	17.81 ± 0.04	WFCAM
WISEU J004851.21+250814.9	...	19.51 ± 0.16	WFCAM
WISEU J005559.88+594745.0	...	17.90 ± 0.05	WFCAM
WISEA J010116.12-520629.8	...	19.76 ± 0.12	>18.31	VIRCAM
WISEA J012057.06-764216.4	20.14 ± 0.14	19.10 ± 0.10	>18.13	VIRCAM
WISEA J012834.87-280302.5	18.86 ± 0.02	17.73 ± 0.01	17.88 ± 0.03	...	17.96 ± 0.06	VIRCAM
WISEA J013217.78-581825.9	...	19.59 ± 0.10	>18.57	VIRCAM
WISEU J013522.46-221957.3	...	18.24 ± 0.03	18.58 ± 0.27	VIRCAM
WISEA J021420.18-573245.1	...	19.73 ± 0.18	>18.03	VIRCAM
WISEA J025805.29-321917.4	18.48 ± 0.02	17.72 ± 0.01	17.86 ± 0.05	...	17.38 ± 0.05	VIRCAM
WISEA J030534.09-582635.5	...	19.10 ± 0.06	>18.44	VIRCAM
WISEA J032600.28+421056.8	...	18.71 ± 0.12	WFCAM
WISEA J032811.00-422321.6	...	19.16 ± 0.09	VIRCAM
WISEA J034227.44-462252.0	...	18.73 ± 0.06	19.15 ± 0.19	...	>18.44	VIRCAM
WISEA J035733.85+070557.4	...	17.66 ± 0.05	WFCAM
WISEA J040702.42+190945.8	...	17.73 ± 0.04	...	18.20 ± 0.18	...	WFCAM
WISEA J042236.95-044203.5	>19.97	19.43 ± 0.23	>18.89	VIRCAM
WISEA J050238.28+100750.0	...	18.90 ± 0.11	WFCAM
WISEU J050305.68-564834.0	...	>20.29	>18.42	VIRCAM
WISEA J050615.56-514521.3	...	>20.05	>19.01	...	>18.30	VIRCAM
WISEA J053512.01-773829.7	>20.31	19.67 ± 0.20	>18.05	VIRCAM
WISEA J064503.72+524054.1	...	19.96 ± 0.22	WFCAM
WISEA J065113.90-835502.6	...	19.39 ± 0.19	>17.92	VIRCAM
WISEA J075438.20+090044.9	...	19.63 ± 0.21	WFCAM
WISEA J080622.22-082046.5	...	>19.60	>18.07	VIRCAM
WISEA J083011.95+283716.0	...	>18.57	CPAPIR
WISEA J083019.97-632305.4	...	18.64 ± 0.10	VIRCAM
WISEA J101804.20-684254.0	...	18.58 ± 0.09	>17.74	VIRCAM
WISEA J104216.89-003935.9	20.09 ± 0.07	19.18 ± 0.04	19.41 ± 0.11	VIRCAM
WISEA J105349.41-460241.2	...	18.64 ± 0.10	>17.86	VIRCAM
WISEA J105917.38+285729.3	...	18.61 ± 0.09	WFCAM
WISEA J110201.76+350335.4	...	19.12 ± 0.13	WFCAM
WISEA J112440.19+663052.0	...	18.48 ± 0.30	CPAPIR
WISEA J114350.90+401333.9	...	18.52 ± 0.07	WFCAM
WISEA J114601.22+342458.8	...	18.09 ± 0.04	WFCAM
WISEA J115917.89+671704.2	...	>18.40	CPAPIR
WISEA J125721.01+715349.3	...	>19.02	CPAPIR
WISEA J143422.31-083934.2	>20.04	>19.55	>19.51	...	>18.29	VIRCAM
WISEA J151620.39+721745.4	...	20.34 ± 0.66	CPAPIR
WISEA J152529.09+605356.5	...	>18.34	CPAPIR
WISEAR J154025.77-113940.8	20.28 ± 0.26	19.57 ± 0.20	>19.29	...	>18.79	VIRCAM
WISEA J155349.96+693355.2	...	>17.34	CPAPIR
WISEA J160516.79+002139.0	...	19.02 ± 0.12	WFCAM
WISEA J162852.64+160421.0	...	>19.50	WFCAM
WISEA J163932.75+184049.4	...	>19.47	WFCAM
WISEA J171331.68+245000.9	...	19.37 ± 0.16	WFCAM
WISEA J172907.10-753017.0	...	17.80 ± 0.04	18.18 ± 0.27	VIRCAM
WISEA J175328.55-590447.6	...	19.05 ± 0.09	>18.02	VIRCAM
WISEA J181849.59-470146.9	...	19.81 ± 0.22	>18.12	VIRCAM
WISEA J190005.76-310810.9	...	18.40 ± 0.06	>18.16	VIRCAM
WISEA J193054.55-205949.4	...	>19.80	>18.08	VIRCAM
WISEA J201833.67-141720.3	...	19.13 ± 0.00	>18.28	VIRCAM
WISEA J205921.85+662725.2	...	>16.07	CPAPIR
WISEA J211456.86-180519.0	19.46 ± 0.08	18.34 ± 0.06	>18.09	VIRCAM
WISEA J212510.91-730758.8	19.58 ± 0.16	18.76 ± 0.14	>17.79	VIRCAM
WISEA J214025.23-332707.4	>20.50	19.96 ± 0.26	>18.11	VIRCAM
WISEU J215018.46-752053.0	18.53 ± 0.13	18.10 ± 0.10	>17.40	VIRCAM
WISEAR J220746.67-503631.7	...	>20.36	>18.98	...	>18.38	VIRCAM
WISEA J221859.33+114644.4	...	17.94 ± 0.06	WFCAM
WISEA J221841.38+143003.4	...	19.14 ± 0.12	WFCAM

Table 7
(Continued)

Name	Y (mag)	J_{MKO} (mag)	H_{MKO} (mag)	K_{MKO} (mag)	K_S (mag)	Origin
WISEA J224319.56–145857.3	>20.43	>19.91	>18.06	VIRCAM
WISEU J224547.11–433341.5	...	18.10 ± 0.03	18.53 ± 0.29	VIRCAM
WISEA J225404.16–265257.5	>20.10	>19.55	>17.98	VIRCAM
WISEA J230930.58+145633.1	...	17.75 ± 0.04	WFCAM
WISEA J233816.47–732929.7	20.39 ± 0.18	19.30 ± 0.13	>18.03	VIRCAM
WISEA J235456.63–481440.1	...	>20.11	>19.33	...	>18.61	VIRCAM

Note. Magnitude limits are 5σ .

(This table is available in machine-readable form.)

Table 8
Additional OMM J -band Photometry

Designation	J_{MKO} (mag)
WISEA J002810.59+521853.1	19.58 ± 0.58
WISEA J002909.90+190516.6	18.02 ± 0.17
WISEU J005559.88+594745.0	16.52 ± 0.05^a
WISEA J032600.28+421056.8	18.85 ± 0.28
WISEA J035733.85+070557.4	17.51 ± 0.08
WISEA J040702.42+190945.8	17.61 ± 0.08
WISEA J042236.95–044203.5	19.62 ± 0.39
WISEA J050238.28+100750.0	>16.84
WISEA J064503.72+524054.1	19.82 ± 0.68
WISEA J075438.20+090044.9	>17.95
WISEA J080622.22–082046.5	>16.64
WISEA J104051.77+450329.3	18.04 ± 0.08
WISEA J104216.89–003935.9	19.47 ± 0.40
WISEA J105917.38+285729.3	18.39 ± 0.28
WISEA J110201.76+350335.4	19.56 ± 0.82
WISEA J114350.90+401333.9	18.82 ± 0.27
WISEA J114601.22+342458.8	18.29 ± 0.10
WISEA J143422.31–083934.2	>18.12
WISEAR J154025.77–113940.8	>18.08
WISEA J161940.51+134752.0	>18.07
WISEA J162716.41–244355.4	>15.73
WISEA J162852.64+160421.0	>18.32
WISEA J163932.75+184049.4	>18.28
WISEA J171331.68+245000.9	19.36 ± 0.25
WISEA J175701.50+183215.2	>17.39
WISEA J185109.93+671343.7	>18.79
WISEA J193054.55–205949.4	>17.01
WISEA J201833.67–141720.3	19.45 ± 0.66
WISEA J211456.86–180519.0	18.45 ± 0.27
WISEA J213810.99+373312.9	>16.01
WISEA J221841.38+143003.4	>17.78
WISEA J224319.56–145857.3	>17.83
WISEA J230930.58+145633.1	17.80 ± 0.12

Notes. This table reports follow-up J band photometry for targets not motion confirmed and/or with higher-significance J -band measurements from archival data sets. Magnitude limits are 5σ .

^a The OMM photometry for WISEU 0055+5947 is contaminated by blending with a brighter nearby source, resulting in a reported magnitude that is artificially bright.

(This table is available in machine-readable form.)

temperature as a function of $\text{ch1} - \text{ch2}$ color. No T_{eff} value is listed if $\text{ch1} - \text{ch2} < 0.9$, since the Kirkpatrick et al. (2019) $T_{\text{eff}}(\text{ch1} - \text{ch2})$ relation is not applicable in that Spitzer color regime.

5. Tangential velocity: V_{tan} estimates follow from the combination of our μ_{tot} values in Table 6 and our photometric distance estimates. As shown in Figure 6, our set of targets appears to have a higher typical V_{tan} value than that found for the Kirkpatrick et al. (2019) volume-limited sample of mid- to late T and Y dwarfs within 20 pc. The 180 Kirkpatrick et al. (2019) objects within 20 pc have a median V_{tan} of 35 km s^{-1} , whereas our sample's median V_{tan} is 60 km s^{-1} . This presumably owes to a bias whereby our motion-selected sample preferentially contains relatively faint and fast-moving targets.

Table 9 also includes ch2 reduced proper motions,²⁴ calculated by combining linear motion fitting results from Table 6 with the apparent ch2 magnitudes from Table 2. Figure 6 shows histograms of $\text{ch1} - \text{ch2}$ color, photometric distance, and V_{tan} for objects in Table 9. Further discussion subsections draw heavily on the Table 9 parameters to highlight notable aspects and members of our sample.

11.2. The 10 and 20 pc Samples

Studies of the substellar mass function are currently limited by incompleteness of the local ($\lesssim 20$ pc) brown dwarf sample at the latest spectral types (Kirkpatrick et al. 2019). A core objective of this work was therefore to help pinpoint previously unidentified members of the 20 pc census.

In terms of our nearest motion-confirmed discoveries, two have best-fit photometric distance estimates (Table 9) within 10 pc: WISEA 0830+2837 and WISEA 1930–2059. WISEA 1930–2059 also has a 1σ distance upper envelope value within 10 pc. For WISEA 0830+2837, Bardalez Gagliuffi et al. (2020) have published a WISE+Spitzer trigonometric parallax of 90.6 ± 13.7 mas, placing this object most likely outside of the 10 pc sample, though still possibly closer than 10 pc within the 1σ parallax uncertainty. WISEU 0503–5648 has a central distance estimate larger than 10 pc but could still be closer than 10 pc within its 1σ photometric distance estimate uncertainty.

Sixteen of our motion-confirmed discoveries have central photometric distance estimates within 20 pc. An additional 15 of our motion-confirmed discoveries have central photometric distance estimates larger than 20 pc but still within 1σ of the 20 pc threshold. Considering that the Kirkpatrick et al. (2019) 20 pc sample of late T and Y dwarfs consisted of 235 objects (46 of which have central parallax values placing them within 10

²⁴ Defined as $H_{\text{ch2}} = m_{\text{ch2}} + 5 \log_{10} \mu + 5$.

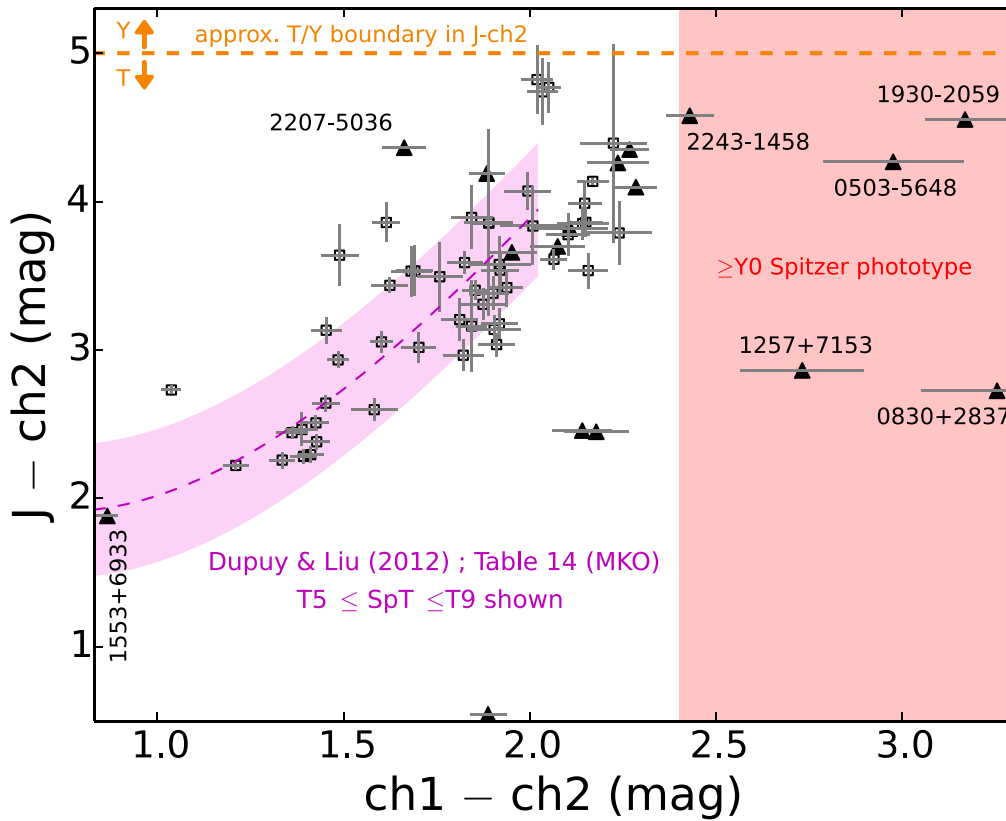


Figure 5. $J - ch2$ vs. $ch1 - ch2$ for motion-confirmed targets with both colors available. Follow-up J -band photometry comes from OMM/CPAPIR, and archival J -band photometry is obtained from the WFCAM/VISTA archives. Black squares represent detections. All $J - ch2$ lower limits (black triangles) are based on 5σ J limits. The dashed purple line shows the relation for mid- to late T dwarfs from Dupuy & Liu (2012), with the purple shaded region indicating the 1σ scatter in that relation. Our motion-confirmed sample generally follows the expected trend. The light-red shaded region denotes the Spitzer color range within which our phototyping procedure yields $\geq Y0$ estimates, $ch1 - ch2 \geq 2.4$ mag. The dashed orange horizontal line indicates the approximate boundary between late T and early Y dwarfs in terms of $J - ch2$ color. Our $J - ch2$ limit for WISEAR 2207–5036, a suspected subdwarf owing to its high kinematics, indicates that it is also a color outlier.

pc), our discoveries represent a sizable new batch of candidate 20 pc sample members.

11.3. Y Dwarf Candidates

Given our use of the Kirkpatrick et al. (2019) phototyping relation, we have effectively placed our threshold for Y dwarf candidacy at $ch1 - ch2 > 2.4$ mag. Five of our motion-confirmed brown dwarf candidates have best-fit Spitzer colors most consistent with $\geq Y0$ phototypes: WISEU 0503–5648, WISEA 0830+2837, WISEA 1257+7153, WISEA 1930–2059, and WISEA 2243–1458. WISEA 0830+2837 has already been discussed thoroughly in Bardalez Gagliuffi et al. (2020) and is thought to be of type $\geq Y1$. Of the other four motion-confirmed Y dwarf candidates first presented in this work, three have exceptionally red Spitzer colors most consistent with types $\geq Y1$. This new crop of $\geq Y1$ candidates discovered by Backyard Worlds is particularly significant given that only four to six spectroscopically confirmed brown dwarfs are currently known in this regime: WISE 0350–5658 (Y1; Kirkpatrick et al. 2012), WISE 0647–6232 (Y1; Kirkpatrick et al. 2012), WISE 1541–2250 (Y1; Cushing et al. 2011), WISE 2354–0240 (Y1; Schneider et al. 2015), WISE 1828+2650 ($\geq Y2$ with highly uncertain T_{eff} ; Beichman et al. 2013), and WISE 0855–0714 (L - and M -band spectra; Skemer et al. 2016; Morley et al. 2018). The impact of our sample’s likely

coldest four discoveries in terms of mass function analyses is also considerable: only nine previously known objects in the Kirkpatrick et al. (2019) 20 pc compilation inhabit the corresponding $T_{\text{eff}} < 400$ K effective temperature range.

Of our five motion-confirmed discoveries with phototypes $\geq Y0$, four are more than 2σ redder than our T/Y threshold color of $ch1 - ch2 = 2.4$ mag. On the other hand, WISEA 2243–1458 is within its 1σ color uncertainty of being classified as a late T dwarf. A sixth member of our sample (WISEA 2351–7000) would have a Y phototype based on its $ch1 - ch2$ color, but it falls just short of exceeding our χ^2_{motion} significance threshold (Table 6). Figure 7 shows WISE+Spitzer motion trajectories for all six targets with $ch1 - ch2 > 2.4$ mag, including WISEA 2351–7000. The WISEA 2351–7000 WISE+Spitzer astrometric trajectory looks plausibly linear, but more data will be needed to conclusively establish whether this source is moving.

Each of our five motion-confirmed Y dwarf candidates is labeled in Figure 5. Clearly, the existing J limits for these sources are not deep enough to confirm that their $J - ch2$ colors are securely in the $J - ch2 \gtrsim 5$ mag regime occupied by Y dwarfs. Therefore, deeper ground-based NIR imaging of our Y dwarf candidates would be of high value, with the exception of WISEA 0830+2837, which already has extreme $F125W - ch2 > 9.36$ mag and $F105W - ch2 > 9.56$ mag limits available (Bardalez Gagliuffi et al. 2020).

Table 9
Derived Parameters of Motion-confirmed Objects with Spitzer ch1 and ch2 Photometry

Name	SpT (phototype)	M_{ch2} (mag)	Distance (pc)	T_{eff} (K)	H_{ch2} (mag)	V_{tan} (km s ⁻¹)
CWISE J000229.93+635217.0	7.5	13.41 ^{+0.42} _{-0.39}	28.6 ^{+5.6} _{-5.1}	730 ⁺¹³² ₋₁₂₄	20.21 ^{+0.15} _{-0.14}	109 ⁺²² ₋₂₁
WISEA J001449.96+795116.1	8.0	13.68 ^{+0.31} _{-0.31}	27.4 ^{+4.2} _{-3.7}	643 ⁺⁸⁴ ₋₈₄	19.30 ^{+0.21} _{-0.19}	63 ⁺¹¹ ₋₁₀
WISEU J001908.31-094323.3	7.0	13.20 ^{+0.30} _{-0.30}	31.1 ^{+4.6} _{-4.0}	815 ⁺⁸³ ₋₈₃	18.14 ^{+0.45} _{-0.37}	46 ⁺¹¹ ₋₁₀
WISEA J002810.59+521853.1	7.5	13.44 ^{+0.30} _{-0.30}	27.9 ^{+4.2} _{-3.7}	718 ⁺⁸³ ₋₈₃	18.99 ^{+0.17} _{-0.16}	61 ⁺¹⁰ ₋₉
WISEA J002909.90+190516.6	7.0	13.18 ^{+0.30} _{-0.30}	26.6 ^{+4.0} _{-3.4}	827 ⁺⁸² ₋₈₂	17.73 ^{+0.30} _{-0.27}	39 ⁺⁸ ₋₇
WISEU J004851.21+250814.9	8.5	13.89 ^{+0.30} _{-0.30}	14.8 ^{+2.2} _{-1.9}	588 ⁺⁸² ₋₈₂	20.22 ^{+0.04} _{-0.04}	87 ⁺¹³ ₋₁₁
WISEU J005559.88+594745.0	7.0	13.23 ^{+0.30} _{-0.30}	22.2 ^{+3.3} _{-2.9}	801 ⁺⁸² ₋₈₂	18.02 ^{+0.14} _{-0.13}	43 ⁺⁷ ₋₆
WISEA J010116.12-520629.8	8.5	13.82 ^{+0.31} _{-0.31}	23.7 ^{+3.7} _{-3.2}	607 ⁺⁸⁴ ₋₈₃	19.96 ^{+0.14} _{-0.13}	80 ⁺¹³ ₋₁₂
WISEA J012057.06-764216.4	8.0	13.66 ^{+0.31} _{-0.31}	26.7 ^{+4.1} _{-3.6}	649 ⁺⁸⁴ ₋₈₄	18.21 ^{+0.31} _{-0.27}	39 ⁺⁸ ₋₇
WISEA J012834.87-280302.5	6.0	13.02 ^{+0.30} _{-0.30}	31.5 ^{+4.7} _{-4.1}	923 ⁺⁸² ₋₈₂	17.51 ^{+0.35} _{-0.30}	38 ⁺⁸ ₋₇
WISEA J013217.78-581825.9	9.0	14.03 ^{+0.32} _{-0.32}	22.0 ^{+3.5} _{-3.0}	558 ⁺⁸⁴ ₋₈₄	18.96 ^{+0.22} _{-0.20}	46 ⁺⁸ ₋₈
WISEU J013522.46-221957.3	6.5	13.13 ^{+0.30} _{-0.30}	34.1 ^{+5.1} _{-4.4}	855 ⁺⁸³ ₋₈₃	18.66 ^{+0.26} _{-0.23}	61 ⁺¹¹ ₋₁₀
WISEA J013810.78-412220.2	6.0	13.03 ^{+0.30} _{-0.30}	42.9 ^{+6.4} _{-5.6}	911 ⁺⁸⁴ ₋₈₄	20.28 ^{+0.29} _{-0.26}	133 ⁺²⁶ ₋₂₄
WISEA J014603.23-261908.7	7.5	13.43 ^{+0.31} _{-0.31}	29.9 ^{+4.5} _{-3.9}	722 ⁺⁸⁴ ₋₈₃	19.79 ^{+0.21} _{-0.19}	89 ⁺¹⁶ ₋₁₄
WISEA J015507.35-421635.7	9.0	14.13 ^{+0.34} _{-0.34}	25.5 ^{+4.3} _{-3.7}	537 ⁺⁸⁷ ₋₈₇	19.63 ^{+0.26} _{-0.23}	60 ⁺¹² ₋₁₁
WISEA J021420.18-573245.1	8.5	13.71 ^{+0.32} _{-0.32}	30.8 ^{+4.9} _{-4.2}	633 ⁺⁸⁶ ₋₈₆	19.78 ^{+0.24} _{-0.21}	77 ⁺¹⁵ ₋₁₃
WISEA J025756.40-265528.8	9.5	14.35 ^{+0.34} _{-0.34}	20.9 ^{+3.6} _{-3.1}	496 ⁺⁸⁶ ₋₈₆	19.65 ^{+0.24} _{-0.21}	54 ⁺¹¹ ₋₁₀
WISEA J025805.29-321917.4	5.5	12.92 ^{+0.30} _{-0.30}	25.9 ^{+3.9} _{-3.4}	1006 ⁺⁸² ₋₈₂	16.66 ^{+0.20} _{-0.19}	27 ⁺⁵ ₋₄
WISEA J030534.09-582635.5	8.0	13.60 ^{+0.31} _{-0.30}	24.2 ^{+3.7} _{-3.2}	667 ⁺⁸³ ₋₈₃	18.56 ^{+0.17} _{-0.16}	47 ⁺⁸ ₋₇
WISEA J032600.28+421056.8	8.5	13.74 ^{+0.31} _{-0.30}	20.4 ^{+3.1} _{-2.7}	626 ⁺⁸² ₋₈₂	18.65 ^{+0.19} _{-0.17}	45 ⁺⁸ ₋₇
WISEA J032811.00-422321.6	8.5	13.70 ^{+0.31} _{-0.31}	29.2 ^{+4.5} _{-3.9}	638 ⁺⁸⁵ ₋₈₅	19.90 ^{+0.19} _{-0.18}	82 ⁺¹⁵ ₋₁₃
WISEA J034227.44-462252.0	7.5	13.33 ^{+0.31} _{-0.31}	36.4 ^{+5.5} _{-4.8}	761 ⁺⁸⁵ ₋₈₅	18.47 ^{+0.32} _{-0.28}	51 ⁺¹⁰ ₋₁₀
WISEA J035733.85+070557.4	6.5	13.11 ^{+0.30} _{-0.30}	28.8 ^{+4.3} _{-3.7}	866 ⁺⁸² ₋₈₂	18.69 ^{+0.20} _{-0.19}	62 ⁺¹¹ ₋₁₀
WISEA J040702.42+190945.8	6.5	13.15 ^{+0.30} _{-0.30}	28.7 ^{+4.2} _{-3.7}	841 ⁺⁸² ₋₈₂	18.10 ^{+0.34} _{-0.29}	46 ⁺¹⁰ ₋₉
WISEA J042236.95-044203.5	8.0	13.52 ^{+0.31} _{-0.31}	30.5 ^{+4.6} _{-4.0}	692 ⁺⁸⁴ ₋₈₄	21.58 ^{+0.09} _{-0.09}	194 ⁺³¹ ₋₂₇
WISEA J050238.28+100750.0	9.0	14.05 ^{+0.31} _{-0.31}	18.3 ^{+2.8} _{-2.4}	553 ⁺⁸³ ₋₈₃	17.63 ^{+0.31} _{-0.27}	25 ⁺⁵ ₋₅
WISEU J050305.68-564834.0	≥11.0	15.56 ^{+0.51} _{-0.49}	12.4 ^{+3.1} _{-2.6}	348 ⁺⁸⁹ ₋₈₇	20.70 ^{+0.07} _{-0.07}	51 ⁺¹³ ₋₁₁
WISEA J050615.56-514521.3	9.0	13.98 ^{+0.34} _{-0.33}	28.3 ^{+4.7} _{-4.1}	569 ⁺⁸⁸ ₋₈₇	18.40 ^{+0.32} _{-0.28}	36 ⁺⁸ ₋₇
WISEA J053512.01-773829.7	9.5	14.18 ^{+0.33} _{-0.33}	21.9 ^{+3.6} _{-3.1}	528 ⁺⁸⁵ ₋₈₅	17.88 ^{+0.30} _{-0.26}	26 ⁺⁵ ₋₅
WISEA J064503.72+524054.1	8.5	13.85 ^{+0.31} _{-0.30}	18.1 ^{+2.7} _{-2.4}	598 ⁺⁸² ₋₈₂	20.13 ^{+0.05} _{-0.05}	85 ⁺¹³ ₋₁₁
WISEA J065113.90-835502.6	8.0	13.68 ^{+0.31} _{-0.31}	23.5 ^{+3.6} _{-3.1}	643 ⁺⁸³ ₋₈₃	17.84 ^{+0.21} _{-0.19}	32 ⁺⁶ ₋₅
WISEA J075438.20+090044.9	8.0	13.62 ^{+0.31} _{-0.31}	26.6 ^{+4.0} _{-3.5}	660 ⁺⁸³ ₋₈₃	18.30 ^{+0.39} _{-0.33}	41 ⁺⁹ ₋₉
WISEA J080622.22-082046.5	8.0	13.67 ^{+0.31} _{-0.31}	22.3 ^{+3.4} _{-2.9}	645 ⁺⁸³ ₋₈₃	21.14 ^{+0.06} _{-0.06}	148 ⁺²³ ₋₂₀
WISEA J083011.95+283716.0 ^a	≥11.0	16.19 ^{+0.57} _{-0.55}	8.6 ^{+2.5} _{-2.0}	303 ⁺⁸⁷ ₋₈₅	22.42 ^{+0.07} _{-0.07}	84 ⁺²⁴ ₋₁₉
WISEA J083019.97-632305.4	8.0	13.59 ^{+0.31} _{-0.31}	26.1 ^{+4.0} _{-3.4}	668 ⁺⁸³ ₋₈₃	19.20 ^{+0.12} _{-0.12}	63 ⁺¹⁰ ₋₉
WISEA J084329.01+694709.8	6.0	13.01 ^{+0.30} _{-0.30}	39.9 ^{+5.9} _{-5.2}	928 ⁺⁸³ ₋₈₃	18.81 ^{+0.34} _{-0.29}	69 ⁺¹⁴ ₋₁₃
WISEA J101804.20-684254.0	8.5	13.71 ^{+0.31} _{-0.31}	21.8 ^{+3.3} _{-2.9}	633 ⁺⁸³ ₋₈₃	19.95 ^{+0.07} _{-0.07}	84 ⁺¹³ ₋₁₁
WISEA J104216.89-003935.9	7.5	13.37 ^{+0.30} _{-0.30}	29.9 ^{+4.5} _{-3.9}	744 ⁺⁸³ ₋₈₃	19.23 ^{+0.24} _{-0.22}	70 ⁺¹³ ₋₁₂
WISEA J105349.41-460241.2	8.5	13.69 ^{+0.30} _{-0.30}	20.6 ^{+3.1} _{-2.7}	639 ⁺⁸² ₋₈₂	19.66 ^{+0.09} _{-0.09}	74 ⁺¹² ₋₁₀
WISEA J105917.38+285729.3	7.5	13.45 ^{+0.30} _{-0.30}	26.8 ^{+4.0} _{-3.5}	713 ⁺⁸³ ₋₈₃	19.56 ^{+0.17} _{-0.16}	79 ⁺¹³ ₋₁₂
WISEA J110201.76+350335.4	9.0	14.04 ^{+0.31} _{-0.31}	16.6 ^{+2.5} _{-2.2}	556 ⁺⁸² ₋₈₂	16.31 ^{+0.41} _{-0.35}	13 ⁺³ ₋₃
WISEA J112440.19+663052.0	8.0	13.62 ^{+0.30} _{-0.30}	21.9 ^{+3.3} _{-2.9}	660 ⁺⁸² ₋₈₂	16.23 ^{+0.45} _{-0.37}	16 ⁺⁴ ₋₄
WISEA J114350.90+401333.9	8.5	13.70 ^{+0.31} _{-0.31}	22.7 ^{+3.4} _{-3.0}	636 ⁺⁸³ ₋₈₃	19.46 ^{+0.15} _{-0.14}	67 ⁺¹¹ ₋₁₀
WISEA J114601.22+342458.8	7.0	13.20 ^{+0.30} _{-0.30}	28.1 ^{+4.2} _{-3.7}	815 ⁺⁸² ₋₈₂	18.88 ^{+0.18} _{-0.17}	65 ⁺¹¹ ₋₁₀
WISEA J115917.89+671704.2	9.0	14.08 ^{+0.33} _{-0.32}	23.7 ^{+3.8} _{-3.3}	547 ⁺⁸⁵ ₋₈₅	20.59 ^{+0.16} _{-0.15}	95 ⁺¹⁷ ₋₁₅
WISEA J125721.01+715349.3	≥11.0	15.05 ^{+0.45} _{-0.43}	16.6 ^{+3.7} _{-3.1}	398 ⁺⁹⁰ ₋₈₈	21.05 ^{+0.13} _{-0.12}	75 ⁺¹⁷ ₋₁₅
CWISEP J135937.65-435226.9	9.5	14.19 ^{+0.33} _{-0.33}	22.1 ^{+3.6} _{-3.1}	525 ⁺⁸⁵ ₋₈₅	18.54 ^{+0.47} _{-0.39}	35 ⁺⁹ ₋₈
WISEA J143422.31-083934.2	9.0	13.93 ^{+0.32} _{-0.32}	24.3 ^{+3.8} _{-3.3}	580 ⁺⁸⁴ ₋₈₄	19.58 ^{+0.29} _{-0.26}	64 ⁺¹³ ₋₁₂
WISEA J151620.39+721745.4	9.0	14.15 ^{+0.33} _{-0.33}	22.8 ^{+3.7} _{-3.2}	532 ⁺⁸⁵ ₋₈₅	20.41 ^{+0.10} _{-0.10}	85 ⁺¹⁴ ₋₁₃
WISEA J152529.09+605356.5	9.0	14.03 ^{+0.32} _{-0.32}	23.5 ^{+3.7} _{-3.2}	559 ⁺⁸⁵ ₋₈₄	20.54 ^{+0.10} _{-0.10}	95 ⁺¹⁶ ₋₁₄
WISEAR J154025.77-113940.8	7.0	13.24 ^{+0.30} _{-0.30}	34.5 ^{+5.2} _{-4.5}	800 ⁺⁸⁴ ₋₈₃	20.64 ^{+0.19} _{-0.18}	144 ⁺²⁵ ₋₂₂
WISEA J155349.96+693355.2	5.0	12.53 ^{+0.25} _{-0.24}	38.6 ^{+4.6} _{-4.2}	-	22.13 ^{+0.06} _{-0.06}	395 ⁺⁴⁸ ₋₄₄
WISEA J160516.79+002139.0	8.5	13.72 ^{+0.31} _{-0.31}	22.6 ^{+3.4} _{-3.0}	633 ⁺⁸³ ₋₈₃	18.10 ^{+0.26} _{-0.24}	36 ⁺⁷ ₋₆
WISEA J162852.64+160421.0	8.5	13.76 ^{+0.31} _{-0.31}	26.1 ^{+4.0} _{-3.5}	621 ⁺⁸⁴ ₋₈₄	20.96 ^{+0.11} _{-0.11}	131 ⁺²¹ ₋₁₉
WISEA J163932.75+184049.4	9.5	14.25 ^{+0.31} _{-0.31}	16.8 ^{+2.6} _{-2.3}	514 ⁺⁸³ ₋₈₃	18.97 ^{+0.15} _{-0.14}	42 ⁺⁷ ₋₆
WISEA J171331.68+245000.9	7.5	13.43 ^{+0.31} _{-0.31}	30.4 ^{+4.6} _{-4.0}	721 ⁺⁸⁴ ₋₈₃	18.69 ^{+0.40} _{-0.34}	54 ⁺¹² ₋₁₁
WISEA J172907.10-753017.0	7.0	13.18 ^{+0.30} _{-0.30}	28.0 ^{+4.2} _{-3.6}	826 ⁺⁸² ₋₈₂	16.77 ^{+0.36} _{-0.31}	25 ⁺⁵ ₋₅

Table 9
(Continued)

Name	SpT (phototype)	M_{ch2} (mag)	Distance (pc)	T_{eff} (K)	H_{ch2} (mag)	V_{tan} (km s ⁻¹)
WISEA J175328.55–590447.6	9.0	14.04 ^{+0.31} _{-0.31}	17.0 ^{+2.6} _{-2.2}	555 ⁺⁸² ₋₈₂	18.10 ^{+0.22} _{-0.20}	31 ⁺⁵ ₋₅
WISEA J181849.59–470146.9	8.5	13.87 ^{+0.30} _{-0.30}	17.3 ^{+2.6} _{-2.3}	593 ⁺⁸² ₋₈₂	18.64 ^{+0.13} _{-0.12}	43 ⁺⁷ ₋₆
WISEA J190005.76–310810.9	9.0	13.91 ^{+0.30} _{-0.30}	14.9 ^{+2.2} _{-2.0}	583 ⁺⁸² ₋₈₂	17.19 ^{+0.23} _{-0.21}	21 ⁺⁴ ₋₄
WISEA J193054.55–205949.4	≥11.0	15.99 ^{+0.39} _{-0.38}	7.1 ^{+1.4} _{-1.2}	315 ⁺⁸³ ₋₈₂	21.10 ^{+0.06} _{-0.06}	50 ⁺¹⁰ ₋₈
WISEA J201833.67–141720.3	9.0	14.07 ^{+0.31} _{-0.31}	15.3 ^{+2.3} _{-2.0}	550 ⁺⁸² ₋₈₂	16.47 ^{+0.40} _{-0.34}	14 ⁺³ ₋₃
WISEA J205921.85+662725.2	8.0	13.67 ^{+0.31} _{-0.31}	23.5 ^{+3.6} _{-3.1}	644 ⁺⁸³ ₋₈₃	19.07 ^{+0.12} _{-0.12}	57 ⁺⁹ ₋₈
WISEA J211456.86–180519.0	8.0	13.63 ^{+0.30} _{-0.30}	18.3 ^{+2.7} _{-2.4}	657 ⁺⁸² ₋₈₂	19.03 ^{+0.11} _{-0.11}	57 ⁺⁹ ₋₈
WISEA J212510.91–730758.8	8.0	13.58 ^{+0.31} _{-0.31}	24.9 ^{+3.8} _{-3.3}	672 ⁺⁸³ ₋₈₃	19.33 ^{+0.16} _{-0.15}	67 ⁺¹¹ ₋₁₀
WISEA J214025.23–332707.4	8.5	13.83 ^{+0.32} _{-0.32}	28.7 ^{+4.6} _{-4.0}	602 ⁺⁸⁶ ₋₈₆	20.22 ^{+0.24} _{-0.22}	90 ⁺¹⁷ ₋₁₆
WISEU J215018.46–752053.0	6.5	13.15 ^{+0.30} _{-0.30}	31.4 ^{+4.7} _{-4.1}	843 ⁺⁸³ ₋₈₃	20.56 ^{+0.09} _{-0.09}	144 ⁺²² ₋₂₀
WISEAR J220746.67–503631.7	7.5	13.41 ^{+0.31} _{-0.31}	33.0 ^{+5.0} _{-4.3}	729 ⁺⁸⁴ ₋₈₄	21.71 ^{+0.16} _{-0.15}	216 ⁺³⁶ ₋₃₂
WISEA J221859.33+114644.4	7.5	13.35 ^{+0.30} _{-0.30}	20.4 ^{+3.0} _{-2.6}	753 ⁺⁸² ₋₈₂	17.60 ^{+0.21} _{-0.19}	34 ⁺⁶ ₋₅
WISEA J221841.38+143003.4	7.5	13.36 ^{+0.30} _{-0.30}	24.2 ^{+3.6} _{-3.2}	748 ⁺⁸² ₋₈₂	18.75 ^{+0.15} _{-0.14}	57 ⁺⁹ ₋₈
WISEA J224319.56–145857.3	10.0	14.49 ^{+0.32} _{-0.32}	14.8 ^{+2.3} _{-2.0}	473 ⁺⁸³ ₋₈₃	19.27 ^{+0.19} _{-0.17}	43 ⁺⁸ ₋₇
WISEA J225404.16–265257.5	9.5	14.22 ^{+0.31} _{-0.31}	15.7 ^{+2.4} _{-2.1}	519 ⁺⁸² ₋₈₂	18.98 ^{+0.22} _{-0.20}	42 ⁺⁸ ₋₇
WISEA J230930.58+145633.1	7.0	13.17 ^{+0.30} _{-0.30}	28.7 ^{+4.3} _{-3.7}	833 ⁺⁸² ₋₈₂	20.00 ^{+0.17} _{-0.15}	110 ⁺¹⁸ ₋₁₆
WISEA J233816.47–732929.7	9.0	13.97 ^{+0.31} _{-0.31}	20.5 ^{+3.1} _{-2.7}	571 ⁺⁸³ ₋₈₃	19.94 ^{+0.09} _{-0.09}	74 ⁺¹² ₋₁₀
WISEA J235456.63–481440.1	9.5	14.17 ^{+0.33} _{-0.32}	21.7 ^{+3.5} _{-3.0}	529 ⁺⁸⁵ ₋₈₄	19.19 ^{+0.25} _{-0.22}	48 ⁺⁹ ₋₈

Notes. Photometric spectral type values are defined such that SpT = 6 for T6, SpT = 7 for T7, ..., SpT = 11 for Y1. WISEA J053535.43–644518.5 is omitted from this table despite being motion confirmed, since its relatively blue ch1–ch2 ≈ 0 color does not provide a well-constrained Spitzer-based phototype. WISEU J224547.11–433341.5 has been omitted because it lacks a ch1 magnitude and hence a Spitzer phototype.

^a Bardalez Gagliuffi et al. (2020) present a trigonometric parallax for WISEA J083011.95+283716.0 yielding more reliable estimates for its phototype, M_{ch2} , distance, T_{eff} , and V_{tan} .

(This table is available in machine-readable form.)

11.4. Absence of Discoveries as Cold as WISE 0855–0714

Although WISEA 0830+2837 may potentially be similar to WISE 0855–0714 (the coldest known brown dwarf) in terms of ch1–ch2 and F125W–ch2 colors, WISEA 0830+2837 is ~ 1.5 mag more luminous at ch2 (Bardalez Gagliuffi et al. 2020) and thus presumably warmer. Therefore, recent Spitzer follow-up from Backyard Worlds and CatWISE appears not to have identified even one object as cold as or colder than WISE 0855–0714 ($T_{\text{eff}} \approx 250$ K; Luhman 2014b). This may seem surprising given that motion surveys like Backyard Worlds and CatWISE are pushing much deeper than the relatively bright WISE 0855–0714 magnitude of W2 ≈ 14 (see Figure 2). Wright et al. (2014) argued that a complete search of the WISE data to W2 = 16 should find between 3 (16th percentile) and 34 (84th percentile) additional objects²⁵ comparable to WISE 0855–0714, with a median of 14. The Backyard Worlds and CatWISE Spitzer target lists both have complex selection functions because they each amalgamate results from numerous contributing searches, but it is unlikely that either (or their union) is currently complete to W2 = 16 (see esp. Section 3.3 of Eisenhardt et al. 2020 regarding CatWISE Preliminary incompleteness). Adjusting the Wright et al. (2014) prediction to the typical magnitude of our Backyard Worlds sample (W2 ≈ 15.7 ; see Section 5) yields a corresponding 16th–84th percentile range of 1.6–22 WISE 0855–0714 analogs, with a median of 9.

We find it conceivable that a small number of WISE 0855–0714 analogs have been detected by WISE/NEOWISE but

have so far not been pinpointed by either Backyard Worlds or CatWISE. For instance, the combined Backyard Worlds and CatWISE motion discovery lists total ~ 4000 objects, yet fewer than 300 of these were imaged with Spitzer. One cannot predict which WISE sources will turn out to be reddest in Spitzer based on faint W2 detections alone, so it is certainly possible that the parent Backyard Worlds plus CatWISE motion discovery samples contain new WISE 0855–0714 analogs not yet recognized as such owing to lack of Spitzer follow-up. This potential incompleteness affects both Backyard Worlds and CatWISE and could easily arise from, e.g., blending of an extremely cold brown dwarf with one or more background contaminants, yielding a spuriously blue W1–W2 color. Another selection bias specific to CatWISE is that very faint and fast-moving sources may not appear in the catalog at all, since CatWISE source detection is performed on static sky co-adds spanning more than half a decade (Eisenhardt et al. 2020), significantly diluting the appearance of objects moving faster than $\sim 1''$ yr⁻¹.

To summarize, the absence of additional objects as cold as WISE 0855–0714 suggests that their true abundance is probably not on the higher side of imprecise estimates based purely on the nearby location of WISE 0855–0714 (i.e., there likely are not of order 10 such objects with W2 < 15.7). On the other hand, the absence of such discoveries in the Backyard Worlds and CatWISE Spitzer follow-up samples (zero identified vs. 1.6 expected at the distribution’s 16th percentile) does not definitively establish an underabundance relative to the Wright et al. (2014) forecast given the extremely low number statistics and possible incompleteness. An updated 20 pc census of brown dwarfs that incorporates recent Backyard

²⁵ These numbers are lower than those quoted in Wright et al. (2014) by 1 because the Wright et al. (2014) values include WISE 0855–0714 itself.

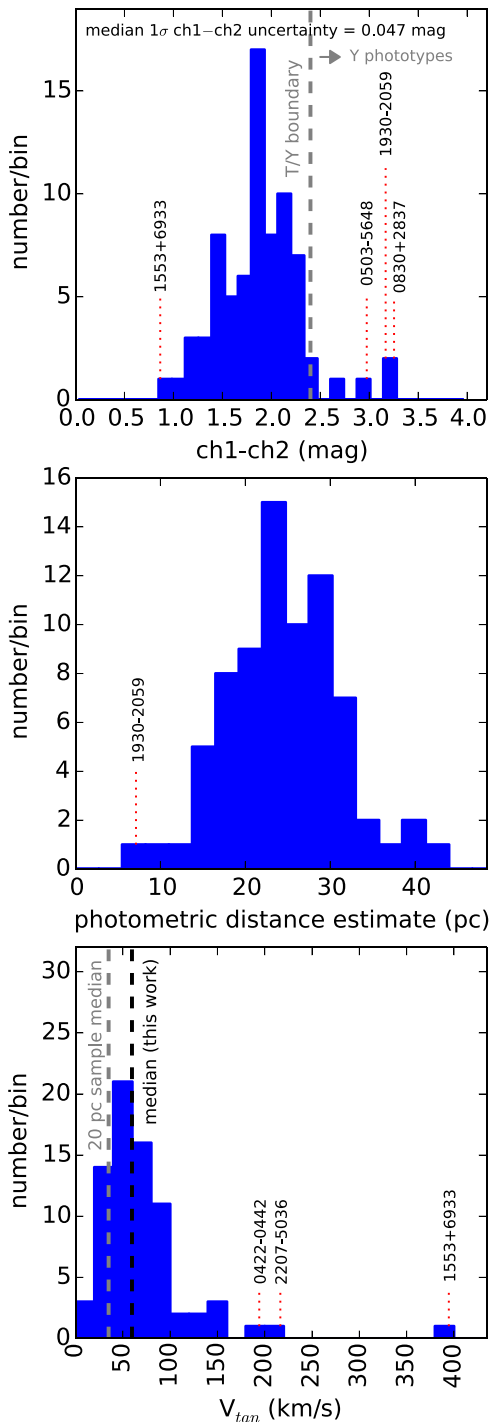


Figure 6. Distributions of Spitzer colors (top), photometric distance estimates (middle), and V_{tan} (bottom) from Table 9 for motion-confirmed targets whose spectral types could be estimated based on our Spitzer photometry. Short names of selected extreme objects are included as annotations.

Worlds and CatWISE discoveries can provide improved space density and mass function estimates, thereby enabling a more rigorous assessment of whether the close-by detection of WISE 0855–0714 is anomalous given its as-yet-unrivaled temperature. That analysis is beyond the scope of this work and will be presented in a dedicated follow-up paper (J. D. Kirkpatrick et al. 2020, in preparation).

11.5. Objects with Largest Motions

11.5.1. Subdwarf Candidates

Few mid-T or later subdwarfs are currently known, so identifying more such examples is a critical step toward developing an understanding of very cold substellar objects at low metallicity (e.g., Zhang et al. 2019). High tangential velocity is a potential indicator of a relatively old object with low metallicity possibly belonging to the Milky Way thick disk or halo. A threshold value for large V_{tan} sometimes employed in solar neighborhood studies is 100 km s^{-1} (e.g., Faherty et al. 2009). Ten objects in Table 9 have central V_{tan} estimates $> 100 \text{ km s}^{-1}$. To highlight only the most extreme of our targets in terms of tangential velocity as potential subdwarfs, we examine the set of motion-confirmed targets with estimated $V_{\text{tan}} > 150 \text{ km s}^{-1}$: WISEA 0422–0442 ($V_{\text{tan}} = 194^{+31}_{-27} \text{ km s}^{-1}$), WISEA 1553+6933 ($V_{\text{tan}} = 395^{+48}_{-44} \text{ km s}^{-1}$), and WISEAR 2207–5036 ($V_{\text{tan}} = 216^{+36}_{-32} \text{ km s}^{-1}$). Mid- to late T subdwarfs may have unusually red J – ch2 colors relative to their ch1 – ch2 colors (e.g., Mace et al. 2013), motivating a check of whether available NIR photometry indicates that our high- V_{tan} outliers are also color outliers. As shown in Figure 5, WISEAR 2207–5036 has a substantially redder $J - \text{ch2}$ color limit than would be expected for a normal brown dwarf with its $\text{ch1} - \text{ch2} = 1.66 \pm 0.06$ color, bolstering its subdwarf candidacy. On the other hand, WISEA 0422–0442 has an NIR detection ($J = 19.43 \pm 0.23$), yielding a $J - \text{ch2} = 3.49 \pm 0.23$ color that is consistent with its T8 phototype.

WISEA 1553+6933 stands apart from the rest of our brown dwarf candidates as a result of its exceedingly high tangential velocity estimate. WISEA 1553+6933 is also our sample’s fastest-moving source in terms of best-fit total linear motion ($\mu > 2'' \text{ yr}^{-1}$). Despite not being especially faint by the standards of our sample ($\text{ch2} \approx 15.5$), it was missed by prior searches owing to severe blending with a static background source during pre-hibernation WISE observations. Our OMM follow-up establishes a limit of $J > 17.34$ for WISEA 1553+6933, corresponding to a $J - \text{ch2} > 1.88$ color constraint. This color limit is not sufficiently stringent to rule out the possibility that WISEA 1553+6933 is a normal mid-T brown dwarf. WISEA 1553+6933 merits additional follow-up as a candidate mid- to late T-type subdwarf, including deeper J -band imaging.

11.5.2. Reduced Proper Motion

Reduced proper motion can be a valuable tool for identifying low-luminosity sources, such as Y dwarfs and subdwarfs, in the absence of trigonometric parallaxes. Since our sample lacks trigonometric parallaxes, we cannot directly compute absolute ch2 magnitudes to pinpoint our most intrinsically faint sources. Reduced proper motion replaces parallax in the absolute magnitude formula with total proper motion, on the premise that large apparent motion tends to indicate that a source is relatively nearby. Thus, we can single out objects of especially low luminosity within our sample (independent of absolute magnitude vs. color relations) based on their large reduced proper motions.

Figure 8 shows the reduced proper motions of our sample as a function of $\text{ch1} - \text{ch2}$ color. In this reduced proper-motion diagram, our sample’s reddest objects (by $\text{ch1} - \text{ch2}$ color) are beginning to bridge a previously wide gap between the coldest known brown dwarf (WISE 0855–0714; Luhman 2014b) and

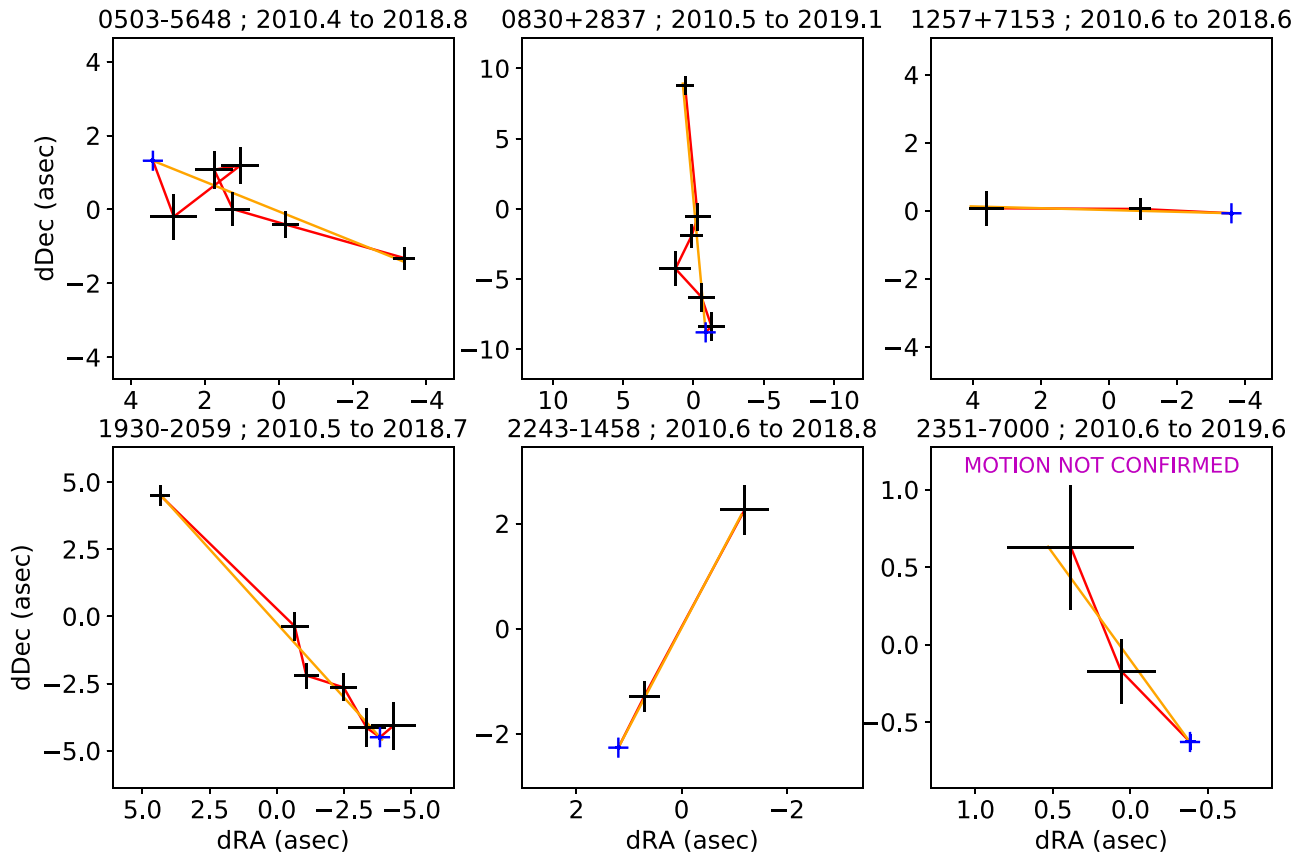


Figure 7. Combined WISE+Spitzer astrometry for our six targets with best-fit $\text{ch1}-\text{ch2} > 2.4$ mag, corresponding to phototypes $\geq Y0$. Each panel’s title lists the short object identifier and time period spanned by its astrometry. All but WISEA 2351–7000 are motion confirmed. The WISEA 2351–7000 trajectory appears plausibly linear, but its significance of motion falls just short of exceeding our χ^2_{motion} threshold for motion confirmation. dR.A. (dDecl.) is the positional offset along the R.A. (decl.) direction relative to the midway point between the minimum and maximum R.A. (decl.) for each object. dR.A. is in units of angular separation, rather than being a simple difference of R.A. coordinate values. Black plus signs represent the WISE W2 locations and their $\pm 1\sigma$ uncertainties. Spitzer astrometry is represented by a blue plus sign of arbitrary size in each panel; the actual Spitzer uncertainties are much smaller than these symbols and would be difficult to perceive if plotted to scale. Red line segments follow the astrometric measurements in a time-ordered fashion. The best-fit linear motion solutions (Table 6) are shown as orange lines and cover the same time period spanned by the combined set of WISE and Spitzer detections. As illustrated by the relatively large size of the black plus signs, the time series of measured WISE positions can be quite noisy. For example, the loop-like phenomenon seen for WISEU 0503–5648 results from centroid measurement noise, not parallax motion.

the rest of the Y dwarf population. WISEA 0830+2837 in particular stands out as inhabiting this formerly empty region of parameter space and has the largest reduced proper motion of any member of our sample ($H_{\text{ch2}} = 22.42 \pm 0.07$ mag). Note that WISEA 0830+2837 is indeed alone in the gap between WISE 0855–0714 and other Y dwarfs. CWISEP 1446–2317 previously fell in a similar region of parameter space, but its $\text{ch1}-\text{ch2}$ color has recently been revised substantially blueward relative to that initially presented in Meisner et al. (2020). Still, the WISEA 0830+2837 reduced proper motion is lower than that of WISE 0855–0714 by more than a magnitude. As discussed in Bardalez Gagliuffi et al. (2020), WISEA 0830+2837 may represent a heretofore missing link between the bulk of the as-yet-identified Y dwarfs and WISE 0855–0714. WISEA 1553+6933 has the second-highest reduced proper motion among our sample, with $H_{\text{ch2}} = 22.13 \pm 0.06$, while also being one of our bluest targets in $\text{ch1}-\text{ch2}$ color; we suspect that WISEA 1553+6933 is a T-type subdwarf on account of its high kinematics (Section 11.5.1).

11.5.3. Total Linear Motion

Nine of our motion-confirmed discoveries have best-fit total linear motions larger than $1'' \text{ yr}^{-1}$: WISEU 0048+2508, WISEA

0422–0442, WISEA 0806–0820, WISEA 0830+2837, WISEA 1553+6933, WISEA 1628+1604, WISEA 1930–2059, WISEAR 2207–5036, and WISEA 2245–4333. Of these nine, two have best-fit total linear motions larger than $2'' \text{ yr}^{-1}$: WISEA 0830+2837 and WISEA 1553+6933. The suspected subdwarf WISEA 1553+6933 has the largest total linear motion among our sample, with $\mu = 2160 \pm 55 \text{ mas yr}^{-1}$. Several of our discoveries with $\mu_{\text{tot}} > 1'' \text{ yr}^{-1}$ were missed by prior brown dwarf color selections owing to blending at early WISE epochs: CWISE 0002+6352, WISEU 0048+2508, WISEA 1553+6933, WISEA 1930–2059, and WISEU 2245–4333. By visually surveying for motion, Backyard Worlds citizen scientists were able to spot these previously overlooked members of the solar neighborhood.

11.6. Candidate CPM Systems

Five of our targets were considered potential CPM companions to earlier-type primaries upon being selected for Spitzer follow-up, and a sixth CPM candidate (CWISE 0002+6352) has archival Spitzer data available. The comoving pair consisting of WISEU 2150–7520 and its L dwarf primary has already been discussed extensively in Faherty et al. (2020). WISEU 0505+3043 was targeted as a possible comoving

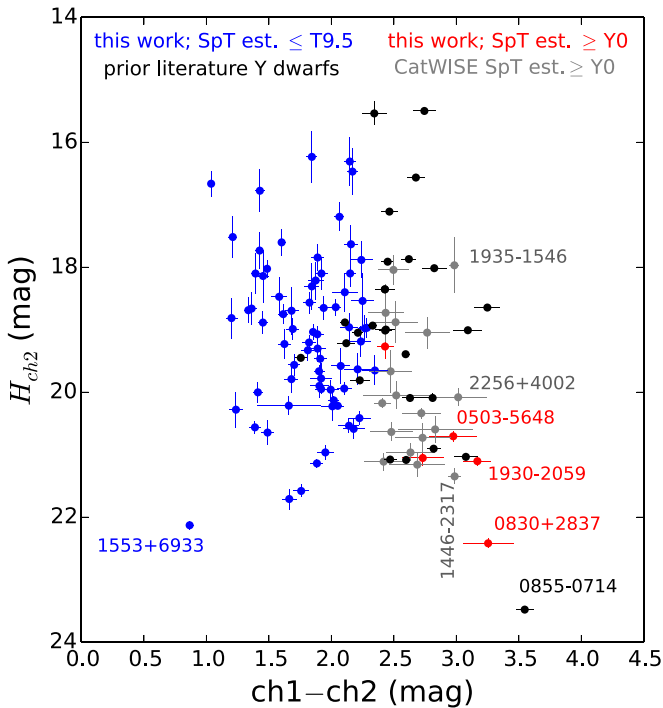


Figure 8. Reduced proper-motion diagram showing all Y dwarfs from the prior literature (black) and all motion-confirmed targets from this study with Spitzer phototypes available. Our targets with best-fit $ch1-ch2$ color most consistent with spectral type Y are shown in red, while all of our objects with earlier spectral type estimates are shown in blue. Recent CatWISE discoveries with Spitzer-based Y phototypes are also plotted in gray (Meisner et al. 2020). Our three discoveries with largest central $ch1-ch2$ colors are individually labeled (red annotations), as are the three reddest CatWISE discoveries (gray annotations; Marocco et al. 2019, 2020; Meisner et al. 2020).

companion to the extreme subdwarf LSPM J0505+3043 but turned out to be entirely spurious (see Table 1). The other remaining four CPM candidates are discussed in detail below.

11.6.1. CWISE J000229.93+635217.0

The motion of CWISE 0002+6352 appears strikingly similar to that of the $\sim 5'$ distant DC white dwarf LSR J0002+6357 (Limoges et al. 2015), which has accurate parallax and proper-motion measurements available from Gaia. Our WISE+Spitzer linear motion fitting gives $\mu_\alpha = 802 \pm 49 \text{ mas yr}^{-1}$, $\mu_\delta = 44 \pm 47 \text{ mas yr}^{-1}$ for CWISE 0002+6352, versus $\mu_\alpha = 918.9 \pm 0.1 \text{ mas yr}^{-1}$, $\mu_\delta = 108.3 \pm 0.1 \text{ mas yr}^{-1}$ for LSR J0002+6357 (Gaia Collaboration et al. 2018). The CWISE 0002+6352 R.A. (decl.) motion component differs from that of LSR J0002+6357 by 2.4σ (1.3σ). Additionally, the Gaia parallax of LSR J0002+6357 (38.1 mas, corresponding to 26.3 pc) places it within the 1σ photometric distance interval of CWISE 0002+6352 ($28.6_{-5.1}^{+5.6}$ pc; Table 9). Restricting to this distance range, only 12 sources in the entire Gaia DR2 catalog have both proper-motion components consistent with those of CWISE 0002+6352 to within 3σ . Therefore, the probability of having one such Gaia source land at least as close on the sky as LSR J0002+6357 does to CWISE 0002+6352 by random chance is 7.7×10^{-6} .

While this false-alarm probability suggests a good likelihood that CWISE 0002+6352 is a bona fide companion to LSR J0002+6357, the moderate motion discrepancies remain concerning, particularly the difference of $>100 \text{ mas yr}^{-1}$ along the R.A. direction. Significant blending of the brown dwarf's WISE counterpart at essentially all epochs in this highly

crowded field (see Figure 9) means that our WISE+Spitzer motion may carry systematic uncertainties larger than those we quote based on statistics alone. In addition to a spectroscopic confirmation of CWISE 0002+6352 to corroborate (or discredit) its photometric distance estimate, a future NIR astrometric data point free of blending would help provide a more conclusive determination as to whether CWISE 0002+6352 is indeed physically associated with LSR J0002+6357. Based on its Spitzer photometry, we predict $J \approx 18.8$ for CWISE 0002+6352. CWISE 0002+6352 is not detected by Pan-STARRS (Chambers et al. 2016).

If CWISE 0002+6352 and LSR J0002+6357 are physically associated, their angular separation of $330''.9 \pm 0''.4$ would translate to a projected physical separation of $8691 \pm 20 \text{ au}$. This would be the second-largest projected physical separation of any known white dwarf plus mid- to late T dwarf system, following only LSPM 1459+0857AB (16,500–26,500 au; Day-Jones et al. 2011). LSR J0002+6357 has serendipitous Spitzer observations from the GLIMPSE360 program, with $ch1 = 15.05 \pm 0.05$ and $ch2 = 14.91 \pm 0.08$, though it appears slightly blended with a neighboring source in that archival imaging (see Figure 9).

11.6.2. WISEU J001908.31-094323.3

Based on visual inspection, we recognized WISEU 0019-0943 to share a very similar motion with the nearby M dwarf LP 704-85. Our WISEU 0019-0943 linear motion agrees with the Gaia DR2 proper motion of LP 704-85 to within 1σ in terms of both μ_α and μ_δ . WISEU 0019-0943 is $19''.1 \pm 0''.4$ distant from LP 704-85, comparing the Gaia epoch 2015.5 position of LP 704-85 to that predicted at the same epoch by our linear motion model for WISEU 0019-0943. Using the full-sky Gaia DR2 catalog, we find that there are only 2601 Gaia sources that have both μ_α and μ_δ within 1σ of the values listed for WISEU 0019-0943 in Table 6. This yields a chance alignment probability of 5.6×10^{-6} .

However, our Spitzer-based photometric distance estimate for WISEU 0019-0943 is in some tension with the Gaia DR2 parallax for LP 704-85. The WISEU 0019-0943 photometric distance estimate ($d = 31.1_{-4.0}^{+4.6}$ pc) is 3σ discrepant from the LP 704-85 distance according to Gaia DR2 ($d = 44.9 \pm 0.2$ pc). We note that this discrepancy could be eliminated if WISEU 0019-0943 were itself a pair of T7 brown dwarfs rather than a single T7 brown dwarf, which would then place its central distance estimate at 44.0 pc. Archival VHS images do show a pair of sources near the WISEU 0019-0943 location, separated by $3''.4$. However, the WISEU 0019-0943 Spitzer $ch2$ counterpart looks pointlike, whereas a $\sim 3''$ separation pair of sources with similar $ch2$ apparent brightnesses should have yielded a significantly extended profile given that the $ch2$ PRF FWHM is $\sim 2''$. We therefore believe that one of the nearby VHS NIR detections (the fainter source in J band) is an unrelated background object. We consider our current data to be inconclusive regarding whether WISEU 0019-0943 is indeed physically associated with LP 704-85. If physically associated, the projected separation would be $857 \pm 16 \text{ au}$. LP 704-85 has no published spectrum, but its $J_{2\text{MASS}}$ apparent magnitude and Gaia parallax combine to give an absolute $J_{2\text{MASS}}$ magnitude of 8.9, consistent with spectral type $\sim M4$ (Hawley et al. 2002).

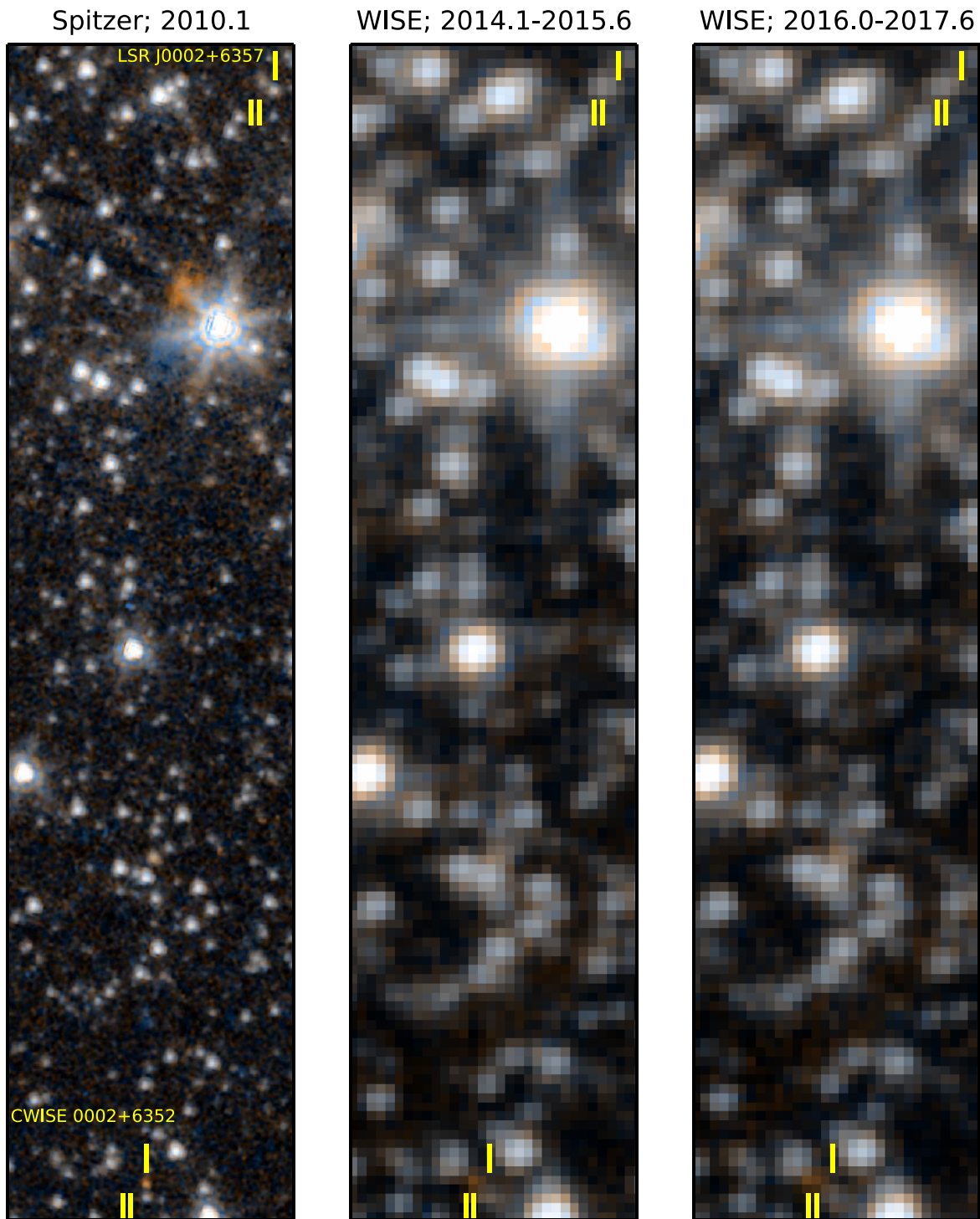


Figure 9. Time series of WISE and Spitzer images illustrating the similar proper motions of our late T discovery CWISE 0002+6352 (bottom of each cutout) and the DC white dwarf LSR J0002+6357 (upper right of each cutout). Each panel is a two-band color-composite rendering. In each case W1 (ch1) is represented by the blue color channel and W2 (ch2) is represented by the red color channel. The Spitzer color composite at left is built from archival GLIMPSE360 imaging. WISE images (middle and right panels) are co-adds spanning different portions of the post-reactivation time period. CWISE 0002+6352 appears distinctively orange in comparison to the relatively white/blue background source population that has $W1 - W2 \approx \text{ch1} - \text{ch2} \approx 0$. East is left and north is up. Yellow vertical lines track the west-to-east motion of this pair over the ~ 2010 – 2018 time period. Each postage stamp is $1''.6 \times 6''.2$ in angular extent. Follow-up NIR astrometry would help to conclusively determine whether CWISE 0002+6352 and LSR J0002+6357 are indeed physically associated by refining the former’s measured proper motion.

11.6.3. WISEU J005559.88+594745.0

Based on visual inspection, we recognized WISEU 0055+5947 to share a very similar motion with the nearby DC white dwarf LSPM J0055+5948 (see Figure 10; Limoges et al. 2013). Our WISEU 0055+5947 linear motion agrees with the

Gaia DR2 proper motion of LSPM J0055+5948 to within 2σ in terms of both μ_α and μ_δ . WISEU 0055+5947 is $17''.6 \pm 0''.1$ distant from LSPM J0055+5948, comparing the Gaia epoch 2015.5 position of LSPM J0055+5948 to that predicted at the same epoch by our linear motion model for WISEU

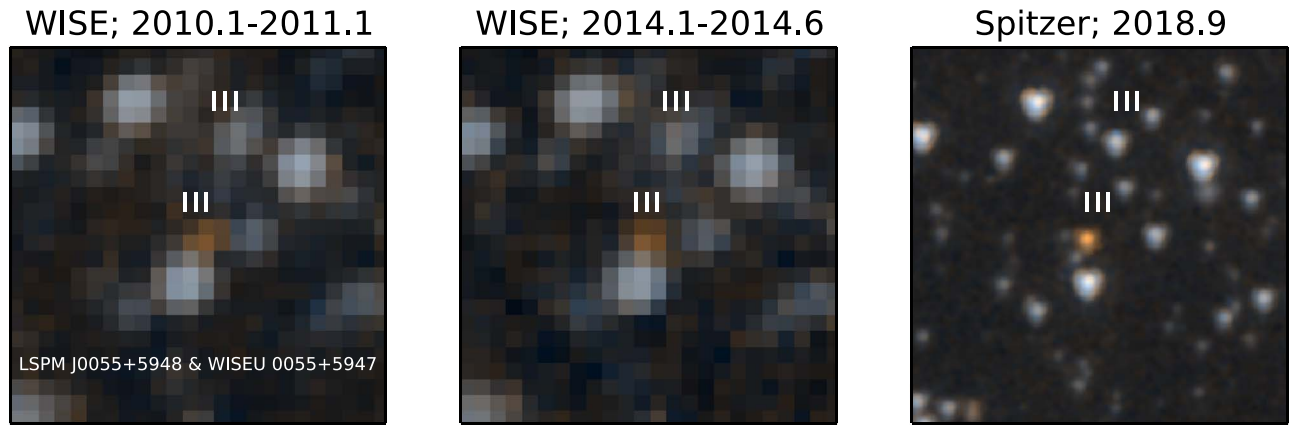


Figure 10. Time series of WISE and Spitzer images illustrating the CPM of our T8 discovery WISEU 0055+5947 (center of each cutout) and the DC white dwarf LSPM J0055+5948 (upper right). Each panel is a two-band color-composite rendering. In each case W1 (ch1) is represented by the blue color channel and W2 (ch2) is represented by the red color channel. WISE images are 1 yr co-adds spanning the pre-hibernation period (left) and first year post-reactivation (middle). The Spitzer color composite at right is built from p14076 IRAC imaging (PI: Faherty). The T8 comoving companion at center is strikingly orange in comparison to the relatively white/blue background source population that has $W1 - W2 \approx \text{ch1} - \text{ch2} \approx 0$. East is left and north is up. The white vertical lines track the west-to-east motion of this pair over the ~ 2010 – 2019 time period. Each postage stamp is $1'.1 \times 1'.1$ in angular extent.

0055+5947. Using the full-sky Gaia DR2 catalog, we find that there are only 351 Gaia sources that have both μ_α and μ_δ within 2σ of the values listed for WISEU 0055+5947 in Table 6. This yields a chance alignment probability of just 6.4×10^{-7} .

The WISEU 0055+5947 photometric distance estimate provides further evidence for physical association with LSPM J0055+5948. The white dwarf has a Gaia parallax of 43.78 ± 0.07 mas, corresponding to a distance of 22.8 pc. This agrees with our Spitzer-based photometric distance estimate for WISEU 0055+5947 ($d = 22.2^{+3.3}_{-2.9}$ pc; Table 9) to within 1σ . Adding further corroboration, our Keck/NIRES spectral type of T8 for the secondary (Section 8) agrees with our photometric estimate of T7 within the expected phototyping uncertainty (Section 11.1). The chance alignment probability drops further to 4.9×10^{-8} when accounting for the consistency of the brown dwarf distance estimate with the white dwarf parallax in combination with the similarity of their proper motions. The projected physical separation between the brown dwarf and white dwarf is 402 ± 3 au using the white dwarf’s Gaia parallax to convert from arcseconds of angular separation to projected au. We conclude that WISEU 0055+5947 is indeed a comoving companion of LSPM J0055+5948. This makes WISEU 0055+5947 an interesting target for further benchmarking studies given the potential for determining the system’s age using that of the white dwarf primary.

LSPM J0055+5948 was identified as a DC white dwarf by Limoges et al. (2015) and is also in the Gentile Fusillo et al. (2019) Gaia DR2 white dwarf catalog. According to Gentile Fusillo et al. (2019), LSPM J0055+5948 has $T_{\text{eff}} = 4623 \pm 21$ K, $\log(g) = 7.82 \pm 0.02$, and $M = 0.474 \pm 0.010M_\odot$ when modeled assuming a pure H atmosphere (Gentile Fusillo et al. 2019), as suggested by Limoges et al. (2013). To confirm these parameters, we also obtained the Pan-STARRS *griz* (Chambers et al. 2016), 2MASS *JHK_s*, and AllWISE W1,W2 photometry of LSPM J0055+5948 and determined T_{eff} and $\log(g)$ using the photometric spectral energy distribution (SED) and Gaia DR2 parallax. For a DA composition and fitting to the Fontaine et al. (2001) cooling models, we obtain $T_{\text{eff}} = 4734 \pm 81$ K and $\log(g) = 7.87 \pm 0.07$, consistent within the uncertainties with the Gentile Fusillo et al. (2019) values.

Using the Gentile Fusillo et al. (2019) parameters and the cooling models from Fontaine et al. (2001) for DA white dwarfs, we determine a cooling time of $5.01^{+0.24}_{-0.23}$ Gyr. We then use the semiempirical initial mass–final mass relationship for white dwarfs from Cummings et al. (2018) to determine the initial mass of the white dwarf progenitor to be $1.38^{+0.47}_{-0.21} M_\odot$, a likely solar-type star. Combining the progenitor mass with the MIST isochrones (Paxton et al. 2011; Dotter 2016), we determine the total age of the system to be 10 ± 3 Gyr. The age we determine is consistent if we use the SED determined T_{eff} and $\log(g)$.

It should be noted that while we have assumed that this DC white dwarf is likely to have a hydrogen-rich atmosphere, the Gentile Fusillo et al. (2019) modeling gives $T_{\text{eff}} = 4654 \pm 17$ K, $\log(g) = 7.84 \pm 0.02$, and $M = 0.473 \pm 0.010M_\odot$ when modeled assuming a pure He atmosphere, which is also consistent with the values we have determined for the white dwarf, meaning that even if LSPM J0055+5948 is a helium atmosphere white dwarf, our estimate of the system age will not change. LSPM J0055+5948 has $\text{ch1} = 14.91 \pm 0.01$ and $\text{ch2} = 14.90 \pm 0.02$ based on our Spitzer follow-up imaging.

Combining our total system age constraint and T_{eff} estimate from Table 9 yields a mass range of $56 \pm 9M_{\text{Jup}}$ for WISEU 0055+5947 based on the Saumon & Marley (2008) model grids.

The WISEU 0055+5947 plus LSPM J0055+5948 pair is currently only the fourth such wide system to be discovered after LSPM 1459+0857AB (Day-Jones et al. 2011), WD 0806-661AB (Luhman et al. 2011), and COCONUTS-1AB (Zhang et al. 2020). The projected separation of ~ 400 au for WISEU 0055+5947 is closer than the other three comoving systems, all of which have projected separations of at least 1000 au (COCONUTS-1AB: 1280 au; WD 0806-661AB: 2500 au; LSPM 1459+0857AB: 16500–26500 au). All four systems have T dwarf companions or later: both COCONUTS-1B and LSPM 1459+0857B are T4/5 dwarfs, and WD 0806-661B is a probable Y dwarf and is almost certainly of planetary mass (Luhman et al. 2014). All systems are old, with ages of at least 2 Gyr, and WISEU 0055+5947 is probably the oldest, based on its low effective temperature and age estimate. The wide separation of the brown and white dwarfs means that the brown

dwarf is unlikely to have been affected by the evolution of the white dwarf progenitor and also that the white dwarf evolution is unlikely to have been truncated during a common envelope phase. This is supported by the fact that none of the white dwarfs in these systems are of low enough mass to have formed via binary evolution (e.g., Marsh 1995). The fact that the components of these binaries are comoving but have not affected each other's evolution makes them ideal benchmark systems for determining spectroscopic parameters of old brown dwarfs.

11.6.4. WISEA J075438.20+090044.9

Based on WISE/NEOWISE imaging alone, the WISEA 0754+0900 motion appears visually similar to that of the 780'' distant M6 dwarf LP 483-66. The WISE-based proper motion of WISEA 0754+0900 ($\mu_\alpha = 267 \pm 72 \text{ mas yr}^{-1}$, $\mu_\delta = -179 \pm 90 \text{ mas yr}^{-1}$ according to the CatWISE 2020 catalog) is consistent with the Gaia DR2 proper motion of LP 483-66 ($\mu_\alpha = 414 \text{ mas yr}^{-1}$, $\mu_\delta = -233 \text{ mas yr}^{-1}$) to within $\sim 2\sigma$ along both directions. Our photometric distance estimate for WISEA 0754+0900 ($26.6_{-3.5}^{+4.0}$ pc; Table 9) is also consistent with the LP 483-66 parallax from Gaia (33.2 mas, corresponding to a distance of 30.1 pc). However, our WISE+Spitzer motion ($\mu_\alpha = 166 \pm 52 \text{ mas yr}^{-1}$, $\mu_\delta = -280 \pm 55 \text{ mas yr}^{-1}$; Table 6) differs substantially from the LP 483-66 Gaia proper motion, with a discrepancy of nearly 5σ along the R.A. direction. No anomalies are evident in our WISEA 0754+0900 ch2 imaging/astrometry, so we view our WISE+Spitzer linear motion as superior to estimates based solely on WISE. As a result, we consider it unlikely that WISEA 0754+0900 and LP 483-66 are associated given the available evidence.

11.7. Notes on Individual Objects

11.7.1. WISEA J035410.03–572104.0

WISEA 0354–5721 has $\chi_{\text{motion}}^2 = 16.7$ and therefore is not motion confirmed by our WISE+Spitzer astrometry analysis. Nevertheless, this source appears to have a very faint/red counterpart moving southward when comparing z -band images from DECaLS DR8 (Dey et al. 2019) with those from Dark Energy Survey DR1 (Abbott et al. 2018). The z -band counterpart has $z = 22.52 \pm 0.15$ (AB) according to DECaLS DR8. Assuming that this z -band source is indeed linked to our WISE/Spitzer brown dwarf candidate, then the object would be most consistent with a $\sim T7.5$ phototype and a distance of ~ 33 pc.

11.7.2. WISEA J053535.43–644518.5

WISEA 0535–6445 is unusual among our sample in that its $\text{ch1–ch2} \approx 0$ color is not indicative of a mid-T or later brown dwarf, but rather is consistent with a broad range of earlier spectral types (Patten et al. 2006). Little archival photometry is available for this object, which lacks counterparts in Gaia and 2MASS while falling outside of the VHS footprint. The 2MASS nondetection implies a $J - W2 \gtrsim 1.9$ color limit. WISEA 0535–6445 has $W1 - W2 = 0.17 \pm 0.04$ according to the CatWISE Preliminary catalog, with slightly redder WISE colors of $W1 - W2 = 0.23 \pm 0.05$ and $W1 - W2 = 0.29 \pm 0.02$ according to the AllWISE and unWISE Catalogs, respectively. The NOAO Source Catalog (Nidever et al. 2018) reports a DECam counterpart with AB magnitudes of $i = 21.87 \pm 0.07$ and

$z = 20.36 \pm 0.06$. The $J - W2$ lower bound, $W1 - W2$ color, and $i - z$ color indicate an early L type, and $i - W2 = 6.61 \pm 0.08$ suggests a spectral type of $\sim L3$. The WISEA 0535–6445 photometry is not consistent with an M subdwarf or L subdwarf scenario. If WISEA 0535–6445 is an L3 dwarf, then its photometric distance estimate would be ~ 84 pc, corresponding to a tangential velocity of $\sim 112 \text{ km s}^{-1}$.

11.7.3. CWISEP J135937.65–435226.9

CWISEP 1359–4352 was inadvertently targeted as part of p14299 despite the fact that CatWISE p14034 had previously observed it (Meisner et al. 2020). Our p14299 observations of this object are deeper than those from p14034 and so provide a higher-S/N color estimate of $\text{ch1–ch2} = 2.25 \pm 0.09$ mag, corresponding to a best-fit spectral type estimate of T9.5. The 1σ ch1–ch2 color intervals from p14034 and p14299 overlap for this source, although the central color value from Meisner et al. (2020) had scattered sufficiently redward to yield a phototype of Y0 rather than T9.5 as we have obtained here.

12. Conclusion

We have presented critical Spitzer photometric follow-up of 95 brown dwarf candidates discovered by the Backyard Worlds citizen science project. Our Spitzer astrometry allows us to verify the motions of most of these objects, certifying that these are new members of the solar neighborhood. Additionally, Keck/NIRES and Magellan/FIRE spectroscopy of 10 candidates confirms in all cases that the targets are brown dwarfs. Our Spitzer imaging also yields photometric spectral types and distances; these estimates are crucial for pinpointing the superlative objects among our sample, separating out the strong Y dwarf candidates from the late T dwarfs.

Among our most exciting discoveries are new candidate members of the 10 pc sample, two objects moving faster than $2'' \text{ yr}^{-1}$, three T-type subdwarf candidates, five Y dwarf candidates, and a new T8 plus white dwarf comoving system. Our Y dwarf candidates begin bridging the gap between the bulk of the Y dwarf population and the coldest known brown dwarf, making them potential targets for JWST spectroscopy. Backyard Worlds is actively pursuing additional ground-based follow-up of the discoveries presented in this study, especially spectroscopy where feasible. While this work's new brown dwarf candidates already demonstrate the power of citizen science for mapping the solar neighborhood, these objects make up only a small fraction of Backyard Worlds moving object discoveries to date. As NEOWISE continues scanning the sky, Backyard Worlds will endeavor to search all of its newly delivered data for yet more cold and close neighbors to the Sun.


We thank the anonymous referee for valuable comments. The Backyard Worlds: Planet 9 team would like to thank the many Zooniverse volunteers who have participated in this project, from providing feedback during the beta review stage to classifying flipbooks to contributing to the discussions on TALK. We would also like to thank the Zooniverse web development team for their work creating and maintaining the Zooniverse platform and the Project Builder tools. This research was supported by NASA grant 2017-ADAP17-0067. S.L.C. acknowledges the support of an STFC Ernest Rutherford Fellowship. Support for this work was provided by NASA through the NASA Hubble Fellowship grant HST-HF2-51447.001-A awarded by the Space Telescope Science

Institute, which is operated by the Association of Universities for Research in Astronomy, Inc., for NASA, under contract NAS5-26555. This publication makes use of data products from the Wide-field Infrared Survey Explorer, which is a joint project of the University of California, Los Angeles, and the Jet Propulsion Laboratory/California Institute of Technology, funded by the National Aeronautics and Space Administration. This research has made use of the NASA/IPAC Infrared Science Archive, which is funded by the National Aeronautics and Space Administration and operated by the California Institute of Technology. This research has made use of the VizieR catalog access tool, CDS, Strasbourg, France (DOI :10.26093/cds/vizieR). The original description of the VizieR service was published in Ochsenbein et al. (2000). This work has made use of the white dwarf cooling models hosted by Pierre Bergeron at <http://www.astro.umontreal.ca/~bergeron/CoolingModels>.

Facilities: Spitzer(IRAC), HST(WFC3), WISE/NEOWISE, UKIRT(WFCAM), VISTA(VIRCAM), IRSA, 2MASS, Gaia.

Software: MOPEX (Makovoz & Khan 2005; Makovoz & Marleau 2005), WiseView (Caselden et al. 2018), astrometry.net (Lang et al. 2010).

ORCID iDs

Aaron M. Meisner  <https://orcid.org/0000-0002-1125-7384>
 Jacqueline K. Faherty  <https://orcid.org/0000-0001-6251-0573>
 J. Davy Kirkpatrick  <https://orcid.org/0000-0003-4269-260X>
 Adam C. Schneider  <https://orcid.org/0000-0002-6294-5937>
 Dan Caselden  <https://orcid.org/0000-0001-7896-5791>
 Jonathan Gagné  <https://orcid.org/0000-0002-2592-9612>
 Marc J. Kuchner  <https://orcid.org/0000-0002-2387-5489>
 Adam J. Burgasser  <https://orcid.org/0000-0002-6523-9536>
 Sarah L. Casewell  <https://orcid.org/0000-0003-2478-0120>
 John H. Debes  <https://orcid.org/0000-0002-1783-8817>
 Étienne Artigau  <https://orcid.org/0000-0003-3506-5667>
 Daniella C. Bardalez Gagliuffi  <https://orcid.org/0000-0001-8170-7072>
 Sarah E. Logsdon  <https://orcid.org/0000-0002-9632-9382>
 Rocío Kiman  <https://orcid.org/0000-0003-2102-3159>
 Katelyn Allers  <https://orcid.org/0000-0003-0580-7244>
 Chih-chun Hsu  <https://orcid.org/0000-0002-5370-7494>
 John P. Wisniewski  <https://orcid.org/0000-0001-9209-1808>
 Guillaume Colin  <https://orcid.org/0000-0002-7630-1243>
 Hugo A. Durantini Luca  <https://orcid.org/0000-0002-4143-2550>
 Sam Goodman  <https://orcid.org/0000-0003-2236-2320>
 Léopold Gramaize  <https://orcid.org/0000-0002-8960-4964>
 Leslie K. Hamlet  <https://orcid.org/0000-0002-7389-2092>
 Ken Hinckley  <https://orcid.org/0000-0002-4733-4927>
 Frank Kiwy  <https://orcid.org/0000-0001-8662-1622>
 Austin Rothermich  <https://orcid.org/0000-0003-4083-9962>
 Arttu Sainio  <https://orcid.org/0000-0003-4864-5484>
 Jörg Schümann  <https://orcid.org/0000-0002-7587-7195>
 Christopher Tanner  <https://orcid.org/0000-0002-9807-5435>
 Melina Thévenot  <https://orcid.org/0000-0001-5284-9231>

References

Abbott, T. M. C., Abdalla, F. B., Allam, S., et al. 2018, *ApJS*, 239, 18
 Artigau, E., Doyon, R., Vallee, P., Riopel, M., & Nadeau, D. 2004, *Proc. SPIE*, 5492, 1479
 Bardalez Gagliuffi, D. C., Faherty, J. K., Schneider, A. C., et al. 2020, *ApJ*, 895, 145
 Batygin, K., & Brown, M. E. 2016, *AJ*, 151, 22

Beichman, C., Gelino, C. R., Kirkpatrick, J. D., et al. 2013, *ApJ*, 764, 101
 Bochanski, J. J., Hennawi, J. F., Simcoe, R. A., et al. 2009, *PASP*, 121, 1409
 Burgasser, A. J., McElwain, M. W., Kirkpatrick, J. D., et al. 2004, *AJ*, 127, 2856
 Caselden, D., Westin, P., III, Meisner, A., Kuchner, M., & Colin, G. 2018, WiseView: Visualizing Motion and Variability of Faint WISE Sources, Astrophysics Source Code Library, ascl:1806.004
 Chambers, K. C., Magnier, E. A., Metcalfe, N., et al. 2016, arXiv:1612.05560
 Churchwell, E., Babler, B. L., Meade, M. R., et al. 2009, *PASP*, 121, 213
 Cross, N. J. G., Collins, R. S., Mann, R. G., et al. 2012, *A&A*, 548, A119
 Cummings, J. D., Kalirai, J. S., Tremblay, P. E., Ramirez-Ruiz, E., & Choi, J. 2018, *ApJ*, 866, 21
 Cushing, M. C., Kirkpatrick, J. D., Gelino, C. R., et al. 2011, *ApJ*, 743, 50
 Cushing, M. C., Vacca, W. D., & Rayner, J. T. 2004, *PASP*, 116, 362
 Cutri, R. M., Mainzer, A., Conrow, T., et al. 2015, Explanatory Supplement to the NEOWISE Data Release Products, Tech. Rep. 1
 Cutri, R. M., Wright, E. L., Conrow, T., et al. 2012, Explanatory Supplement to the WISE All-Sky Data Release Products, Tech. Rep. 1
 Cutri, R. M., Wright, E. L., Conrow, T., et al. 2013, Explanatory Supplement to the AllWISE Data Release Products, Tech. Rep. 1
 Day-Jones, A. C., Pinfield, D. J., Ruiz, M. T., et al. 2011, *MNRAS*, 410, 705
 Debes, J. H., Thévenot, M., Kuchner, M. J., et al. 2019, *ApJL*, 872, L25
 Dey, A., Schlegel, D. J., Lang, D., et al. 2019, *AJ*, 157, 168
 Dotter, A. 2016, *ApJS*, 222, 8
 Dupuy, T. J., & Liu, M. C. 2012, *ApJS*, 201, 19
 Dye, S., Lawrence, A., Read, M. A., et al. 2018, *MNRAS*, 473, 5113
 Edge, A., Sutherland, W., Kuijken, K., et al. 2013, *Msngr*, 154, 32
 Eisenhardt, P. R. M., Marocco, F., Fowler, J. W., et al. 2020, *ApJS*, 247, 69
 Faherty, J. K., Burgasser, A. J., Cruz, K. L., et al. 2009, *AJ*, 137, 1
 Faherty, J. K., Goodman, S., Caselden, D., et al. 2020, *ApJ*, 889, 176
 Fazio, G. G., Hora, J. L., Allen, L. E., et al. 2004, *ApJS*, 154, 10
 Fitzpatrick, M. J., Olsen, K., Economou, F., et al. 2014, *Proc. SPIE*, 9149, 91491T
 Fontaine, G., Brassard, P., & Bergeron, P. 2001, *PASP*, 113, 409
 Gaia Collaboration, Brown, A. G. A., Vallenari, A., et al. 2018, *A&A*, 616, A1
 Gaia Collaboration, Prusti, T., de Bruijne, J. H. J., et al. 2016, *A&A*, 595, A1
 Gardner, J. P., Mather, J. C., Clampin, M., et al. 2006, *SSRv*, 123, 485
 Gentile Fusillo, N. P., Tremblay, P.-E., Gänsicke, B. T., et al. 2019, *MNRAS*, 482, 4570
 Greisen, E. W., & Calabretta, M. R. 2002, *A&A*, 395, 1061
 Hambly, N. C., Collins, R. S., Cross, N. J. G., et al. 2008, *MNRAS*, 384, 637
 Hawley, S. L., Covey, K. R., Knapp, G. R., et al. 2002, *AJ*, 123, 3409
 Kirkpatrick, J. D., Cushing, M. C., Gelino, C. R., et al. 2011, *ApJS*, 197, 19
 Kirkpatrick, J. D., Gelino, C. R., Cushing, M. C., et al. 2012, *ApJ*, 753, 156
 Kirkpatrick, J. D., Kellogg, K., Schneider, A. C., et al. 2016, *ApJS*, 224, 36
 Kirkpatrick, J. D., Martin, E. C., Smart, R. L., et al. 2019, *ApJS*, 240, 19
 Kirkpatrick, J. D., Schneider, A., Fajardo-Acosta, S., et al. 2014, *ApJ*, 783, 122
 Kuchner, M. J., Faherty, J. K., Schneider, A. C., et al. 2017, *ApJL*, 841, L19
 Lang, D., Hogg, D. W., Mierle, K., Blanton, M., & Roweis, S. 2010, *AJ*, 139, 1782
 Lawrence, A., Warren, S. J., Almaini, O., et al. 2007, *MNRAS*, 379, 1599
 Limoges, M. M., Bergeron, P., & Lépine, S. 2015, *ApJS*, 219, 19
 Limoges, M. M., Lépine, S., & Bergeron, P. 2013, *AJ*, 145, 136
 Lindegren, L., Hernández, J., Bombrun, A., et al. 2018, *A&A*, 616, A2
 Luhman, K. L. 2013, *ApJL*, 767, L1
 Luhman, K. L. 2014a, *ApJ*, 781, 4
 Luhman, K. L. 2014b, *ApJL*, 786, L18
 Luhman, K. L., Burgasser, A. J., & Bochanski, J. J. 2011, *ApJL*, 730, L9
 Luhman, K. L., Morley, C. V., Burgasser, A. J., Esplin, T. L., & Bochanski, J. J. 2014, *ApJ*, 794, 16
 Mace, G. N., Kirkpatrick, J. D., Cushing, M. C., et al. 2013, *ApJ*, 777, 36
 Mainzer, A., Bauer, J., Cutri, R., et al. 2014, *ApJ*, 792, 30
 Mainzer, A., Bauer, J., Grav, T., et al. 2011a, *ApJ*, 731, 53
 Mainzer, A., Cushing, M. C., Skrutskie, M., et al. 2011b, *ApJ*, 726, 30
 Makovoz, D., & Khan, I. 2005, in ASP Conf. Ser. 347, Astronomical Data Analysis Software and Systems XIV, ed. P. Shopbell, M. Britton, & R. Ebert (San Francisco, CA: ASP), 81
 Makovoz, D., & Marleau, F. R. 2005, *PASP*, 117, 1113
 Marocco, F., Caselden, D., Meisner, A. M., et al. 2019, *ApJ*, 881, 17
 Marocco, F., Kirkpatrick, J. D., Meisner, A. M., et al. 2020, *ApJL*, 888, L19
 Marsh, T. R. 1995, *MNRAS*, 275, L1
 Martin, E. C., Kirkpatrick, J. D., Beichman, C. A., et al. 2018, *ApJ*, 867, 109
 Matese, J. J., Whitman, P. G., & Whitmire, D. P. 1999, *Icar*, 141, 354
 Matese, J. J., & Whitmire, D. P. 2011, *Icar*, 211, 926
 McMahon, R. G., Banerji, M., Gonzalez, E., et al. 2013, *Msngr*, 154, 35
 Meisner, A., Bromley, B. C., Nugent, P. E., et al. 2017, *AJ*, 153, 65

- Meisner, A. M., Bromley, B. C., Kenyon, S. J., & Anderson, T. E. 2018a, *AJ*, 155, 166
- Meisner, A. M., Caselden, D., Kirkpatrick, J. D., et al. 2020, *ApJ*, 889, 74
- Meisner, A. M., Lang, D., Schlafly, E. F., & Schlegel, D. J. 2019, *PASP*, 131, 124504
- Meisner, A. M., Lang, D., & Schlegel, D. J. 2018b, *AJ*, 156, 69
- Meisner, A. M., Lang, D. A., & Schlegel, D. J. 2018c, *RNAAS*, 2, 202
- Morley, C. V., Skemer, A. J., Allers, K. N., et al. 2018, *ApJ*, 858, 97
- Nidever, D. L., Dey, A., Olsen, K., et al. 2018, *AJ*, 156, 131
- Ochsenbein, F., Bauer, P., & Marcout, J. 2000, *A&AS*, 143, 23
- Patten, B. M., Stauffer, J. R., Burrows, A., et al. 2006, *ApJ*, 651, 502
- Paxton, B., Bildsten, L., Dotter, A., et al. 2011, *ApJS*, 192, 3
- Racine, R. 1978, *JRASC*, 72, 324
- Saumon, D., & Marley, M. S. 2008, *ApJ*, 689, 1327
- Schlafly, E. F., Green, G. M., Lang, D., et al. 2018, *ApJS*, 234, 39
- Schlafly, E. F., Meisner, A. M., & Green, G. M. 2019, *ApJS*, 240, 30
- Schneider, A. C., Cushing, M. C., Kirkpatrick, J. D., et al. 2015, *ApJ*, 804, 92
- Schneider, A. C., Greco, J., Cushing, M. C., et al. 2016, *ApJ*, 817, 112
- Scholz, R. D. 2014, *A&A*, 561, A113
- Simcoe, R. A., Burgasser, A. J., Schechter, P. L., et al. 2013, *PASP*, 125, 270
- Simpson, R., Page, K. R., & De Roure, D. 2014, in Proc. of the 23rd Int. Conf. on World Wide Web, WWW 14 Companion (New York: Association for Computing Machinery), 1049
- Skemer, A. J., Morley, C. V., Allers, K. N., et al. 2016, *ApJL*, 826, L17
- Skrutskie, M. F., Cutri, R. M., Stiening, R., et al. 2006, *AJ*, 131, 1163
- Vacca, W. D., Cushing, M. C., & Rayner, J. T. 2003, *PASP*, 115, 389
- Wenger, M., Ochsenbein, F., Egret, D., et al. 2000, *A&AS*, 143, 9
- Werner, M. W., Roellig, T. L., Low, F. J., et al. 2004, *ApJS*, 154, 1
- Wilson, J. C., Henderson, C. P., Herter, T. L., et al. 2004, *Proc. SPIE*, 5492, 1295
- Wright, E., Eisenhardt, P., Mainzer, A., et al. 2010, *AJ*, 140, 1868
- Wright, E. L., Mainzer, A., Kirkpatrick, J. D., et al. 2014, *AJ*, 148, 82
- Zhang, Z., Liu, M. C., Hermes, J. J., et al. 2020, *ApJ*, 891, 171
- Zhang, Z. H., Burgasser, A. J., Gálvez-Ortiz, M. C., et al. 2019, *MNRAS*, 486, 1260